Addressing a Major Hurdle for Brain Cancer Therapy: Widespread Therapeutic Delivery

By Karina Negrón

A dissertation submitted to Johns Hopkins University in conformity with the requirements for the degree of Doctor of Philosophy

Baltimore, Maryland
March 2019

Abstract

Despite the most advanced therapeutic regimen, median survival of malignant gliomas remains ~ 14 months. Given the aggressive and infiltrative nature of it, inability of conventional gene vectors and drug carriers to provide a widespread therapeutic distribution is an utmost challenge. Convection enhanced delivery (CED) is an attractive method to bypass the blood-brain barrier and facilitate widespread therapeutic distribution within brain parenchyma by creating a continuous pressure-driven bulk flow. In this work I demonstrate that local infusion of nanoparticle (NP)-based delivery systems designed to efficiently penetrate the highly adhesive and nanoporous extracellular matrix synergistically enhances the payload distribution within healthy and tumor-bearing brains. I start by establishing in Chapter 1 the broad picture that medicine challenges faced with the current treatment strategies for central nervous system diseases, as well as the numerous barriers that NPs must overcome to successfully achieve a therapeutic distribution in the brain. It also describes a very detailed protocol for local infusion doing stereotaxic surgeries in rodent brains via CED. In Chapter 2, I established a new system to assess for gene transfection efficiency in vitro by utilizing 3D multicellular tumor spheroids, providing insights for the effect of non-adhesive coating, made of polyethylene glycol (PEG), in synthetic gene vectors, made of polyethyleneimine (PEI), and their extent of penetration with accurate in vitro-to-in vivo correlation in the brain. Furthermore, I developed a mathematical protocol to quantify the penetration profile of nanoparticles in the 3D multicellular tumor spheroids. With this model, I confirmed that NPs with higher ratios of PEG possessed better penetration capabilities, which led to greater volumes of transgene expression in healthy and tumor rat brain tissues. Using this DNA-NP system, I also demonstrated that long-term gene expression can be achieved in the brain up to 3 weeks, by replacing the promoter that regulates the expression of the reporter gene. This application may be beneficial for future therapeutic studies, including neurodegenerative diseases. In Chapter 3, I demonstrated that a series of

eight end-capped polymer variants, made of biodegradable poly-beta-amino-ester (PBAE), perform differently in a mouse glioblastoma 3D model and in vivo, depending on their physicochemical properties and colloidal stability. I identified 4 lead candidates for widespread transgene expression in the brain. Furthermore, I tested the top candidate in 1 mouse glioblastoma model and 2 pediatric brain tumor models, which showed well transfected regions at the tumor site and tumor periphery. Lastly, I developed a protocol that allows freeze-drying of these biodegradable NPs for long-term storage as a powder form. This form of proper storing and cryoprotection for extended periods of time did not compromised the NPs performance in vivo, which serves of big relevance to our collaborators and future clinical studies. Lastly, I completed this work with Chapter 4, describing the effect of 3 different triblock copolymers consisting of a central hydrophobic block of polypropylene oxide (PPO) flanked by two hydrophilic blocks of polyethylene oxide (PEO) that serve as non-adhesive coatings in biodegradable polymer-based nanoparticles made of the hydrophobic poly(lactic-co-glycolic acid) (PLGA) for local drug delivery to the brain. I demonstrated that these triblock copolymers coat PLGA-NPs in a unique manner, depending on the content of the PPO hydrophobic block, resulting in better shielding of the hydrophobic core for the copolymer with the highest PPO ratio. Therefore, this trend showed a direct correlation between the coating efficiency of each copolymer and the volume of distribution in rat brain after local infusion. Furthermore, I discovered that the brain intercellular space can be penetrable by nanoparticles up to ~200 nm in diameter when coated with the copolymer possessing the highest PPO content. Lastly, I also established a protocol to freeze-dry and store these particles as a powder form for long-term periods of time, and by increasing the osmotic pressure of the nanoparticles solution, I discovered that the widespread distribution can be further enhanced in the brain. This serves of great utility for future drug delivery studies where greater tissue coverage is necessary to kill the infiltrative brain cancer cells. Ultimately, I hope that this work will contribute to the greater

understanding of localized nanomedicine, which will help yield more effective treatments thus improving and extending patients' lives.

Thesis Advisor:

Dr. Justin Hanes, Ph.D. (Designated Reader)

Thesis Committee Members:

Dr. Jung Soo Suk, Ph.D.

Dr. James C. Barrow, Ph.D. (Designated Reader)

Dr. Charles G. Eberhart, M.D. Ph.D.

Acknowledgments

I can say with certainty that no words will ever make justice to describe how thankful I am with God for giving me the opportunity to come to this prestigious institution to start and successfully complete this amazing journey. I owe everything to Him. If I was to accurately and wholly thank every person who helped me achieve what I have in the past few years, I would need a document longer than this manuscript. Science is a team effort, and I would have accomplished very little on my own. Therefore, this dissertation is more of a reflection and documentation of the immense amount of work that was done by not only me and my immediate colleagues but the 'giants' whose shoulders we have stood on as we delved into the unknown. I, merely, am the person who is formally recording the methods, data, and rationale behind each experiment. Before I spend the rest of this section directly thanking various individuals, I must, first, formally acknowledge those who are not explicitly mentioned including, but certainly not limited to, the JHMI community and the related scientists, administrators, and other members of the Pharmacology department who guided me through this journey.

First, I would like to thank my amazing scientific family at the Center for Nanomedicine at Hopkins. It would be difficult to have worked with a more fun, more supportive group of people, all of which are brilliant and committed to our greater cause. Their various expertise and backgrounds made a large portion of this work much more straight forward and easy to navigate. Their technical 'this-is-how-you-do-it' was the proverbial flashlight that guided me through the unknown abyss, and without it, I would be undoubtedly still lost in the bench somewhere. I must thank the "original brain team" Clark (now Dr. Zhang), Panos (now Dr. Mastorakos, neurosurgeon), and Eric (soon to be Dr. Song) that took me under their wings and allowed me to feel so welcomed and mentored during my first year as a student. Thanks for answering my emails and "urgent" phone calls (specially Clark), even when we are hundreds of miles away and years passed since you left. If that is not true friendship and mentorship, I don't

know what is. I also cannot emphasize enough how grateful I am with my undergraduate students Young Eun, Miguel, Billy, Mike, Amna, Namir, Casey, Jillian, Sunny, and Tina who I had the opportunity to mentor and make great science with. You guys are the masters behind the figures for all my papers and presentations. Thanks for all the extra hours, weekends, countless “lets-try-it-again”, and most importantly, your incredible support even when experiments failed.

I also am exceptionally grateful for the friendship and trust circle I had at CNM. They celebrated both of my pregnancies, and they never made me feel guilty for bringing my son to lab or taking a day off to stay home with him. I rarely ever felt that I was surrounded by co-workers. Rather, every day, I felt that I always surrounded by friends and even family, particularly with the fellow graduate students, who became my siblings for the past 5 years. To my lab sisters: Thuy, thank you for your trust and honest friendship, for your wisdom and countless advices; Hannah, I cannot believe we did not become closer sooner! Thanks for all the fun activities/hobbies we did together, and for all the life experiences we have in common; Divya, thanks for being my closest friend inside and outside of lab and for letting me share all of the personal emotions during our morning teas and late night texts, there is no better way to end my road with the brain team than by leaving you in charge.

I would also like to thank Dr. Laura Ensign, my lab mom, for being the greatest role model and influence in my Ph.D. Your wisdom and down-to-earth stories always gave me the push I needed to never give up. To our program director, Dr. Caren Meyers, thanks for always having my back and for being a good advisor to all of us. To Dr. Surojit Sur, my dearest friend and collaborator, thank you for your patience and understanding every time I visited your lab seeking for good advice. You continuously had the craziest of ideas, but they always helped me think “not-like-an-engineer-but-like-a-biologist” to move my projects forward. To my two advisors Dr. Justin Hanes and Dr. Jung Soo Suk, thank you for toughening me up. You helped me build my character and see things black or white. I always received the technical advice I needed,

and your discussions and overall guidance helped me understand the ‘big picture’ aspects of my work and helped mold what felt was a series of random experiments into a cohesive story. Next, I would like to thank Dr. Eberhart and Dr. Barrow, for their support and input regarding my work and for taking the time to sit on my thesis committee. Finally, I’d like to acknowledge the Department of Pharmacology and the friendly staff for their support, and the United States National Institute of Health for funding this work.

It is no secret that life outside of the lab is most important to me. I must acknowledge the personal guidance, support, and love that I received from my family. I would like to first thank my married family, the Negrón’s. You all have exemplified the notion that true family is not limited to those who you share DNA with, thanks for sticking by me through it all since my college years. Next, I thank my immediate nuclear family. Most notably, I must thank my mom and grandma who I cannot begin to express my gratitude for. Despite living hundreds of miles away from them, they were always a phone call or text message away. Thank you for your endless prayers, words of encouragement, and wisdom. Mom, I know you are my biggest fan, but I hope one day I can live up to the legacy that you have made so that you can see how much more I am a fan of yours. Thank you for giving me everything, literally everything you had so I can pursue my dreams. You all at times, were the major driving force which kept me optimistic and motivated.

Finally, I would like to thank those that should receive all the credit for my personal well-being. I would like to thank my husband Javier and my son Ian. The endless supply of love I received from you two every single day of this experience is indescribable in words. Because of you, I was able to get out of bed every morning and slept comfortably at night and for that, I am eternally grateful. Javier, we have shared 9 incredible years together, since my freshmen years until now, you have always made me laugh, wiped my tears, hugged me tight, watched me succeed, seen me fail, and kept me strong. Thank you for believing in me more than I believe in myself. I could not have done it without you. This Ph.D. is for both of us.

Table of Contents

List of Tables

List of Figures

Introduction

Chapter 1: Enhancing Therapeutic Delivery to the Brain via Convection Enhanced Delivery

Chapter 2: Widespread Gene Transfer to Brain Tumors via Synthetic Polymer-Based DNA Nanoparticles

Introduction

Brain tumors and current status of therapeutics for malignant gliomas

1. Brain tumors

Brain tumors grow as an abnormal mass of tissue in which cells grow and multiply uncontrollably, seemingly unchecked by the molecular mechanisms that control normal cells. More than 150 different brain tumors have been documented, but the two main groups of brain tumors are termed primary and metastatic (*1*). Primary brain tumors include tumors that originate from the tissues of the brain or its surroundings. These are categorized as glial (derived from glial cells) or non-glial (developed on or in the structures of the brain, including nerves, blood vessels and glands), each type can be benign or malignant. Metastatic brain tumors include tumors that arise elsewhere in the body, primarily the breast or lungs, and migrate to the brain, usually through the bloodstream. These are considered as only malignant (Figure 1).

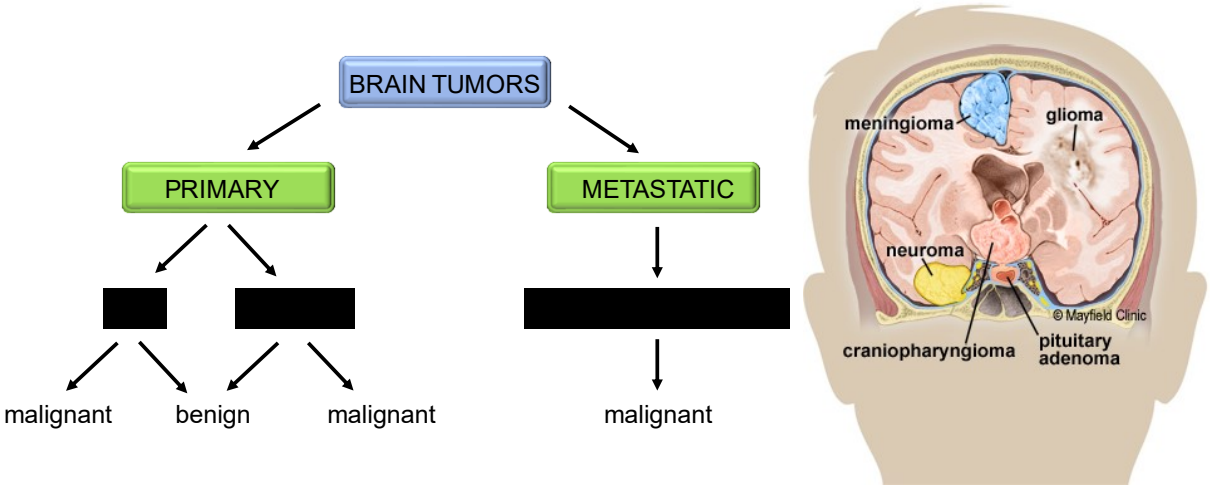

Figure 1: Schematic representation of the different types of brain tumors. Brain tumors may grow from nerves (neuroma), dura (meningioma), or pituitary gland (craniopharyngioma or pituitary adenoma). They may also grow from the brain tissue itself (glioma).

Metastatic tumors affect nearly one in four patients with cancer, or an estimated 150,000 people a year, with up to 40 percent developed from lung cancer. For the purpose of this Thesis, we will be solely focused the on primary brain tumors, mainly malignant gliomas.

The estimated average mortality rate for primary brain tumors in 2018 and 2019 in the United States is ~18,000 deaths (*2*). Furthermore, 78,980 new cases are expected to be diagnosed this year, including malignant, non-malignant, and other types of central nervous system (CNS) related tumors (*2*). Based on population-based database analyses, the five-year relative survival rate in the United States following a diagnosis of a primary malignant brain and other CNS tumors is only 34.9% (*2*). Over the years, the World Health Organization (WHO) has developed a grading system to indicate a tumor's malignancy or benignity based on its histological features under a microscope (Figure 2) (*3*).

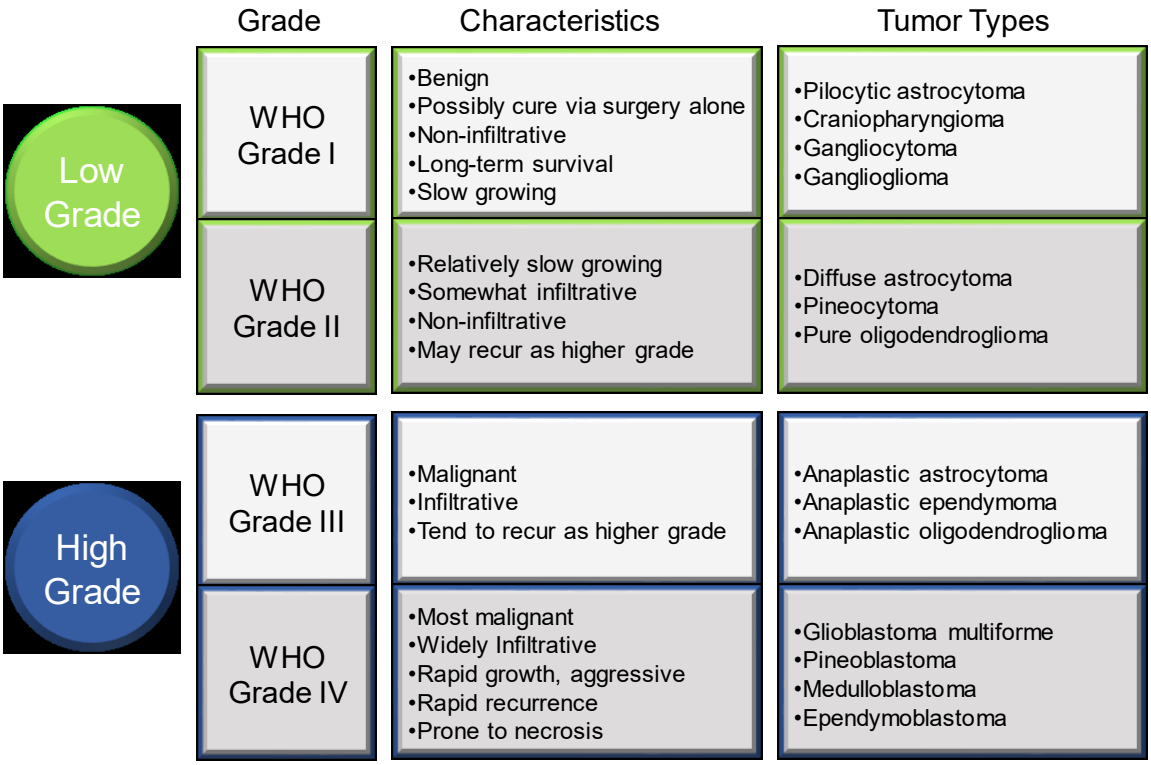

Figure 2: World Health Organization (WHO) brain tumor grades.

2. Currently approved therapies for brain tumors and their limitations

Brain tumors (whether primary or metastatic, benign or malignant) usually are treated with surgery, radiation, and/or chemotherapy (alone or in various combinations) (Figure 3). Treatment for a brain tumor depends on the type, size and location of the tumor, as well as the patient's overall health and preferences.

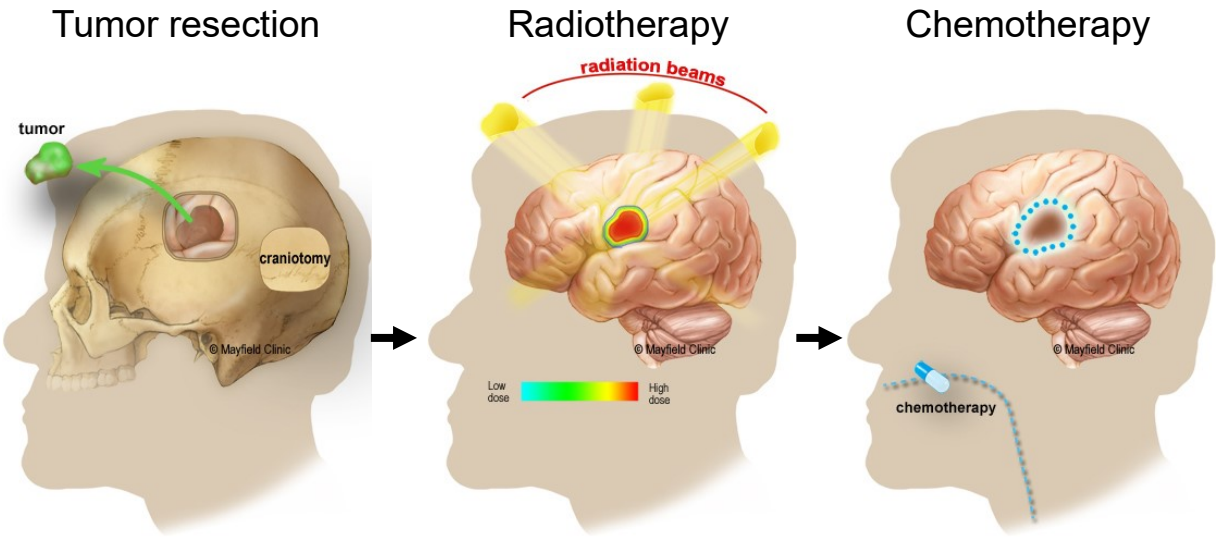

Figure 3: Surgery is the treatment of choice for brain tumors that can be reached without causing major injury to vital parts of the brain. A neurosurgeon performs a craniotomy to open the skull and remove the tumor. Sometimes only part of the tumor is removed if it is near critical areas of the brain. Radiation or chemotherapy may be used on the remaining tumor cells. Radiation damages the DNA inside cells, making them unable to divide and grow. The radiation beams are shaped to match the tumor and minimize exposure to normal brain tissue. The benefits of radiation are not immediate but occur with time. Aggressive tumors, whose cells divide rapidly, tend to respond quickly to radiation. Over time, the abnormal cells die, and the tumor may shrink. Chemotherapy for high-grade gliomas is usually taken as a pill daily for a set period of time called a cycle. The drug circulates through the bloodstream to the brain where it crosses the blood-brain-barrier to the tumor.

Surgery

Most brain tumors in infants, children, and adults require surgical removal, or at least a biopsy, as part of the treatment. For low-grade or slow-growing tumors, surgery may be the only intervention necessary. If the brain tumor is in a place that makes it accessible for an operation, it will be preferred to remove as much of the brain tumor as possible. This may also help to relieve intracranial pressure caused by the tumor, reducing signs and symptoms. However, surgery carries risks, such as infection and bleeding. Other risks may depend on the part of your brain where the tumor is located. For instance, surgery on a tumor near nerves that connect to the eyes may carry a risk of vision loss. Thanks to the evolution of medicine, neurosurgeons can now execute awake brain surgery. The procedure, offered at very few medical centers in the

country, is used to help certain people who've been told they have an inoperable brain tumor. The surgical team can remove the tumor safely with minimized risk of serious complications.

Radiation

Radiation therapy is performed after surgery for some types of gliomas or for those in locations where surgery is not safe. This is executed by using high-energy beams, such as X-rays or protons, to kill tumor cells. Three types of radiation therapy are used to treat gliomas: external beam radiation therapy, internal radiation, and stereotactic radiosurgery. External beam radiation can focus just on the area of your brain where the tumor is located, or it can be applied to your entire brain (whole-brain radiation). Whole-brain radiation is most often used to treat cancer that spreads to the brain from some other part of the body. Stereotactic radiosurgery uses multiple beams of radiation to give a highly focused form of radiation treatment in a very small area. Each beam of radiation possesses a low power intensity, but the point where all the beams meet, i.e. tumor site, receives a very large dose of radiation to kill the cancer cells. This has been explored using new technologies such as a gamma knife or the linear accelerator. Common side effects during or immediately following radiation include fatigue, headaches, memory loss and scalp irritation. For tumors that are very close to sensitive areas of the brain, proton therapy may reduce the risk of side effects associated with radiation. But proton therapy has not proved to be more effective than standard radiation therapy with X-rays.

Chemotherapy: Temozolomide

Chemotherapy is used for most aggressive high-grade brain tumors. These can be administered orally, intravenously, injected directly into the cerebrospinal fluid, or injected directly into the cavity left after surgical removal of a brain tumor. The standard of care for newly diagnosed brain tumors, particularly glioblastoma multiforme (GBM), includes maximal safe tumor resection, 6 weeks of concurrent radiation with temozolomide (TMZ) as a pill, followed by maintenance (or adjuvant) TMZ for a total of 6 to 12 cycles (*4*). TMZ has increased the median overall survival for GBM patients from less than 12 months (*5*), to 14.6 months, and the

percentage of patients alive at two years has been reported to increase from 10.4% to 26.5% (*4, 6*). However, TMZ is an alkylating agent, therefore, its therapeutic benefit depends on its ability to alkylate/methylate DNA, which most often occurs at the N-7 or O-6 positions of guanine residues, triggering apoptosis (*6, 7*). The problem is that some tumor cells can repair this type of DNA damage by expressing a protein, O6-alkylguanine-DNA alkyltransferase (AGT), encoded in humans by the O-6-methylguanine-DNA methyltransferase (MGMT) gene, thus, diminishing the therapeutic efficacy of TMZ (*8*). Furthermore, cells lacking a "normal" DNA mismatch repair system do not detect alkylation adducts and hence are resistant to TMZ even when they lack MGMT (*9*). Lastly, besides the drug-resistance, the major disadvantage of TMZ is its short half-life of 1.8 h (*6*), thus, requiring multiple high doses for the patient.

Targeted drug therapy: Bevacizumab

Since angiogenesis (the growth of new blood vessels) is one of the hallmarks for most malignant gliomas, inhibitors of this pathway have also been approved for GBM (*10*). Bevacizumab (BEV), a humanized monoclonal antibody binding specifically to circulating vascular endothelial growth factor (VEGF), received accelerated approval by the United States Food and Drug Administration (FDA) for the treatment of recurrent GBM in May 2009 based on results from two phase II trials (*11, 12*). However, administration of BEV along with TMZ as an adjuvant treatment for newly diagnosed GBM did not improve median overall survival when compared to patients that received TMZ monotherapy (*13, 14*). Nevertheless, BEV remains as an anti-angiogenesis therapy for recurrent GBM in United States, and it is administered biweekly with or without irinotecan (IRI) (approved for colon or rectal cancer).

Local therapy: Gliadel® wafer

Another common type of therapy for GBM is the use of drug-loaded polymer wafer, Gliadel®, made of biodegradable polymer poly [bis(p-carboxyphenoxy propane) sebacic acid] loaded with the anti-cancer drug carmustine (BCNU) (*15, 16*). Gliadel® had been shown to increase overall survival in patients with recurrent GBM as well as in patients with newly

diagnosed GBM (*16, 17*). However, studies have shown that Gliadel® wafers, along with other locally delivered therapeutics, suffer from the “sink effect” in which the drug is washed away in systemic circulation due to excessive diffusion of the drug, i.e., the concentration of the drug rapidly declines once it has been released from the wafer (*18*). New efforts are being done to extend the survival benefit of wafers by combining BCNU-TMZ using a novel polymeric formulation. Tyler B. and coworkers demonstrated that this new wafer combination results in higher local drug concentrations achieved and maintained by its ability to create a stable and hydrophobic microenvironment for both BCNU and TMZ (*19*). This study is also unique in that the two chemotherapeutic agents are delivered from one wafer with uniform release of the compounds into the brain parenchyma.

Tumor treating fields: Optune™

Optune, a tumor treating fields (TTFields) medical device, is a novel therapeutic modality that was approved by the FDA for both recurrent and newly diagnosed GBM in April 2011 and October 2015, respectively (*20*). When Optune is turned on, it creates low-intensity, wave-like electric fields called TTFields. These TTFields are delivered by 4 adhesive patches, called transducer arrays, to the location of the tumor, slowly interfering with cell division (Figure 3). These transducer arrays are applied to the scalp and are connected to the device and battery. EF-14 phase III clinical trial using TTFields along with maintenance TMZ prolonged median overall survival to 20.9 months, which was superior to a median overall survival of 16 months in the control group treated with TMZ monotherapy for newly diagnosed GBM (*21*).

Others

Other therapies have been applied to recurrent GBM, including second craniotomy with or without Gliadel® wafers, salvage radiation, dose-dense TMZ, nitrosoureas, carboplatin, PCV [procarbazine, lomustine (CCNU) and vincristine], etoposide or IRI (*10*). However, none of them have shown significant improvement in the overall survival compared to the standard of care.

3. Clinical trials for recurrent glioblastomas and other types of brain tumors

Adjunct therapies

Combination chemotherapy is the strategy of using chemotherapy drugs concurrently to yield additive or synergistic inhibitory effects to glioma cell growth and make it difficult for cancer cells to develop drug resistance (*22*). However, no chemotherapy combination has yet been shown to extend survival time than current standard of care treatment for recurrent GBM patients through phase III studies. Current chemotherapy combinations that have been evaluated in clinical trials are: BEV+IRI, BEV+CCNU, BEV+TTFields, and BEV+TMZ (*23*-*25*).

The triple-drug combination of TMZ, BEV, and IRI, named TBI, has been studied in 3 different clinical trials treating GBM: a phase I study of 41 unresectable GBM patients (NCT00979017) (*26*), a phase II study of 75 newly diagnosed GBM subjects (NCT00597402) (*27*), and a phase I pilot study including 12 high-grade glioma (HGG) subjects (NCT00890786) (*28*). These studies demonstrated that the TBI regimen was reasonably tolerated among GBM and high-grade glioma patients. However, the TBI regimen has not yet been studied in recurrent GBM. Albeit, the FDA does not restrict physicians' practice for “off-label” use of approved medications or their combinations (*29*).

Immunotherapy

The recent success of cancer immunotherapy using immune checkpoint inhibitors (CPIs) against many otherwise untreatable cancers has raised expectations that such approaches could also be successfully used against GBM. For example, combination of anti-programmed cell death protein-1 (PD-1), anti-TIM-3, and targeted radiation showed impressive results in the preclinical mouse GL261 glioma model (*30*). There are currently several ongoing clinical trials of CPIs in GBM including phase III trials with Ipilimumab (blocking CTLA-4) and Nivolumab (blocking PD-1) (NCT02017717, NCT02617589) (*31*).

Adoptive cell transfer therapies for GBM have evolved considerably over time as earlier work focused on less specific approaches utilizing natural killer or lymphokine-activated killer

cells (*32*). Clinical trials for these platforms have become less favored over the past decades, in part due to phase III evidence from solid tumor settings where infusion of cells with interleukin-2 was not found to be superior to interleukin-2 alone (*33*). Of all adoptive cell transfer-based immunotherapies currently in development for GBM, gene-engineered CAR T cells are at the forefront, with encouraging results reported from several recent clinical trials (*34*). Structurally, CAR molecules consist of an extracellular, antigen-binding domain translated in tandem with assorted intracellular signaling regions that have differential effects on T-cell proliferation, effector function, and survival. To date, 4 antigens have been pursued in CAR clinical trials for GBM. These include EGFR variant III (*35*), HER2 (*36*), and IL13Ra2 (*37*). There is also interest in erythropoietin-producing hepatocellular carcinoma A2, although results from clinical trials investigating this target have not yet been released (NCT02575261).

Experiences in the clinics show that GBM presents a particularly difficult target for immunotherapy, and the currently ongoing clinical trials utilizing CPIs, chimeric antigen receptor (CAR) T cells, or different vaccination strategies have resulted in mostly disappointing results (*31*).

Virus-based immunotherapy

It is worth noting that PD-1 blockade has shown impressive results against hypermutated GBM (*38, 39*), indicating that CPIs can be effective in a certain subset of patients. However, CPIs work by blocking the negative regulators of T cell function, thereby sustaining T cell activity. Consequently, tumors with low T cell infiltration (such as GBM) are unlikely to get significant benefit from CPI therapy. In these cases, it would be important to induce T cell infiltration into the tumor prior to CPI therapy. As oncolytic viruses have a potent ability to induce CD8+ T cell responses against tumor cells, it can be expected that precursory oncolytic virotherapy would enhance the effectiveness of CPIs. Therefore, combination of checkpoint blockade with oncolytic virotherapy (selectively kill infected cancer cells) is an attractive option

due to virus-induced inflammatory response in the tumor can lead to upregulation of PD-1 on T cells and PD-L1 on tumor cells (*40*).

There are 19 current trials using oncolytic viruses against GBM (*31*). Of these, perhaps the most promising viruses are DNX-2401, PVS-RIPO, and Toca 511, all of which have shown complete durable responses in approximately 20% of GBM patients who received virus intratumorally (*41-43*). In Toca 511 and DNX-2401 trials, no dose-limiting toxicities were observed (*42, 43*). In the PVSRIPO trial, one death and one dose-limiting toxic effect were reported (*41*). The encouraging results obtained with PVS-RIPO, Toca511, and DNX-2401 have granted them a fast track designation by the FDA for expedited drug review process.

Robust replication-induced cell death can, however, lower the amount of transgene produced by the infected cell. Therefore, any oncolytic virus construct that depends on delivery and expression of therapeutic genes must be carefully optimized. It must also be considered that excessive expression of immunoregulatory transgenes might have unwanted toxic side-effects (*44*). Furthermore, it should not be underestimated that the GBM microenvironment presents a challenge for oncolytic virus delivery into the tumor, as well as effective viral replication and spread within the tumor. In addition, the heavy infiltration of innate immune cells (in both human and mouse models) and the presence glioma stem cells can render the GBM tissue resistant to effective viral spread, pointing out the need for robustly replicating viruses in order to disrupt the suppressive GBM microenvironment (*31*).

4. Moving forward using localized nanomedicine

The history of therapeutic studies for malignant gliomas is filled with attempts to deliver drugs or genes into the tumor cells in a cancer-selective manner, sparing surrounding healthy brain tissue components. Therapeutic delivery to the brain is challenging because of two critical barriers: 1) the blood brain barrier (BBB), which regulates the traffic of substances between the blood stream and the brain, and 2) the tissue interstitial barrier, which compromises 15-20% of

the total brain volume, affecting the flow and intake of nutrients, metabolites, cytokines, neurotransmitters, and numerous molecules present in the tumor and the brain parenchyma. Independent of local or systemic delivery, effective penetration of therapeutic agents to diffuse into the highly infiltrative and not surgically accessible tumor cells is crucial to achieve maximum anti-tumor efficacy.

Nanomedicine represents a promising and versatile platform for the delivery of therapeutics to the brain. The current standard of care, as discussed earlier, yields only a modest therapeutic benefit for patients with malignant gliomas. Recent advances in local drug delivery techniques, along with the development of highly effective brain-penetrating nanoparticles, have significantly improved treatment and imaging of brain tumors in preclinical studies (*45*). The major advantage of this combined strategy is the ability to optimize local therapy, by maintaining an effective and sustained concentration of therapeutics in the brain with minimal systemic toxicity. In this thesis, we investigate the development and application of brain penetrating nanoparticles for improving therapeutic delivery and distribution within the brain, particularly in tumor tissue.

5. References

1. A. A. o. N. Surgeons, Brain Tumors. *AANS* https://www.aans.org/Patients/Neurosurgical-Conditions-and-Treatments/Brain-Tumors, (2019).
2. T. Halkin, Brain Tumors: Facts & Figures up to May 2018: Incidence, Mortality, and Survival. *National Brain Tumor Society* http://blog.braintumor.org/brain-tumor-facts-figures-may-2018-incidence-mortality-and-survival-in-2018/, (2018).
3. D. N. Louis *et al.*, The 2016 World Health Organization Classification of Tumors of the Central Nervous System: a summary. *Acta Neuropathol* **131**, 803-820 (2016).
4. R. Stupp *et al.*, Radiotherapy plus concomitant and adjuvant temozolomide for glioblastoma. *The New England journal of medicine* **352**, 987-996 (2005).
5. P. Zhu, X. L. Du, G. Lu, J. J. Zhu, Survival benefit of glioblastoma patients after FDA approval of temozolomide concomitant with radiation and bevacizumab: A population-based study. *Oncotarget* **8**, 44015-44031 (2017).
6. E. S. Newlands *et al.*, Phase I trial of temozolomide (CCRG 81045: M&B 39831: NSC 362856). *British Journal Of Cancer* **65**, 287 (1992).
7. J. Zhang, M. F. Stevens, T. D. Bradshaw, Temozolomide: mechanisms of action, repair and resistance. *Curr Mol Pharmacol* **5**, 102-114 (2012).
8. P. Karran, R. Hampson, Genomic instability and tolerance to alkylating agents. *Cancer Surv* **28**, 69-85 (1996).
9. A. Thomas *et al.*, Temozolomide in the Era of Precision Medicine. *Cancer Res* **77**, 823-826 (2017).
10. G. Lu *et al.*, Triple-drug Therapy With Bevacizumab, Irinotecan, and Temozolomide Plus Tumor Treating Fields for Recurrent Glioblastoma: A Retrospective Study. *Front Neurol* **10**, 42 (2019).

11. H. S. Friedman *et al.*, Bevacizumab alone and in combination with irinotecan in recurrent glioblastoma. *Journal of clinical oncology : official journal of the American Society of Clinical Oncology* **27**, 4733-4740 (2009).

12. T. N. Kreisl *et al.*, Phase II trial of single-agent bevacizumab followed by bevacizumab plus irinotecan at tumor progression in recurrent glioblastoma. *Journal of clinical oncology : official journal of the American Society of Clinical Oncology* **27**, 740-745 (2009).

13. M. R. Gilbert *et al.*, A randomized trial of bevacizumab for newly diagnosed glioblastoma. *The New England journal of medicine* **370**, 699-708 (2014).

14. O. L. Chinot *et al.*, Bevacizumab plus radiotherapy-temozolomide for newly diagnosed glioblastoma. *The New England journal of medicine* **370**, 709-722 (2014).

15. M. S. Lesniak, H. Brem, Targeted therapy for brain tumours. *Nature Reviews Drug Discovery* **3**, 499 (2004).

16. M. Westphal *et al.*, A phase 3 trial of local chemotherapy with biodegradable carmustine (BCNU) wafers (Gliadel wafers) in patients with primary malignant glioma. *Neuro Oncol* **5**, 79-88 (2003).

17. S. A. Chowdhary, T. Ryken, H. B. Newton, Survival outcomes and safety of carmustine wafers in the treatment of high-grade gliomas: a meta-analysis. *Journal of Neuro-Oncology* **122**, 367-382 (2015).

18. K. E. Parrish, J. N. Sarkaria, W. F. Elmquist, Improving drug delivery to primary and metastatic brain tumors: strategies to overcome the blood-brain barrier. *Clin Pharmacol Ther* **97**, 336-346 (2015).

19. T. Shapira-Furman *et al.*, Biodegradable wafers releasing Temozolomide and Carmustine for the treatment of brain cancer. *J Control Release* **295**, 93-101 (2019).

20. B. Urciuoli, Optune Combination Improves Survival in Glioblastoma. *Cure Today* https://www.curetoday.com/articles/optune-combination-improves-survival-in-glioblastoma, (2017).
21. R. Stupp *et al.*, Effect of Tumor-Treating Fields Plus Maintenance Temozolomide vs Maintenance Temozolomide Alone on Survival in Patients With Glioblastoma: A Randomized Clinical Trial. *JAMA* **318**, 2306-2316 (2017).
22. B. Al-Lazikani, U. Banerji, P. Workman, Combinatorial drug therapy for cancer in the post-genomic era. *Nat Biotechnol* **30**, 679-692 (2012).
23. M. Weller, T. Cloughesy, J. R. Perry, W. Wick, Standards of care for treatment of recurrent glioblastoma--are we there yet? *Neuro Oncol* **15**, 4-27 (2013).
24. W. Taal *et al.*, Single-agent bevacizumab or lomustine versus a combination of bevacizumab plus lomustine in patients with recurrent glioblastoma (BELOB trial): a randomised controlled phase 2 trial. *Lancet Oncol* **15**, 943-953 (2014).
25. W. Wick *et al.*, Lomustine and Bevacizumab in Progressive Glioblastoma. *The New England journal of medicine* **377**, 1954-1963 (2017).
26. K. B. Peters *et al.*, Phase II Trial of Upfront Bevacizumab, Irinotecan, and Temozolomide for Unresectable Glioblastoma. *Oncologist* **20**, 727-728 (2015).
27. J. J. Vredenburgh *et al.*, The addition of bevacizumab to standard radiation therapy and temozolomide followed by bevacizumab, temozolomide, and irinotecan for newly diagnosed glioblastoma. *Clin Cancer Res* **17**, 4119-4124 (2011).
28. T. R. Hummel *et al.*, A pilot study of bevacizumab-based therapy in patients with newly diagnosed high-grade gliomas and diffuse intrinsic pontine gliomas. *J Neurooncol* **127**, 53-61 (2016).
29. S. K. Gupta, R. P. Nayak, Off-label use of medicine: Perspective of physicians, patients, pharmaceutical companies and regulatory authorities. *J Pharmacol Pharmacother* **5**, 88-92 (2014).

30. J. E. Kim *et al.*, Combination Therapy with Anti-PD-1, Anti-TIM-3, and Focal Radiation Results in Regression of Murine Gliomas. *Clin Cancer Res* **23**, 124-136 (2017).

31. M. Martikainen, M. Essand, Virus-Based Immunotherapy of Glioblastoma. *Cancers (Basel)* **11**, (2019).

32. B. D. Choi, M. V. Maus, C. H. June, J. H. Sampson, Immunotherapy for Glioblastoma: Adoptive T-cell Strategies. *Clin Cancer Res*, (2018).

33. T. M. Law *et al.*, Phase III randomized trial of interleukin-2 with or without lymphokine-activated killer cells in the treatment of patients with advanced renal cell carcinoma. *Cancer* **76**, 824-832 (1995).

34. B. D. Choi, W. T. Curry, B. S. Carter, M. V. Maus, Chimeric antigen receptor T-cell immunotherapy for glioblastoma: practical insights for neurosurgeons. *Neurosurg Focus* **44**, E13 (2018).

35. D. M. O'Rourke *et al.*, A single dose of peripherally infused EGFRvIII-directed CAR T cells mediates antigen loss and induces adaptive resistance in patients with recurrent glioblastoma. *Sci Transl Med* **9**, (2017).

36. N. Ahmed *et al.*, HER2-Specific Chimeric Antigen Receptor-Modified Virus-Specific T Cells for Progressive Glioblastoma: A Phase 1 Dose-Escalation Trial. *JAMA Oncol* **3**, 1094-1101 (2017).

37. C. E. Brown *et al.*, Bioactivity and Safety of IL13Ralpha2-Redirected Chimeric Antigen Receptor CD8+ T Cells in Patients with Recurrent Glioblastoma. *Clin Cancer Res* **21**, 4062-4072 (2015).

38. T. M. Johanns *et al.*, Immunogenomics of Hypermutated Glioblastoma: A Patient with Germline POLE Deficiency Treated with Checkpoint Blockade Immunotherapy. **6**, 1230-1236 (2016).

39. E. Bouffet *et al.*, Immune Checkpoint Inhibition for Hypermutant Glioblastoma Multiforme Resulting From Germline Biallelic Mismatch Repair Deficiency. *Journal of clinical*

oncology : official journal of the American Society of Clinical Oncology **34**, 2206-2211 (2016).

40. A. Samson *et al.*, Intravenous delivery of oncolytic reovirus to brain tumor patients immunologically primes for subsequent checkpoint blockade. *Sci Transl Med* **10**, (2018).
41. A. Desjardins *et al.*, Recurrent Glioblastoma Treated with Recombinant Poliovirus. **379**, 150-161 (2018).
42. F. F. Lang *et al.*, Phase I Study of DNX-2401 (Delta-24-RGD) Oncolytic Adenovirus: Replication and Immunotherapeutic Effects in Recurrent Malignant Glioma. *Journal of clinical oncology : official journal of the American Society of Clinical Oncology* **36**, 1419-1427 (2018).
43. T. F. Cloughesy *et al.*, Durable complete responses in some recurrent high-grade glioma patients treated with Toca 511 + Toca FC. *Neuro Oncol* **20**, 1383-1392 (2018).
44. J. Cohen, IL-12 Deaths: Explanation and a Puzzle. **270**, 908-908 (1995).
45. Y. E. Seo, T. Bu, W. M. Saltzman, Nanomaterials for convection-enhanced delivery of agents to treat brain tumors. *Curr Opin Biomed Eng* **4**, 1-12 (2017).

Chapter 1

Enhancing therapeutic delivery to the brain via convection enhanced delivery

Abstract

Convection enhanced delivery (CED) is an attractive method to bypass the blood-brain barrier for therapeutic delivery to the brain as well as to facilitate widespread therapeutic distribution within brain parenchyma by creating a continuous pressure-driven bulk flow. However, rapid removal of therapeutics from the brain by the physiological clearance mechanism remains a critical challenge to achieving widespread therapeutic delivery by CED. Nanoparticle (NP)-based delivery systems that stay longer in the brain while convoying a high concentration of payloads can potentially provide widespread and efficient therapeutic delivery to the highly disseminated disease areas within the brain. We have recently demonstrated that CED of NPs designed to efficiently penetrate the highly adhesive and nanoporous brain extracellular matrix synergistically enhances the payload distribution within healthy and tumor-bearing brains. In this chapter, we overview the mechanism and current limitations of CED, as well as strategies to maximize the CED-mediated therapeutic and/or NP delivery to the brain. We then describe a detailed methodology for preclinical CED experiments, including device/animal set-up, NP preparation, tissue processing and image/data analysis. Finally, we conclude the chapter with a few troubleshooting tips.

1. Introduction

1.1 Key challenge to therapeutic delivery to the brain - limited therapeutic distribution

The blood-brain barrier (BBB) is a primary impediment to the delivery of systemically administered therapeutic agents to the brain (*1*). Strategies to overcome the BBB have been widely explored and pre-clinically validated, including transient BBB opening via chemical (*2*) or physical (*3-5*) methods and circumvention of the barrier by local infusion (*6, 7*). The conventional strategy to bypass the BBB involves direct intracerebroventricular or intrathecal injection of therapeutics into lateral ventricles of the brain or into the lumbar spine where the cerebrospinal fluid (CSF) circulates, respectively (*8*). However, an additional challenge, regardless of the route of administration, is to achieve widespread therapeutic distribution in the brain (*9*). It is now well established that simple diffusion-mediated dispersion of conventional therapeutics, including small molecule-, and protein-based drugs, do not provide widespread coverage throughout highly disseminated disease areas within the brain parenchyma (*10, 11*). In addition to the slow diffusion rates, the rapid drug clearance by convective flow of the CSF, from brain tissue to bloodstream, remains a contributor to the suboptimal drug distribution and their local retention (*12*). The human CSF is produced at a rate of 550 mL/day, with ~100-140 mL of CSF turning over every 4 - 5 hours (*13*). Thus, injected drugs carried by the interstitial fluid bulk flow are continuously destine to the CSF and subsequently eliminated from the brain parenchyma by the physiological CSF turnover (*9*).

Due to the combined effect of slow diffusion and rapid clearance, the concentrations of locally injected drugs have been estimated to decrease by ~10-folds for every millimeter of the traveled distance from the site of administration (*10, 14, 15*). This decrease in drug concentrations augments with the increase in the molecular weight or size of the molecule (*16*), which is primarily attributed to the reduction in the diffusion rates, as expected from the Stokes-Einstein diffusion equation. The bis-chloroethylnitrosourea (BCNU) wafer, Gliadel®, developed and clinically used to provide sustained drug concentrations within the brain also suffers from a

similar reality; it has been reported that the BCNU concentration reduces by ~10-folds every 500 μm of distance away from the wafer (*17*). Thus, the amount of drug necessary to achieve therapeutic concentration only a few millimeters away from the site of administration would be several orders of magnitude greater than its effective therapeutic dose. The required drug dose can be even greater, noting that the overall distance that needs to be traveled by injected drugs can be as far as ~50 mm or more depending on the administration site (*10*). Such drug doses will most likely lead to significant toxicity, thereby demanding a safer method to achieve therapeutic concentrations throughout the target diseased areas within the brain.

1.2 Convection enhanced delivery as a strategy to enhance distribution in the brain

Convection enhanced delivery (CED) was initially introduced and implemented as a mean to bypass the BBB in early 1990s (*18*), but has later become appreciated as a strategy to facilitate widespread distribution of locally infused therapeutics (*19-22*). The CED involves continuous infusion of a solution into the brain at a predetermined rate (*23*). The procedure creates a pressure-driven bulk flow that pushes the infusate away from the administration site into the extracellular space of the brain parenchyma (*23, 24*). Thus, CED provides a markedly enhanced volumetric drug distribution within the brain as it is primarily mediated by convection, unlike the bolus injection that entirely counts on non-directional random diffusion (Figure 1.1) (*25, 26*).

In addition, instantaneous pressure build-up is avoided by the CED due to the slow infusion, which reduces reflux that inevitably occurs during bolus injection (*23*). Further, the gradual infusion of CED can potentially mitigate systemic toxicity of therapeutic agents by reducing the amount of drugs exposed to the systemic circulation at a given time (*21, 27*). These unique advantages offered by CED have prompted the use of the technique for localized chemotherapeutic delivery to treat malignant gliomas, primarily glioblastoma multiforme (*28, 29*) and diffuse intrinsic pontine glioma (*24, 30*), of which recurrence generally occurs as far as centimeters away from the primary tumor site (*31*).

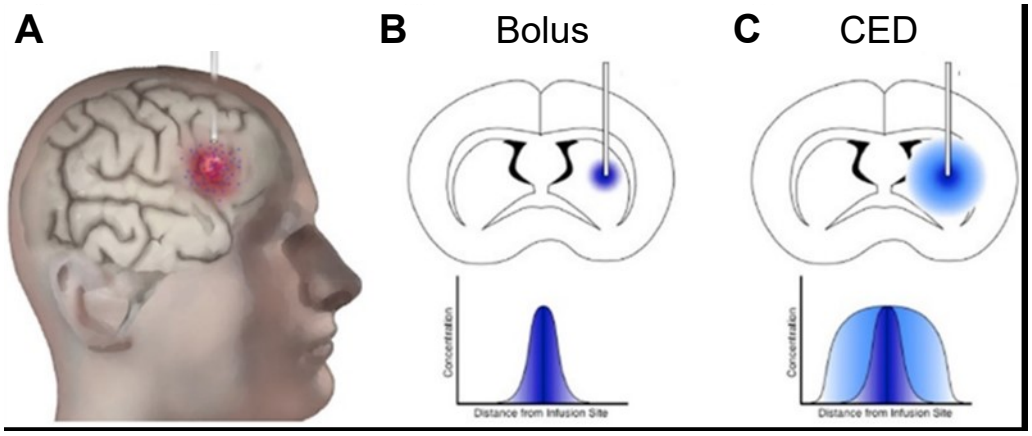

Figure 1.1: Volume of distribution achieved by bolus injection versus CED. (A) A catheter is inserted into the brain tumor (red) or a cavity created after tumor resection, and therapeutic agents (blue) are continuously infused. Schematics (upper panel) and diffusion profiles (i.e. concentration gradients away from the administration site; lower panel) of therapeutic agents (blue) administered by **(B)** bolus injection and **(C)** CED. The CED provides a marked greater therapeutic distribution compared to bolus injection that counts solely on simple diffusion. CED Reproduced from Seo, Y.E. et al. 2017 with permission from Elsevier.

The CED has been also explored in various preclinical and/or clinical settings for treatment or diagnosis of other brain diseases beyond tumors, including neurodegenerative diseases, epilepsy, stroke, traumatic injuries and brainstem lesions (*32-37*). Specifically, the utility of CED has been expanded to achieve widespread delivery of a wide array of therapeutic or diagnostic agents, including monoclonal antibodies, therapeutic toxins, proteins, imaging tracers as well as drug and gene delivery systems (*7, 18, 21, 38-40*). Table 1.1 lists general advantages and disadvantages around the use of CED in comparison to other local or systemic administration modalities commonly applied to brain delivery.

Table 1.1: Advantages and disadvantages of CED.

Advantages	Disadvantages
• Bypasses BBB • Reduces risk of local and systemic toxicity • Widespread and uniform delivery of agents by pressure-driven continuous bulk flow • Distribution minimally affected by molecular weights of agents	• Relatively invasive procedure • Prolonged infusion times • Potential build-up of intracranial pressure • Requires refilling for a long-term infusion

• Less prone to human errors • Reduces backflow	

1.3 Challenges for therapeutic distribution in the brain by CED

While the CED provides a method to enhance drug distribution within the brain, multiple studies have revealed that the benefit is rapidly lost due to the physiological fluid clearance mechanism described above (*23, 25, 41*). It has been reported that the peak volume of drug distribution precipitously reduces as early as 30 minutes after CED and drugs are often found completely removed from the brain within a few hours (*42*). Of note, the clearance is even greater in the brains of patients with diseases characterized by increased vascular permeability and interstitial pressure, such as tumors (*43-45*).

One of the methods to circumvent the clearance problem involves prolonging the infusion of therapeutic agents over days using an implantable catheter, which has shown proof-of-principle benefits in treating brain tumors (*46-51*). However, widespread clinical use of this long-term infusion modality is limited by potential risk of infection and mechanical injury, need for constant monitoring of drug toxicity and complex and high-cost catheter design. As an alternative approach, nanoparticle (NP)-based delivery systems have been widely explored in preclinical settings to provide sustained therapeutic concentrations in the brain. Due to their larger sizes, therapeutic NPs carrying a high concentration of payloads delivered into the brain parenchyma stay longer without being rapidly cleared unlike drugs administered “naked” (*52, 53*). NPs can carry and deliver controlled release of various types of payloads, ranging from small molecule drugs to biological macromolecules (*39, 53, 54*). Further, NPs can be designed to facilitate specific cell targeting and subsequent uptake (*54, 55*), providing another mechanism by which rapid drug clearance from the brain is avoided.

While NPs can potentially delay the drug clearance, released payloads spread in the brain via slow diffusion remains identical to directly injected naked drugs. Thus, NPs must broadly disperse throughout the brain parenchyma via CED, followed by timely release of payloads, to

provide widespread therapeutic coverage within the brain. However, widespread NP distribution is not readily achieved due to the presence of highly adhesive and nanoporous brain extracellular matrix (ECM) that fills the brain extracellular space through which NPs spread in the brain (*56, 57*). The brain ECM is composed of negatively charged or hydrophobic macromolecules, including hyaluronic acids, proteoglycans, glycosaminoglycans and fibrous proteins (*58-60*), which hampers NP transport in the brain via multivalent adhesive interactions such as electrostatic and hydrophobic interactions (*56, 61*). In addition, these macromolecules form a dense meshwork, rendering the ECM a steric barrier to NP diffusion within the brain (*39, 54, 56*). The pore sizes of the brain ECM has been previously estimated to be 38 - 64 nm (*62*), but we have recently re-evaluated them using non-adhesive probes to be as large as or potentially greater than 110 nm (*56*). Physicochemical barrier properties of the ECM within tumor tissues are most likely distinct from those of normal ECM due to significant changes in cellularity and macromolecular compositions that are highly varied depending on the type of tumor (*63-65*). There have been several reports suggesting that the pore sizes of tumor ECM may be smaller than 100 nm (*62, 66*). Of note, interstitial pressure build-up in tumor tissues (*44, 67*) often promotes outward brain tumor cell migration and consequently, greater volume of therapeutic distribution is likely needed (*39, 67-69*).

1.4 Strategies to enhance NP distribution in the brain following CED

As described above, brain ECM is an adhesive and steric barrier to NP diffusion. Thus, NPs possessing small particle diameters to fit through the ECM pores as well as non-adhesive surface coatings that resist adhesive interactions with ECM components would be able to penetrate the brain tissue. Indeed, we have previously demonstrated that NPs as large as ~110 nm efficiently penetrate rodent and human brain parenchyma *ex vivo* and *in vivo*, but only if the particle surfaces are densely passivated with hydrophilic and neutrally charged polyethylene glycol (PEG) (Figure 1.2) (*56*). Specifically, NPs possessing diameters of ~100 nm were shown to efficiently diffuse through normal brain ECM when their surfaces were coated with PEG at the

surface densities of ≥ 8 PEG molecules per 100 nm^2 particle surface area (*56*). However, minimal surface PEG density cut-off may vary depending on particle size due to the difference in surface curvature. We also note that smaller particle diameters may be needed for efficient NP penetration through tumor ECM meshes. More recently, we found that CED of this "brain-penetrating" NP (BPN) resulted in widespread distribution in healthy or tumor-bearing brain striatum; in contrast, the distribution of similarly sized uncoated or conventionally PEGylated NPs was confined to the site of administration despite the pressure-driven convective flow provided by the CED (*38, 65, 70-74*). Importantly, NPs must retain the physicochemical properties required for efficient brain penetration in the physiological brain environment (i.e. brain interstitial fluid or CSF).

The physicochemical properties and stability that allow efficient brain penetration are likely applicable commonly to nano-scale particulate matters regardless of type of core materials, including polymers, lipids and inorganic compounds. We have previously demonstrated that BPNs formulated with chemically distinct core polymers equally provide widespread distribution in rodent brain tissue *in vivo* following CED (*38, 65, 70-72, 74*). Other than PEG, various coating materials have been used to endow NP-based delivery systems with colloidal stability; those include but are not limited to sugars, pluronics, polyglycerols, polyacrylic and polyvinyl polymers (*75, 76*). However, these materials, often possessing chemical properties similar to PEG (i.e. hydrophilic and neutrally charged), can potentially be utilized to engineer BPNs although it is yet to be experimentally determined. We note that while not necessarily geared specifically towards creating NPs capable of penetrating brain ECM, a variety of NPs have been preclinically investigated in conjunction with CED. Interested readers are referred to a recent review article (*54*).

Adhesive NPs small enough to avoid steric obstruction imposed by the brain ECM can widely spread throughout the brain parenchyma following CED if NPs are administered at a very high concentration (*38*). Specifically, CED of uncoated NPs administered at 25 mg/ml exhibited

the volumetric distribution approaching that achieved by identically administered BPN at 0.1 mg/ml (*38*). This phenomenon is likely due to potential masking of the adhesive moieties of ECM by an excess of adhesive NPs, thereby enabling the residual NPs to pass through the ECM pores without being associated with ECM meshes. However, it should be noted that this approach is likely prone to dose-limiting toxicity, particularly when payloads possess intrinsic toxicity such as chemotherapeutic agents.

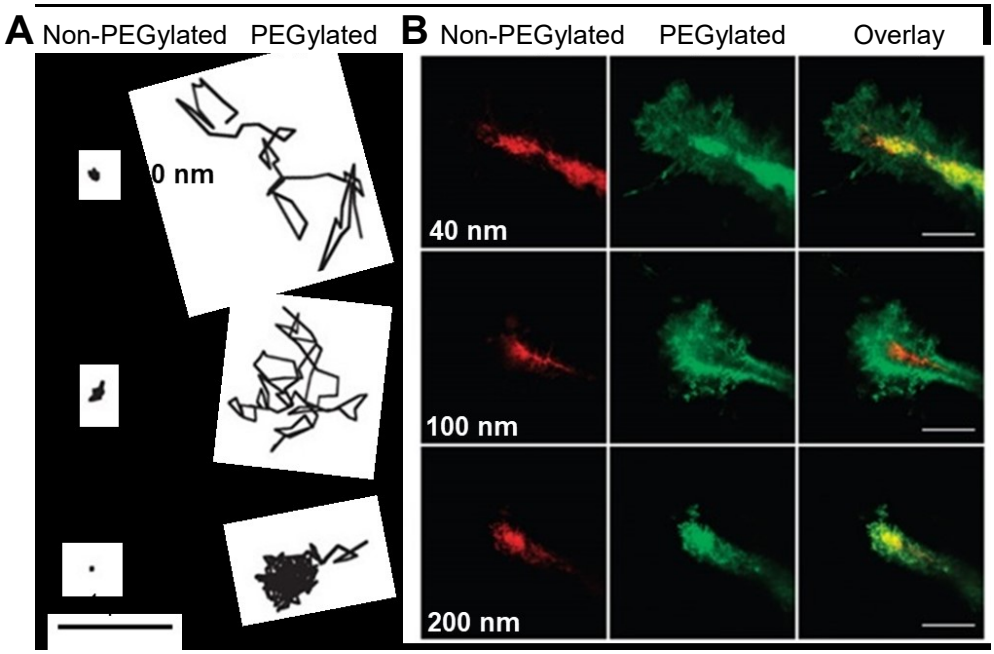

Figure 1.2: Ex vivo diffusion and in vivo distribution of nanoparticles (NPs) in human and rodent brain tissues. (A) Representative particle trajectories for non-PEGylated (i.e. adhesive) and PEGylated (i.e. non-adhesive) NPs of various sizes in brain tissues freshly harvested from humans. **(B)** Direct comparisons of the distribution of non-PEGylated (red) and PEGylated (green) NPs of various sizes following intracranial co-injection into mouse brains. Scale bar = 50 μm. Reproduced from Nance, E. et al. 2012 with permission from The American Association for the Advancement of Science.

Alternatively, NP distribution in the brain following CED can be enhanced by manipulating the barrier properties of ECM. In particular, the pore sizes can be transiently modulated by chemical or physical methods. As an example, we have recently reported that distribution of BPNs in rodent brain following CED significantly increases when administered in a hyperosmotic solution (*38*). This is most likely attributed to the mechanism described in a prior

study that hyperosmolar saline administered in brain tissue leads to enlargement of the ECM mesh spacings as water is drawn out of cells into the extracellular space via an osmotic gradient established by the hyperosmolar saline (*77, 78*). Likewise, it has been recently demonstrated that focused ultrasound, by transiently enlarging the extracellular space, can enhance NP dispersion in the brain (*79*).

1.5 CED in clinical trials

Previous and ongoing clinical trials involving the implementation of CED for treating diseases affecting the central nervous system (CNS) are listed in Table 1.2. Presumably due to the somewhat invasive nature of the procedure, most (i.e. 37 out of 41) of trials were conducted in patients with malignant gliomas who were already receiving surgery. The rest covers neurodegenerative disorders, including Parkinson's disease (NCT01621581, NCT00921128), aromatic L-amino acid decarboxylase (AADC) deficiency (NCT02852213) (*80, 81*) and Gaucher disease (*82*). A majority of trials to date involve delivery of naked therapeutic agents for cancer therapy (*21*), but the number of trials that include delivery systems is increasing, particularly regarding gene therapy applications. Specifically, viruses (NCT02852213, NCT01621581) and liposomes (*83-86*) have been or are currently being explored in clinical settings to achieve widespread therapeutic transgene expression following CED.

Table 1.2: Clinical trials conducted to evaluate CED for treating CNS diseases as of late 2018.

Target Disease	Therapeutic Agent	Year	Trial Phase	Current Status	NCT#	Reference
Malignant gliomas	124I-8H9	2011-present		Recruiting	NCT01502917	-
	Carboplatin	2015	I	Withdrawn	NCT01317212	(*87*)
		2012-2017		Recruiting	NCT01644955	-
	Cotara	2005	I/II	Completed	-	(*88*)
	CpG-28	2005-2008			NCT00190424	(*89, 90*)
	D2C7-IT	2015-present	I	Recruiting	NCT02303678	(*91*)

Delta-24-rgd	2010-2014	I/II	Completed	NCT01582516	-
GRm13Z40-2 CTL	2010-2013	I		NCT01082926	(*92*)
hrBMP4	2017-present		Recruiting	NCT02869243	-
HSV-1-tk[1] + ganciclovir	2003	I/II		-	(*83*)
IL13-PE38QQR	2000-2007		Completed	NCT00024570	(*93*)
	2001-2006	I		NCT00024557	(*94*)
	2004-2007	III		NCT00076986	(*95, 96*)
IL13-PE38QQR + temozolomide	2009-2015	I	Terminated	NCT00880061	(*97*)
	2004-2007		Completed	NCT00089427	(*98*)
LSFV-IL12[1]	2003	I/II		-	(*84*)
mAb 425	1997	I		-	(*99*)
MDNA55	2016-present	II	Recruiting	NCT02858895	-
MR1-1KDEL	2006-2012		Terminated	NCT01009866	-
Irinotecan[1]	2014-present	I	Enrolling by invitation	NCT02022644	(*86*)
	2017-present		Recruiting	NCT03086616	-
NBI-3001	2003		Completed	NCT00014677	(*100*)
Nimustine hydrochloride	2011		-	-	(*101*)
Paclitaxel	2001, 2004	I/II	Completed	-	(*102, 103*)
PRX321	2009-2010	II	Withdrawn	NCT00797940	-
PVS-RIPO	2012-2017	I	Active, not recruiting	NCT01491893	(*104*)
	2017-present		Recruiting	NCT03043391	-
TF-CRM107	1997	I/II	Completed	-	(*105*)
	2003			-	(*106*)

		2004-2011			NCT00308165	(*30, 48, 50*)
		2018-present		Recruiting	NCT03154996	-
	Topotecan	2014-2015	I	Completed	NCT02278510	(*107*)
		2015-present		Recruiting	NCT02500459	-
		2017-present			NCT03193463	-
	TP-38	2004-2007	I/II	Completed	NCT00104091	(*108*)
	Trabedersen	2008-2012	III	Terminated	NCT00761280	-
		2003-2009	II	Completed	NCT00431561	(*109*)
PD	AAV2-GDNF[2]	2012-present	I	Active, not recruiting	NCT01621581	-
	Muscimol	2009		Withdrawn	NCT00921128	-
Type 2 Gaucher Disease	Glucocerebrosidase	2005-2006	I	Completed	NCT00244582	(*82*)
AADC Deficiency	AAV2-hAADC[2]	2016-present	I	Recruiting	NCT02852213	-

[1]liposomal formulations
[2]adeno-associated virus (AAV)

2. Materials and Methods

2.1 CED Apparatus

The CED apparatus is composed of two main components, including the ultra-precise rodent “U”-stereotaxic frame (Stoelting, Wood Dale, IL) and the Chemyx Nanojet injector module (Chemyx, Stafford, TX) (Figure 1.3). The primary components of the stereotaxic frame are (a) non-rupture ear bars, which help place rodent head flat and parallel to the table of operation, (b) 100 micron 3-axes manipulator arm, which allows movement of a probe holder in x-, y- and z-axis directions (measured in mm), (c) a corner clamp probe holder that grips the syringe header and (d) an adaptor where the rodent head is placed. The second component of

the CED apparatus, injection module, consists of (e) Nanojet control box where infusion parameters, including infusion rate, volume and type of syringe, are selected and (f) Nanojet syringe header, which is connected to the control box and holds the syringe in place. We also refer this part to “injector”, as it controls the infusion rates as programmed by the control box.

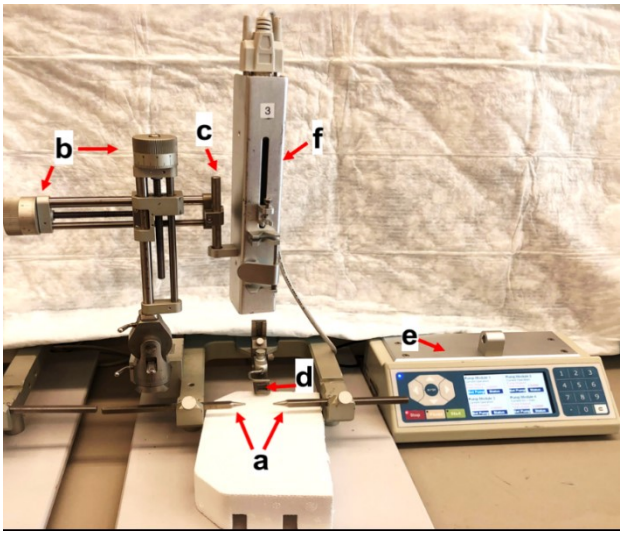

Figure 1.3: CED apparatus. The CED device is composed of two distinct functional compartments, including structural (i.e. stereotaxic frame) and injection (injection module) elements. The primary components of the former include **(a)** non-rupture ear bars, **(b)** 100 micron 3-axes manipulator arm, **(c)** a corner clamp probe holder and **(d)** an adaptor. The latter is composed of **(e)** Nanojet control box and **(f)** Nanojet syringe header or injector.

2.2 Syringe and cleaning solutions

The infusate solution carrying therapeutics or NPs is loaded into a 5 or 50 µL Hamilton Neuros syringe (Hamilton, Reno, NV) connected to a 33-gauge needle for treating mice or rats, respectively. This syringe is designed to endow an enhanced needle rigidity specifically for applications to brains, which allows infusion of a micro-volume of fluid precisely into a desired location within the brain while minimizing the risk of injection site damage (*110*). There are five different types of needle catheters used in CED, including end-port catheter, multi-port catheter, porous-tipped catheter, balloon-tip catheter and stepped-down catheter (*111*) (see (*21*) for details). We routinely use the stepped-down catheter designed to allow feasible adjustment of a Hamilton Neuros syringe. This catheter is composed of a needle sleeve with or without a blind stop and a needle that passes through the sleeve hollow. The distance between the sleeve end and needle tip or the length of the needle exposed from the sleeve end is defined as the step distance, which can be manually adjusted to range 1 to 20 mm (*112*). For the former set-up

(with a blind stop), the step distance is pre-determined and maintained by the sleeve-end blind stop placed on top of the skull during the administration. In contrast, needle sleeve of the latter passes through the burr hole and the step distance can be subsequently adjusted for desired stereotaxic applications. The term “stepped” originated from a sharp dimensional transition from the wider needle sleeve to a narrower needle (*112*). Of note, a 1-mm step distance has been previously optimized to minimize the possibility of reflux and leakage in rodent brain (Figure 1.4) (*112*), and thus most widely employed for CED application.

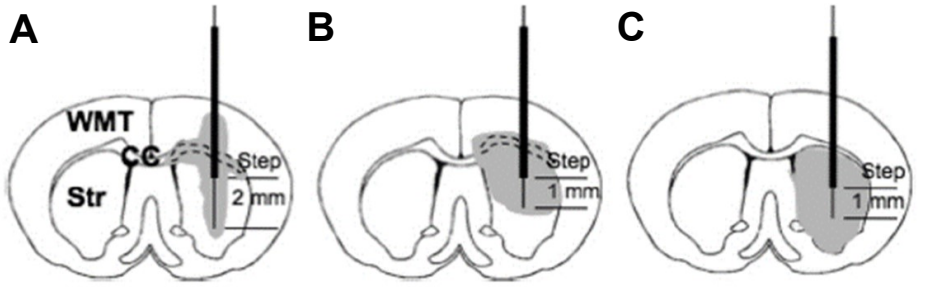

Figure 1.4: Adjustment of stepped-down catheter for optimal infusion into the striatum. (A) Either a long (i.e. 2 mm) step distance or **(B)** an optimal 1-mm step distance with a short cortical distance (i.e. distance between cerebral cortex and catheter step or the end of needle sleeve) increases the probability of reflux and/or leak, leading to a suboptimal infusate distribution (gray shade). **(C)** A 1-mm step distance with a longer cortical distance minimizes the probability of reflux and/or leakage, thereby leading to a greater infusate distribution. *Reproduced from Yin, D. et al. 2010 with permission from Elsevier.*

A fresh solvent used to carry and administer therapeutics and/or NPs (e.g. ultrapure water, medical-grade saline, etc.) is utilized to rinse the syringe between sequential infusions when multiple CED experiments are involved. A biodegradable and non-detergent-based cleaning agent such as the Cleaning Solution Concentrate (Hamilton, Reno, NV) is used to rigorously wash the syringe and needle upon the completion of CED experiments in order to avoid potential clogging and/or contamination. Ultrapure water in conjunction with ethanol or acetone are used for final wash.

2.3 Preparation of NPs and infusate solutions

Based on aforementioned physicochemical design criteria required for efficient brain tissue penetration (see section 1.4; (*54, 56*)), we have engineered numerous BPN formulations for delivery of a wide array of payloads, ranging from small molecule chemotherapeutics (*63, 74*) to

reporter or therapeutic nucleic acids (*65, 71, 72*). For the purpose of this chapter, however, we use commercially available latex beads possessing highly controlled particle diameters and defined surface chemistries as a model therapeutic delivery NP. In particularly, we utilize fluorescently labeled carboxylated polystyrene beads (PS-COOH) (Life Technologies, Grand Island, NY) to engineer model BPNs (i.e. PS-PEG) (*56*), while the unmodified PS-COOH NPs serve as a conventional control that readily interacts with brain ECM components and thus cannot efficiently penetrate the brain parenchyma (*56*). Methoxy-PEG-NH_2 (5 kDa; Creative PEGWorks, Durham, NC), N-hydroxysulfosuccinimide (NHS; Sigma, St. Louis, MO), 1-ethyl-3-(3-dimethylaminopropyl) carbodiimide (EDC; Invitrogen, Carlsbad, CA) and 200 mM sterile sodium borate buffer pH 8.2 (Growcells, Irvine, CA) are used to synthesize model BPNs possessing dense surface PEG coatings. All NPs are washed in Amicon Ultra-0.5 mL 100 K MW filters (Millipore Sigma, Burlington, MA), and characterized with a Zetasizer NanoZS (Malvern Instruments, Columbia, MD) and ^{1}H NMR (400 MHz; REM400; Bruker, Billerica, MA).

Saline-based infusate solutions possessing different osmolality are prepared in ultrapure DNase/RNase-free water (ThermoFischer Scientific, Waltham, MA) and filtered through a 0.20 µm sterile syringe filter (Corning Incorporated, Corning, NY). Specifically, we use 0.9% (~300 mOsm/kg) or 3% (~1000 mOsm/kg) NaCl solution as an isotonic or hypertonic infusate solution, respectively. Osmolality is measured using the Vapro® Vapor Pressure Osmometer (EliTech Wescor, Logan, UT).

2.4 Animal Set-up

While technically any type of rodents can be used, we routinely conduct CED experiments with two different strains each for mice (20 – 30 g), including CF-1 (Jackson Laboratory, Bar Harbor, ME) and C57BL/6J mice (Charles River, Wilmington, MA), and rats (120 – 200 g), including Fischer 344 and Sprague Dawley rats (Harlan Laboratories, Frederick, MD). Of note, inbred rodents are often preferred when an identical genetic background is desired, such as in case of gene therapy applications (*113*). Animals are housed in a standard animal

husbandry facility and are given a free access to food and water. All animals are treated in accordance with the policies and guidelines of the Johns Hopkins University Animal Care and Use Committee.

A mixture of ketamine and xylazine is used to anesthetize rodents as routinely conducted (*114*). Optixcare eye lubricant (CLC Medica, Ontario, Canada) and Betadine® antiseptic solution (Purdue Pharma L.P., Stamford, CT) are used for lubricating eyes and sterilizing skin, respectively, prior to surgery. A scalpel (Aspen Surgical, Caledonia, MI) equipped with a sterile surgical blade (Cincinnati Surgical, Cincinnati, OH) is used to create a midline scalp incision, and a micro-drill (Harvard Apparatus, Holliston, MA) is utilized to make a small 1.0-mm burr hole through the rodent skull. We use biodegradable sutures (Polysorb Braided Absorbable Sutures 5-0; Medtronic, Minneapolis, MN) to seal the incision and bacitracin as a topical antibiotic, following CED experiments.

2.5 Tissue processing and confocal microscopy

For brain tissue fixation and cryoprotection, we use a ready-to-use working solution composed of 4 % formaldehyde (i.e. equivalent to 10% formalin) dissolved in a phosphate buffer (Sigma-Aldrich, St. Luis, MO) and gradient sucrose (Sigma-Aldrich, St. Luis, MO) solutions prepared by dissolving sucrose in Dulbecco's phosphate-buffered saline (DPBS, 1X) (Corning™, Manassas, VA) at 10%, 20%, and 30% w/v, respectively. Tissue-Tek optimal cutting temperature (OCT) compound (Sakura Finetek, Torrance, CA) is used to prepare frozen tissue samples for subsequent cryosection with a research cryostat (model CM3050 S, Leica Biosystems, Buffalo Grove, IL). Dako fluorescence mounting medium (Dako, Carpinteria, CA) is utilized to mount cryosectioned brain tissue slices. Confocal microscopy of the tissue slices is conducted by using a Zeiss LSM 710 confocal laser scanning microscope (Carl Zeiss Microscopy, Jena, Germany) equipped with a 5x/0.25 M27 air objective (Carl Zeiss Microscopy, Jena, Germany). We use Metamorph® image analysis software (Metamorph, Sunnyvale, CA),

ImageJ (NIH, Bethesda, MD) and Imaris (Bitplane, South Windsor, CT) for image analysis and/or reconstruction.

The outcomes of CED applications are contingent to the selection of different variables, including device arrangement, infusion parameters, brain coordinates and NP design. We here describe how we adjust these variables to achieve widespread distribution of model NPs following CED in rodent brains.

2.6 CED device arrangement

To ensure consistent and stable infusions, each component of the CED apparatus must be assembled and adjusted properly following the manufacturer's manual. While the syringe header (i.e. injector) presses the syringe plunger for infusion as programmed by the control box, all other components should be fully stabilized. Specifically, it is critical to securely fasten the base of the 3-axes manipulator arm to avoid its rotation and the corner clamp probe holder to firmly hold the syringe header during the procedure (Figure 1.5). In addition, the screw on the syringe header must be fastened to ensure that a syringe is tightly associated with the header during the infusion. The stereotaxic frame must be placed on a flat surface on which a rodent is laid face-down for a subsequent CED experiment.

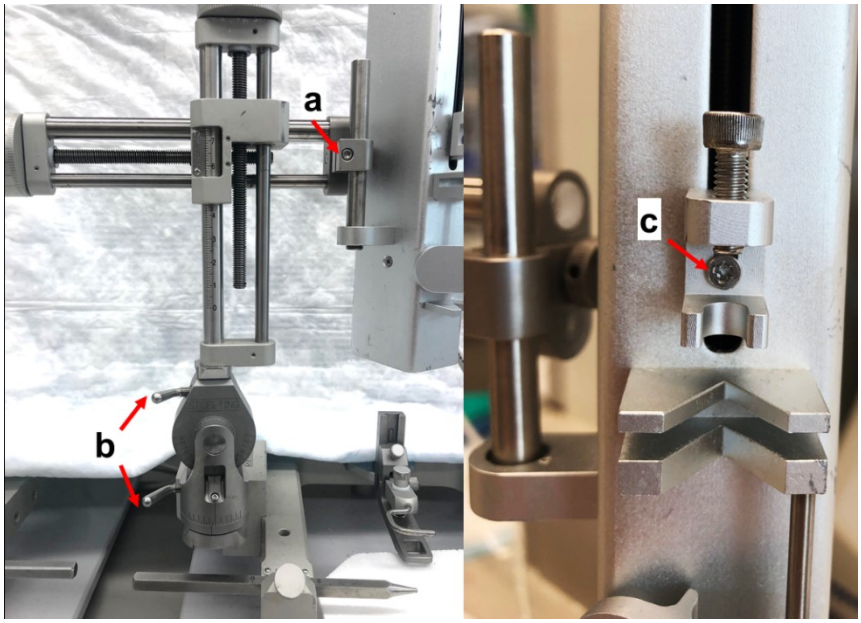

Figure 1.5: CED device arrangement. All components should be fully stabilized prior to CED experiments. Specifically, it is critical to securely fasten **(a)** the corner clamp probe holder to firmly hold the syringe header during the procedure, **(b)** the base of 3-axes manipulator arm to avoid its rotation and **(c)** the screw on the syringe header must be fastened to ensure that a syringe is tightly associated with the header during the infusion.

2.7 Determination of infusion parameters

Infusion parameters are generally perceived as important factors that dictate the final outcomes of CED. However, reports that have systemically evaluated the impacts of infusion parameters are rare. It is conceivable that increase in the infusion rate, by potentially increasing the pressure gradient, may improve the distribution of therapeutics or NPs within the brain tissue following CED. However, greater infusion rates have been shown to enhance reflux, thereby offsetting their otherwise positive impacts on the distribution (*115*). For example, it has been demonstrated that the difference in distribution of soluble proteins (i.e. bovine serum albumin; 69 kDa) in rat brains was negligible regardless of infusion rates ranging from 0.1 to 5.0 μL/min due to the greater refluxes at higher rates (*25*). However, it has been also shown that the reflux can be minimized by a careful optimization of the step distance where no significant reflux was observed up to the infusion rate of 10 μL/min when 1-mm step distance was employed (*116*). We note that infusion rates of 0.1 to 1 μL/min and 0.33 to 5 μL/min are commonly used for mice (*85, 117-119*) and rats (*38, 116, 120-122*), respectively. Based on these previously reported ranges and our in-house optimization, we infuse overall volumes of 2 and 20 μL at rates of 0.2 and 0.33 μL/min for mice and rats, respectively (*38, 72, 73*).

As described above, hypertonic infusate solution can enhance volume of NP distribution by osmotically increasing the brain ECM pore sizes (*77, 78*) when NP diffusion in the brain tissue is primarily hindered by steric hindrance imposed by the ECM mesh (e.g. BPN or PS-PEG NP) (Figure 1.6) (*38*). However, conventional NPs (e.g. PS-COOH NP) that readily interact with ECM components are unable to fully exploit this mechanism due to the contribution of adhesion on their diffusion in brain tissue (*38*). It should be also noted that the colloidal stability of NPs must be retained in a hypertonic infusate solution as the increase in NP sizes in an infusate

solution can offset the effect of infusate-mediated enlargement of the ECM pores on steric hindrance to NP diffusion (*38*).

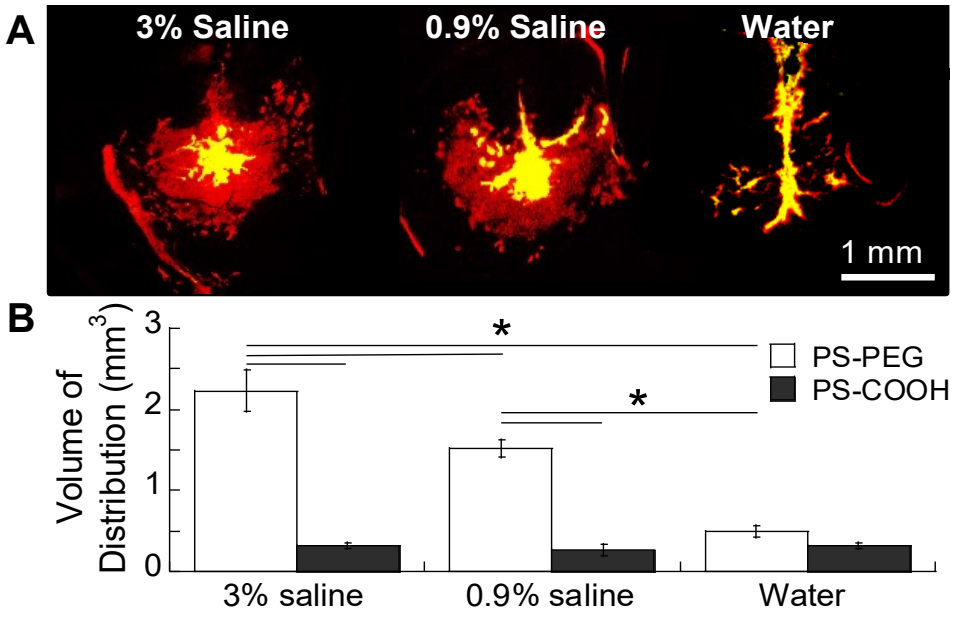

Figure 1.6: Effect of infusate osmolality on the volume of distribution of NPs in mouse brains following CED. (A) Representative tissue sections depicting the coronal plane within the mouse striatum where PS-PEG (red) and PS-COOH (green) NPs were infused via CED. Yellow fluorescence represents overlay of two different types of NPs. Scale bar = 1 mm. **(B)** Volumetric distribution of PS-PEG and PS-COOH NPs quantified by an image-based MATLAB analysis described in section 3.5. *$p <$ 0.05 denotes a statistically significant difference. *Reproduced from Zhang, C. et al. 2017 with permission from Elsevier.*

2.8 NP formulation and characterization

Model BPNs are engineered by amidation reaction between carboxyl groups on the surface of fluorescently labeled PS-COOH NPs and methoxy-PEG-NH_2, following a previously reported protocol (*123, 124*) with some modification. Briefly, PS-COOH NPs are diluted in ultrapure water to the NP concentration of 1.25% w/v (i.e. 4-fold dilution from the stock concentration), followed by an addition of methoxy-PEG-NH_2 at two-molar equivalents of the surface carboxyl groups. Subsequently, 10-molar equivalents (to methoxy-PEG-NH_2) of NHS is added to the mixture and diluted with a 200 mM borate buffer to the final NP concentration of 0.375% w/v. Finally, 1-molar equivalent (to methoxy-PEG-NH_2) of EDC is added and mixed until all reagents are fully dissolved. The particle suspension is incubated at 25°C on a rotary incubator overnight, washed

in Amicon Ultra-0.5 mL 100 K MW filters by extensive centrifugation to remove unreacted species as well as to recover the starting NPs concentration (i.e. 5% w/v) and then stored at 4 °C until use.

NPs are suspended in 10 mM NaCl for fundamental physicochemical characterization via a Zetasizer NanoZS. Specifically, hydrodynamic diameter and polydispersity index are measured by dynamic light scattering (DLS) with 90° scattering optics. The ζ-potential, an indicative of NP surface charge, is determined by laser Doppler anemometry, also known as laser Doppler velocimetry. Table 1.3 demonstrates physicochemical properties of PS-COOH and PS-PEG (i.e. BPN) NPs described above. The surface PEG density is quantified by ^{1}H NMR as previously reported (*56*). Briefly, PS-PEG NPs are fully dissolved in a mixture of deuterated chloroform and trifluoroacetic acid containing 0.5% w/v BTSB and subjected to ^{1}H NMR measurement. Total amount of PEG molecules on NP surfaces are then determined using a standard curve established with ^{1}H NMR integrals measured at various concentrations of 5 kDa methoxy-PEG-NH_2 (3.6 ppm) dissolved in the same deuterated solvent mixture. In parallel, NP surface area is estimated by the hydrodynamic diameter of NP measured by DLS and the density of PS provided by the manufacturer (i.e. 1.055 g/ml). The surface PEG density is then calculated by dividing the total amount of PEG molecules with NP surface area. The colloidal stability of NPs in a physiologically relevant brain microenvironment is assessed by incubation of NPs in artificial CSF at 37 °C, followed by DLS measurement at different time points post-incubation. Likewise, the colloidal stability of NPs in a pre-determined infusate solution over time is assessed by DLS. Fresh NPs are store at 4 °C and diluted to 1 mg/ml in an infusate solution prior to CED experiments.

Table 1.3: Physicochemical properties of PS NPs.

Particle types	Hydrodynamic diameter ± SEM (nm)[a]	Polydispersity index (PDI)[a]	ζ-potential ± SEM (mV)[b]
PS-COOH	42 ± 10	0.05	-39 ± 3
PS-PEG	69 ± 8	0.04	- 3 ± 1

[a] Hydrodynamic diameter and polydispersity index (PDI) were measured by dynamic light scattering (DLS) in 10 mM NaCl at pH 7.0. Mean ± SEM (n ≥ 3).
[b] ζ-potential was measured by laser Doppler anemometry in 10 mM NaCl at pH 7.0. Mean ± SEM (n ≥ 3).

2.9 Animal preparation and CED execution

Rodents are anesthetized by an intraperitoneal administration of ketamine and xylazine at 75 and 7.5 mg/kg, respectively. We then lubricate eyes, shave the hair on the head and sterilize the skin with an antiseptic solution. Subsequently, a midline scalp incision is made to expose the coronal and sagittal sutures of the skull and a small 1-mm burr hole is made by carefully drilling through the skull. It is critical not to damage the brain tissue (e.g. hemorrhage) during this procedure by perforating beyond the skull.

We sequentially wash the Hamilton Neuros syringe with ethanol or acetone and with ultrapure water or an infusate solution prior to the loading of the syringe with a NP-suspended infusate solution. The syringe filled with a NP suspension is then vertically mounted onto the Nanojet syringe header. Of note, the syringe is subjected to the two-step wash between consecutive injections to avoid potential NP contamination when multiple CED experiments with different NP types are involved.

We most routinely conduct CED experiments targeting the striatum where several preclinical neurological disease as well as orthotopic brain tumor models are often established (*125*), while several other anatomical locations can potentially be target sites (e.g. hippocampus for Alzheimer's disease). The syringe is lowered to a depth of 2.5 mm from the dura at the coordinate of 2 mm lateral to and 0.5 mm anterior to bregma for mice (Figure 1.7A), and to a

depth of 3.5 mm from the dura at the coordinate of 3 mm lateral to and 0.5 mm posterior to bregma for rats (Figure 1.7B) (*126*).

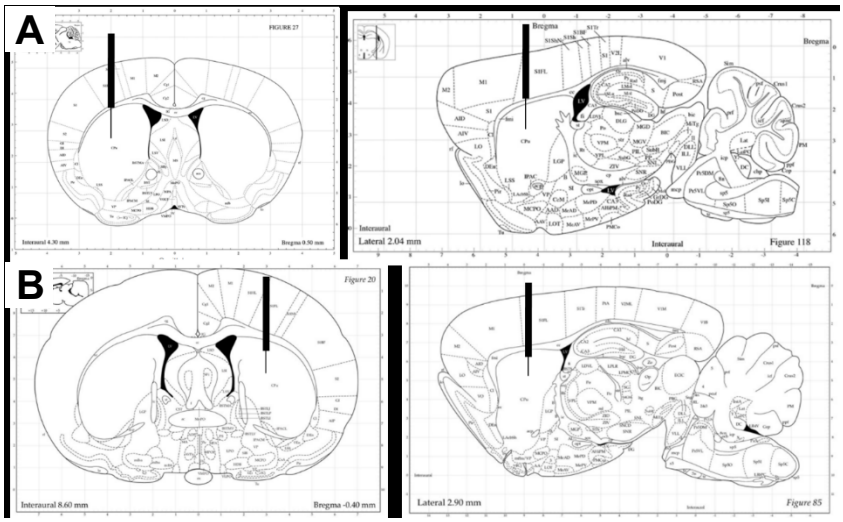

Figure 1.7: Coordinates to infusing therapeutics or NPs into rodent striatum. A stepped-down catheter with a 1-mm step distance points **(A)** a mouse coordinate of medial-lateral (ML) 2 mm, anterior-posterior (AP) 0.5 mm and dorsal-ventral (DV) 2.5 mm, and **(B)** a rat coordinate of ML 3 mm, AP -0.5 mm and DV 3.5 mm.

The pre-infusion sealing time of 5 - 10 minutes is applied after inserting the catheter into the brain in order to minimize tissue damage and to provide tissue-syringe equilibration (see Figure 1.8 for animal set-up) (*25*), and then infusion is commenced as programmed by the control box. The syringe should be withdrawn slowly (i.e. at a rate of 1 mm/min) 5 minutes after the completion of a CED experiment to minimize the reflux. Subsequently, animals are placed on a heating pad for quick recovery while the skin opening is washed with a sterile medical-grade saline and sutured with biodegradable sutures, followed by topical application of an antiseptic.

Figure 1.8: Final CED set-up with rodents mounted onto stereotaxic frames. Rats are under anesthesia and stepped-down catheters are inserted into rat brains targeting striatum (i.e. a coordinate in Figure 7B).

2.9 Tissue processing and imaging analysis

Using the model BPNs, we have confirmed the previous finding that the volume of NP distribution remains consistent from immediately up to 24 hours after the completion of CED (*41, 122*). We thus routinely harvest brain tissues immediately after the infusion and fix the tissue with 4% paraformaldehyde for 24 hours. Subsequently, the brain tissues are immersed in cryoprotective gradient sucrose solutions and then frozen at -80 °C. For the cryosection, frozen brain tissues are first equilibrated in a cryostat for more than 30 minutes at a chamber and an operating temperature of -24 and -22 °C, respectively. The brain tissues are then mounted on the tissue stage, firmly secured with the OCT compound and sectioned at ± 2 mm of the coronal infusion plate with a section thickness of 50 and 100 μm for mice and rats, respectively. Slides with tissues sections are subsequently fixed with the Dako fluorescence mounting medium and stored at 4 °C until confocal microscopy. While fixed tissue samples are generally considered amenable to a long-term storage at 4 °C (*127, 128*), it has been also reported that the autofluorescence often observed with fixed samples increases with the storage period (*129*). We thus conduct confocal microscopy of tissue sections no later than a few days of CED experiments.

We acquire 2D images of fluorescent NP distribution within the striatal tissue sections captured through the 5x/0.25 M27 air objective using a Zeiss LSM 710 confocal laser scanning microscope. We start from the tissue section of the coronal infusion plate and take images of all sections exhibiting NP fluorescence beyond background. The laser power and the master gain are carefully adjusted using the range indicator to prevent saturation of fluorescence. Other software settings, including but not limited pinhole size, scan zoom and tile numbers, are also adjusted depending on type of fluorophore, region of interest, thickness of tissue sections, etc.

It is critical to properly subtract background fluorescence to accurately quantify the NP fluorescence signal and its coverage area. We use a custom-made MATLAB script featuring a binarization algorithm named Otsu's thresholding that distinguishes the pixels with positive (i.e. foreground) fluorescence signals from those with background signals (*55*). The code then quantifies background-subtracted NP-positive area in each tissue section and the volume of NP distribution is finally calculated by multiplying the measured areas with the thickness between individual sections. Images of individual sections are stacked and aligned by Metamorph® image analysis software and StackReg plugin functionality of ImageJ, respectively. Finally, 3D-rendered volume of NP distribution is created by Imaris (Bitplane, South Windsor, CT) at 10% maximum fluorescent intensity (Figure 1.9).

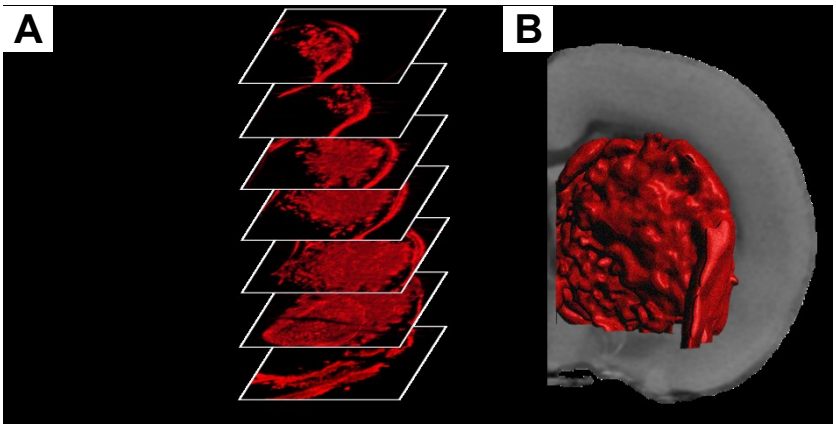

Figure 1.9: Workflow for image-based analysis of NP distribution in the brain. (A) Representative 2D images of consecutive rat brain tissue sections away from the coronal plane of infusion captured by confocal microscopy. Red fluorescence indicates model BPNs (i.e. PS-PEG NPs) administered into the rat striatum via CED. **(B)** Representative 3D-rendered volumetric distribution of BPNs created by stacking and aligning the series of 2D images. Scale bar = 1 mm.

3. Notes for troubleshooting

Cleaning of needle sleeve

Use of the stepped-down catheter without a blind stop involves insertion of the sleeve-end into the brain tissue. During the catheter insertion and subsequent CED experiments, brain tissue residues and/or blood often squeeze into the sleeve hollow, which cannot be cleared by the standard cleaning procedure described in an earlier section. We thus recommend that the

sleeve should be slid towards the syringe to expose the needle beyond the step distance and completely remove the remnant biological specimen by alcohol swipe. It should be noted that residual tissues and/or blood clots can potentially contaminate brain tissues of rodents undergoing future CED experiments.

Removal of air bubbles

The syringe plunger should be pulled up slowly to minimize the aspiration of air into the syringe during the sample loading. Nevertheless, we occasionally encounter air bubble accumulation within needle and/or syringe, which often promotes pressure spikes and reflux during the CED experiments, thereby leading to suboptimal distribution of therapeutics or NPs in the brain (*7, 130*). We also note that air bubbles in the infusate solution would be included in a preset volume of infusion and thus a fraction of sample would be left within the syringe without being administered (i.e. infusion of a lower dose than planned). We thus recommend that the syringe is loaded with an excess of sample volume and purged at a high infusion rate (i.e. no greater than 16.7 μL/min) for a few minutes to remove air bubbles prior to the catheter insertion into the rodent brain (*39, 131*).

4. Conclusions

In this chapter, we have introduced a marriage of CED and BPN as an attractive strategy to achieve widespread distribution of therapeutic or diagnostic payloads in the brain following local administration. We have walked through rationales, materials, methods and a few troubleshooting remarks based on our expertise and experience as well as findings from relevant studies reported by excellent scientists and clinicians devoted to the field. The consolidated efforts have led to multiple clinical trials as described earlier and the safety of CED procedure is now well established in humans. However, later stage trials have revealed technical shortcomings that need to be addressed to fulfil its therapeutic potential, which include design and refinement of CED compartments and parameters (*21*). In addition, combined

approach of CED and NP-based delivery systems, including BPNs, is yet at its infancy with most of the studies at their preclinical stages. Encouragingly, the field has recently experienced expansion regarding simultaneous optimization of CED procedure and NP engineering, and lessons learned will pave a way for its clinical development.

5. References

1. S. Wohlfart, S. Gelperina, J. Kreuter, Transport of drugs across the blood-brain barrier by nanoparticles. *J Control Release* **161**, 264-273 (2012).
2. R. A. Kroll, E. A. Neuwelt, Outwitting the blood-brain barrier for therapeutic purposes: osmotic opening and other means. *Neurosurgery* **42**, 1083-1099; discussion 1099-1100 (1998).
3. N. Vykhodtseva, N. McDannold, K. Hynynen, Progress and problems in the application of focused ultrasound for blood-brain barrier disruption. *Ultrasonics* **48**, 279-296 (2008).
4. J. E. Kennedy, High-intensity focused ultrasound in the treatment of solid tumours. *Nat Rev Cancer* **5**, 321-327 (2005).
5. C. T. Curley, N. D. Sheybani, T. N. Bullock, R. J. Price, Focused Ultrasound Immunotherapy for Central Nervous System Pathologies: Challenges and Opportunities. *Theranostics* **7**, 3608-3623 (2017).
6. T. Patel, J. Zhou, J. M. Piepmeier, W. M. Saltzman, Polymeric nanoparticles for drug delivery to the central nervous system. *Adv Drug Deliv Rev* **64**, 701-705 (2012).
7. A. M. Mehta, A. M. Sonabend, J. N. Bruce, Convection-Enhanced Delivery. *Neurotherapeutics* **14**, 358-371 (2017).
8. P. Calias, W. A. Banks, D. Begley, M. Scarpa, P. Dickson, Intrathecal delivery of protein therapeutics to the brain: a critical reassessment. *Pharmacol Ther* **144**, 114-122 (2014).
9. M. Hammarlund-Udenaes, M. Friden, S. Syvanen, A. Gupta, On the rate and extent of drug delivery to the brain. *Pharm Res* **25**, 1737-1750 (2008).

10. W. M. Pardridge, Drug transport across the blood-brain barrier. *J Cereb Blood Flow Metab* **32**, 1959-1972 (2012).

11. R. K. Jain, Delivery of Novel Therapeutic Agents in Tumors: Physiological Barriers and Strategies. *JNCI: Journal of the National Cancer Institute* **81**, 570-576 (1989).

12. W. H. Oldendorf, Cerebrospinal fluid formation and circulation. *Prog Nucl Med* **1**, 336-358 (1972).

13. R. W. Cutler, L. Page, J. Galicich, G. V. Watters, Formation and absorption of cerebrospinal fluid in man. *Brain* **91**, 707-720 (1968).

14. Q. Yan *et al.*, Distribution of intracerebral ventricularly administered neurotrophins in rat brain and its correlation with trk receptor expression. *Exp Neurol* **127**, 23-36 (1994).

15. L. K. Fung *et al.*, Pharmacokinetics of interstitial delivery of carmustine, 4-hydroperoxycyclophosphamide, and paclitaxel from a biodegradable polymer implant in the monkey brain. *Cancer Res* **58**, 672-684 (1998).

16. D. J. Wolak, R. G. Thorne, Diffusion of macromolecules in the brain: implications for drug delivery. *Mol Pharm* **10**, 1492-1504 (2013).

17. L. K. Fung, M. Shin, B. Tyler, H. Brem, W. M. Saltzman, Chemotherapeutic Drugs Released from Polymers: Distribution of 1,3-bis(2-chloroethyl)-l-nitrosourea in the Rat Brain. *Pharmaceutical Research* **13**, 671-682 (1996).

18. R. H. Bobo *et al.*, Convection-enhanced delivery of macromolecules in the brain. *Proc Natl Acad Sci U S A* **91**, 2076-2080 (1994).

19. J. N. Bruce *et al.*, Regression of recurrent malignant gliomas with convection-enhanced delivery of topotecan. *Neurosurgery* **69**, 1272-1279; discussion 1279-1280 (2011).

20. J. W. Degen, S. Walbridge, A. O. Vortmeyer, E. H. Oldfield, R. R. Lonser, Safety and efficacy of convection-enhanced delivery of gemcitabine or carboplatin in a malignant glioma model in rats. *J Neurosurg* **99**, 893-898 (2003).

21. A. Jahangiri *et al.*, Convection-enhanced delivery in glioblastoma: a review of preclinical and clinical studies. *J Neurosurg* **126**, 191-200 (2017).

22. D. M. Lieberman, D. W. Laske, P. F. Morrison, K. S. Bankiewicz, E. H. Oldfield, Convection-enhanced distribution of large molecules in gray matter during interstitial drug infusion. *J Neurosurg* **82**, 1021-1029 (1995).

23. R. Raghavan *et al.*, Convection-enhanced delivery of therapeutics for brain disease, and its optimization. *Neurosurg Focus* **20**, E12 (2006).

24. Z. Zhou, R. Singh, M. M. Souweidane, Convection-Enhanced Delivery for Diffuse Intrinsic Pontine Glioma Treatment. *Curr Neuropharmacol* **15**, 116-128 (2017).

25. Michael Y. Chen, Russell R. Lonser, Paul F. Morrison, Lance S. Governale, Edward H. Oldfield, Variables affecting convection-enhanced delivery to the striatum: a systematic examination of rate of infusion, cannula size, infusate concentration, and tissue—cannula sealing time. *Journal of Neurosurgery* **90**, 315-320 (1999).

26. K. Kawakami, M. Kawakami, M. Kioi, S. R. Husain, R. K. Puri, Distribution of bolus or convection-enhanced delivery of IL-13 receptor-directed cytotoxin to intracranial brain tumors in a mouse model. *Cancer Research* **64**, 1246-1247 (2004).

27. R. R. Lonser, M. Sarntinoranont, P. F. Morrison, E. H. Oldfield, Convection-enhanced delivery to the central nervous system. *J Neurosurg* **122**, 697-706 (2015).

28. M. A. Vogelbaum, M. K. Aghi, Convection-enhanced delivery for the treatment of glioblastoma. *Neuro Oncol* **17 Suppl 2**, ii3-ii8 (2015).

29. T. H. Ung, H. Malone, P. Canoll, J. N. Bruce, Convection-enhanced delivery for glioblastoma: targeted delivery of antitumor therapeutics. *CNS Oncol* **4**, 225-234 (2015).

30. R. C. Anderson *et al.*, Convection-enhanced delivery of topotecan into diffuse intrinsic brainstem tumors in children. *Journal of neurosurgery. Pediatrics* **11**, 289-295 (2013).

31. F. G. Barker, 2nd *et al.*, Survival and functional status after resection of recurrent glioblastoma multiforme. *Neurosurgery* **42**, 709-720; discussion 720-703 (1998).

32. G. S. Miranpuri *et al.*, Gene-based therapy of Parkinson's Disease: Translation from animal model to human clinical trial employing convection enhanced delivery. *Ann Neurosci* **19**, 133-146 (2012).

33. D. K. Song, R. R. Lonser, Convection-enhanced delivery for the treatment of pediatric neurologic disorders. *J Child Neurol* **23**, 1231-1237 (2008).

34. R. R. Lonser *et al.*, Real-time image-guided direct convective perfusion of intrinsic brainstem lesions. Technical note. *J Neurosurg* **107**, 190-197 (2007).

35. W. Martin Bauknight *et al.*, Convection enhanced drug delivery of BDNF through a microcannula in a rodent model to strengthen connectivity of a peripheral motor nerve bridge model to bypass spinal cord injury. *J Clin Neurosci* **19**, 563-569 (2012).

36. M. A. Rogawski, Convection-enhanced delivery in the treatment of epilepsy. *Neurotherapeutics* **6**, 344-351 (2009).

37. P. J. Haar *et al.*, Quantification of convection-enhanced delivery to the ischemic brain. *Physiol Meas* **31**, 1075-1089 (2010).

38. C. Zhang *et al.*, Strategies to enhance the distribution of nanotherapeutics in the brain. *J Control Release* **267**, 232-239 (2017).

39. E. Allard, C. Passirani, J. P. Benoit, Convection-enhanced delivery of nanocarriers for the treatment of brain tumors. *Biomaterials* **30**, 2302-2318 (2009).

40. P. F. Morrison, D. W. Laske, H. Bobo, E. H. Oldfield, R. L. Dedrick, High-flow microinfusion: tissue penetration and pharmacodynamics. *Am J Physiol* **266**, R292-305 (1994).

41. R. Singh *et al.*, Volume of distribution and clearance of peptide-based nanofiber after convection-enhanced delivery. *J Neurosurg*, 1-9 (2017).

42. A. R. Asthagiri, S. Walbridge, J. D. Heiss, R. R. Lonser, Effect of concentration on the accuracy of convective imaging distribution of a gadolinium-based surrogate tracer. *J Neurosurg* **115**, 467-473 (2011).

43. J. Blakeley, Drug delivery to brain tumors. *Curr Neurol Neurosci Rep* **8**, 235-241 (2008).

44. C. H. Heldin, K. Rubin, K. Pietras, A. Ostman, High interstitial fluid pressure - an obstacle in cancer therapy. *Nat Rev Cancer* **4**, 806-813 (2004).

45. C. S. Teo, W. Hor Keong Tan, T. Lee, C.-H. Wang, Transient interstitial fluid flow in brain tumors: Effect on drug delivery. *Chemical Engineering Science* **60**, 4803-4821 (2005).

46. N. U. Barua *et al.*, A novel implantable catheter system with transcutaneous port for intermittent convection-enhanced delivery of carboplatin for recurrent glioblastoma. *Drug Deliv* **23**, 167-173 (2016).

47. A. Boiardi *et al.*, Treatment of recurrent glioblastoma: can local delivery of mitoxantrone improve survival? *J Neurooncol* **88**, 105-113 (2008).

48. K. A. Lopez *et al.*, Convection-enhanced delivery of topotecan into a PDGF-driven model of glioblastoma prolongs survival and ablates both tumor-initiating cells and recruited glial progenitors. *Cancer Res* **71**, 3963-3971 (2011).

49. R. A. Patchell *et al.*, A phase I trial of continuously infused intratumoral bleomycin for the treatment of recurrent glioblastoma multiforme. *J Neurooncol* **60**, 37-42 (2002).

50. A. M. Sonabend *et al.*, Prolonged intracerebral convection-enhanced delivery of topotecan with a subcutaneously implantable infusion pump. *Neuro Oncol* **13**, 886-893 (2011).

51. A. Bienemann *et al.*, The development of an implantable catheter system for chronic or intermittent convection-enhanced delivery. *J Neurosci Methods* **203**, 284-291 (2012).

52. S. Gelperina, K. Kisich, M. D. Iseman, L. Heifets, The potential advantages of nanoparticle drug delivery systems in chemotherapy of tuberculosis. *Am J Respir Crit Care Med* **172**, 1487-1490 (2005).

53. S. R. Mudshinge, A. B. Deore, S. Patil, C. M. Bhalgat, Nanoparticles: Emerging carriers for drug delivery. *Saudi Pharm J* **19**, 129-141 (2011).

54. Y. E. Seo, T. Bu, W. M. Saltzman, Nanomaterials for convection-enhanced delivery of agents to treat brain tumors. *Curr Opin Biomed Eng* **4**, 1-12 (2017).

55. E. Song *et al.*, Surface chemistry governs cellular tropism of nanoparticles in the brain. *Nat Commun* **8**, 15322 (2017).

56. E. A. Nance *et al.*, A dense poly(ethylene glycol) coating improves penetration of large polymeric nanoparticles within brain tissue. *Sci Transl Med* **4**, 149ra119 (2012).

57. E. Sykova, C. Nicholson, Diffusion in brain extracellular space. *Physiological reviews* **88**, 1277-1340 (2008).

58. D. R. Zimmermann, M. T. Dours-Zimmermann, Extracellular matrix of the central nervous system: from neglect to challenge. *Histochemistry and cell biology* **130**, 635-653 (2008).

59. N. George, H. M. Geller, Extracellular matrix and traumatic brain injury. *J Neurosci Res* **96**, 573-588 (2018).

60. C. Frantz, K. M. Stewart, V. M. Weaver, The extracellular matrix at a glance. *Journal of Cell Science* **123**, 4195-4200 (2010).

61. J. S. Suk, Q. Xu, N. Kim, J. Hanes, L. M. Ensign, PEGylation as a strategy for improving nanoparticle-based drug and gene delivery. *Adv Drug Deliv Rev* **99**, 28-51 (2016).

62. R. G. Thorne, C. Nicholson, In vivo diffusion analysis with quantum dots and dextrans predicts the width of brain extracellular space. *Proc Natl Acad Sci U S A* **103**, 5567-5572 (2006).

63. E. Nance *et al.*, Brain-penetrating nanoparticles improve paclitaxel efficacy in malignant glioma following local administration. *ACS Nano* **8**, 10655-10664 (2014).

64. Q. Xu *et al.*, Impact of Surface Polyethylene Glycol (PEG) Density on Biodegradable Nanoparticle Transport in Mucus ex Vivo and Distribution in Vivo. *ACS Nano* **9**, 9217-9227 (2015).

65. P. Mastorakos *et al.*, Biodegradable brain-penetrating DNA nanocomplexes and their use to treat malignant brain tumors. *J Control Release* **262**, 37-46 (2017).

66. B. Cragg, Preservation of extracellular space during fixation of the brain for electron microscopy. *Tissue and Cell* **12**, 63-72 (1980).

67. V. P. Ferrer, V. Moura Neto, R. Mentlein, Glioma infiltration and extracellular matrix: key players and modulators. *Glia*, (2018).

68. U. Naumann *et al.*, Glioma cell migration and invasion as potential target for novel treatment strategies. *Translational Neuroscience* **4**, 314-329 (2013).

69. L. P. Serwer, C. D. James, Challenges in drug delivery to tumors of the central nervous system: an overview of pharmacological and surgical considerations. *Adv Drug Deliv Rev* **64**, 590-597 (2012).

70. S. Berry *et al.*, Enhancing Intracranial Delivery of Clinically Relevant Non-viral Gene Vectors. *RSC Adv* **48**, 41665-41674 (2016).

71. P. Mastorakos *et al.*, Highly PEGylated DNA Nanoparticles Provide Uniform and Widespread Gene Transfer in the Brain. *Adv Healthc Mater* **4**, 1023-1033 (2015).

72. P. Mastorakos *et al.*, Biodegradable DNA Nanoparticles that Provide Widespread Gene Delivery in the Brain. *Small* **12**, 678-685 (2016).

73. C. S. Schneider *et al.*, Minimizing the non-specific binding of nanoparticles to the brain enables active targeting of Fn14-positive glioblastoma cells. *Biomaterials* **42**, 42-51 (2015).

74. C. Zhang *et al.*, Convection enhanced delivery of cisplatin-loaded brain penetrating nanoparticles cures malignant glioma in rats. *J Control Release* **263**, 112-119 (2017).

75. S. Salmaso, P. Caliceti, Stealth properties to improve therapeutic efficacy of drug nanocarriers. *J Drug Deliv* **2013**, 374252 (2013).

76. G. D. Mogosanu, A. M. Grumezescu, C. Bejenaru, L. E. Bejenaru, Polymeric protective agents for nanoparticles in drug delivery and targeting. *Int J Pharm* **510**, 419-429 (2016).

77. J. Kume-Kick *et al.*, Independence of extracellular tortuosity and volume fraction during osmotic challenge in rat neocortex. *J Physiol* **542**, 515-527 (2002).

78. K. C. Chen, C. Nicholson, Changes in brain cell shape create residual extracellular space volume and explain tortuosity behavior during osmotic challenge. *Proc Natl Acad Sci U S A* **97**, 8306-8311 (2000).

79. D. S. Hersh *et al.*, MR-guided transcranial focused ultrasound safely enhances interstitial dispersion of large polymeric nanoparticles in the living brain. *PLoS One* **13**, e0192240 (2018).

80. C. W. Christine *et al.*, Safety and tolerability of putaminal AADC gene therapy for Parkinson disease. *Neurology* **73**, 1662-1669 (2009).

81. M. S. Fiandaca *et al.*, Real-time MR imaging of adeno-associated viral vector delivery to the primate brain. *NeuroImage* **47 Suppl 2**, T27-35 (2009).

82. N. W. Barton *et al.*, Replacement therapy for inherited enzyme deficiency--macrophage-targeted glucocerebrosidase for Gaucher's disease. *The New England journal of medicine* **324**, 1464-1470 (1991).

83. J. Voges *et al.*, Imaging-guided convection-enhanced delivery and gene therapy of glioblastoma. *Ann Neurol* **54**, 479-487 (2003).

84. H. Ren *et al.*, Immunogene therapy of recurrent glioblastoma multiforme with a liposomally encapsulated replication-incompetent Semliki forest virus vector carrying the human interleukin-12 gene--a phase I/II clinical protocol. *J Neurooncol* **64**, 147-154 (2003).

85. P. Y. Chen *et al.*, Comparing routes of delivery for nanoliposomal irinotecan shows superior anti-tumor activity of local administration in treating intracranial glioblastoma xenografts. *Neuro Oncol* **15**, 189-197 (2013).

86. N. Butowski *et al.*, A PHASE I STUDY OF CONVECTION-ENHANCED DELIVERY OF LIPOSOMAL-IRINOTECAN USING REAL-TIME IMAGING WITH GADOLINIUM IN PATIENTS WITH RECURRENT HIGH GRADE GLIOMA. *Neuro Oncol* **16**, iii13 (2014).

87. E. White *et al.*, A phase I trial of carboplatin administered by convection-enhanced delivery to patients with recurrent/progressive glioblastoma multiforme. *Contemporary clinical trials* **33**, 320-331 (2012).

88. S. J. Patel *et al.*, Safety and feasibility of convection-enhanced delivery of Cotara for the treatment of malignant glioma: initial experience in 51 patients. *Neurosurgery* **56**, 1243-1252; discussion 1252-1243 (2005).

89. A. Carpentier *et al.*, Intracerebral administration of CpG oligonucleotide for patients with recurrent glioblastoma: a phase II study. *Neuro Oncol* **12**, 401-408 (2010).

90. A. Carpentier *et al.*, Phase 1 trial of a CpG oligodeoxynucleotide for patients with recurrent glioblastoma. *Neuro Oncol* **8**, 60-66 (2006).

91. D. Randazzo *et al.*, Phase 1 single-center, dose escalation study of D2C7-IT administered intratumorally via convection-enhanced delivery for adult patients with recurrent malignant glioma. *Journal of Clinical Oncology* **35**, e13532-e13532 (2017).

92. K. V. Keu *et al.*, Reporter gene imaging of targeted T cell immunotherapy in recurrent glioma. *Sci Transl Med* **9**, (2017).

93. S. Kunwar, Convection enhanced delivery of IL13-PE38QQR for treatment of recurrent malignant glioma: presentation of interim findings from ongoing phase 1 studies. *Acta neurochirurgica. Supplement* **88**, 105-111 (2003).

94. S. Kunwar *et al.*, Direct intracerebral delivery of cintredekin besudotox (IL13-PE38QQR) in recurrent malignant glioma: a report by the Cintredekin Besudotox Intraparenchymal Study Group. *Journal of clinical oncology : official journal of the American Society of Clinical Oncology* **25**, 837-844 (2007).

95. S. Kunwar *et al.*, Phase III randomized trial of CED of IL13-PE38QQR vs Gliadel wafers for recurrent glioblastoma. *Neuro Oncol* **12**, 871-881 (2010).

96. S. Mueller *et al.*, Effect of imaging and catheter characteristics on clinical outcome for patients in the PRECISE study. *J Neurooncol* **101**, 267-277 (2011).

97. P. Chittiboina, J. D. Heiss, K. E. Warren, R. R. Lonser, Magnetic resonance imaging properties of convective delivery in diffuse intrinsic pontine gliomas. *Journal of neurosurgery. Pediatrics* **13**, 276-282 (2014).

98. M. A. Vogelbaum *et al.*, Convection-enhanced delivery of cintredekin besudotox (interleukin-13-PE38QQR) followed by radiation therapy with and without temozolomide in newly diagnosed malignant gliomas: phase 1 study of final safety results. *Neurosurgery* **61**, 1031-1037; discussion 1037-1038 (2007).

99. P. Wersall *et al.*, Intratumoral infusion of the monoclonal antibody, mAb 425, against the epidermal-growth-factor receptor in patients with advanced malignant glioma. *Cancer immunology, immunotherapy : CII* **44**, 157-164 (1997).

100. F. W. Weber *et al.*, Local convection enhanced delivery of IL4-Pseudomonas exotoxin (NBI-3001) for treatment of patients with recurrent malignant glioma. *Acta neurochirurgica. Supplement* **88**, 93-103 (2003).

101. R. Saito *et al.*, Regression of recurrent glioblastoma infiltrating the brainstem after convection-enhanced delivery of nimustine hydrochloride. *Journal of neurosurgery. Pediatrics* **7**, 522-526 (2011).

102. Z. Lidar *et al.*, Convection-enhanced delivery of paclitaxel for the treatment of recurrent malignant glioma: a phase I/II clinical study. *J Neurosurg* **100**, 472-479 (2004).

103. Y. Mardor *et al.*, Monitoring response to convection-enhanced taxol delivery in brain tumor patients using diffusion-weighted magnetic resonance imaging. *Cancer Res* **61**, 4971-4973 (2001).

104. A. Desjardins *et al.*, ONCOLYTIC POLIO/RHINOVIRUS RECOMBINANT (PVSRIPO) IN RECURRENT GLIOBLASTOMA (GBM): FIRST PHASE I CLINICAL TRIAL EVALUATING THE INTRATUMORAL ADMINISTRATION. *Neuro-Oncology* **16**, iii43-iii43 (2014).

105. D. W. Laske, R. J. Youle, E. H. Oldfield, Tumor regression with regional distribution of the targeted toxin TF-CRM107 in patients with malignant brain tumors. *Nature medicine* **3**, 1362-1368 (1997).

106. M. Weaver, D. W. Laske, Transferrin receptor ligand-targeted toxin conjugate (Tf-CRM107) for therapy of malignant gliomas. *J Neurooncol* **65**, 3-13 (2003).

107. M. Vogelbaum, A. Mohammadi, C. Brewer, D. M. Peereboom, M. Ahluwalia, SURG-10. CONVECTION ENHANCED DELIVERY OF TOPOTECAN AND GADOLINIUM FOR RECURRENT GBM VIA THE CLEVELAND MULTIPORT CATHETER: A FIRST IN HUMAN STUDY. *Neuro-Oncology* **19**, vi237-vi237 (2017).

108. J. H. Sampson *et al.*, Intracerebral infusion of an EGFR-targeted toxin in recurrent malignant brain tumors. *Neuro Oncol* **10**, 320-329 (2008).

109. U. Bogdahn *et al.*, Targeted therapy for high-grade glioma with the TGF-beta2 inhibitor trabedersen: results of a randomized and controlled phase IIb study. *Neuro Oncol* **13**, 132-142 (2011).

110. H. Company.

111. W. Debinski, S. B. Tatter, Convection-enhanced delivery for the treatment of brain tumors. *Expert Rev Neurother* **9**, 1519-1527 (2009).

112. D. Yin, J. Forsayeth, K. S. Bankiewicz, Optimized cannula design and placement for convection-enhanced delivery in rat striatum. *J Neurosci Methods* **187**, 46-51 (2010).

113. Y. Liu *et al.*, Strain-based genetic differences regulate the efficiency of systemic gene delivery as well as expression. *J Biol Chem* **277**, 4966-4972 (2002).

114. V. R. Recinos *et al.*, Combination of intracranial temozolomide with intracranial carmustine improves survival when compared with either treatment alone in a rodent glioma model. *Neurosurgery* **66**, 530-537; discussion 537 (2010).

115. O. Lewis *et al.*, Chronic, intermittent convection-enhanced delivery devices. *J Neurosci Methods* **259**, 47-56 (2016).

116. M. T. Krauze *et al.*, Reflux-free cannula for convection-enhanced high-speed delivery of therapeutic agents. *J Neurosurg* **103**, 923-929 (2005).

117. M. Wang *et al.*, A Murine Model for Quantitative, Real-Time Evaluation of Convection-Enhanced Delivery (RT-CED) Using an (18)[F]-Positron Emitting, Fluorescent Derivative of Dasatinib. *Mol Cancer Ther* **16**, 2902-2912 (2017).

118. D. Sehedic *et al.*, Locoregional Confinement and Major Clinical Benefit of (188)Re-Loaded CXCR4-Targeted Nanocarriers in an Orthotopic Human to Mouse Model of Glioblastoma. *Theranostics* **7**, 4517-4536 (2017).

119. C. Y. Lin, R. J. Li, C. Y. Huang, K. C. Wei, P. Y. Chen, Controlled release of liposome-encapsulated temozolomide for brain tumour treatment by convection-enhanced delivery. *J Drug Target* **26**, 325-332 (2018).

120. W. G. B. Singleton *et al.*, The distribution, clearance, and brainstem toxicity of panobinostat administered by convection-enhanced delivery. *Journal of neurosurgery. Pediatrics*, 1-9 (2018).

121. M. M. Nordling-David *et al.*, Liposomal temozolomide drug delivery using convection enhanced delivery. *J Control Release* **261**, 138-146 (2017).

122. W. G. Singleton *et al.*, Convection enhanced delivery of panobinostat (LBH589)-loaded pluronic nano-micelles prolongs survival in the F98 rat glioma model. *Int J Nanomedicine* **12**, 1385-1399 (2017).

123. S. K. Lai *et al.*, Rapid transport of large polymeric nanoparticles in fresh undiluted human mucus. *Proc Natl Acad Sci U S A* **104**, 1482-1487 (2007).

124. S. R. Popielarski, S. H. Pun, M. E. Davis, A nanoparticle-based model delivery system to guide the rational design of gene delivery to the liver. 1. Synthesis and characterization. *Bioconjug Chem* **16**, 1063-1070 (2005).

125. P. C. Huszthy *et al.*, In vivo models of primary brain tumors: pitfalls and perspectives. *Neuro Oncol* **14**, 979-993 (2012).

126. G. Paxinos, and Charles Watson. (Elsevier, 2001-2006), vol. 2018.

127. F. Grillo *et al.*, Factors affecting immunoreactivity in long-term storage of formalin-fixed paraffin-embedded tissue sections. *Histochemistry and cell biology* **144**, 93-99 (2015).

128. Y. Ono *et al.*, Quality assessment of long-term stored formalin-fixed paraffin embedded tissues for histopathological evaluation. *J Toxicol Pathol* **31**, 61-64 (2018).

129. A. S. Davis *et al.*, Characterizing and Diminishing Autofluorescence in Formalin-fixed Paraffin-embedded Human Respiratory Tissue. *J Histochem Cytochem* **62**, 405-423 (2014).

130. F. Casanova, P. R. Carney, M. Sarntinoranont, Effect of needle insertion speed on tissue injury, stress, and backflow distribution for convection-enhanced delivery in the rat brain. *PLoS One* **9**, e94919 (2014).

131. K. A. Sillay, S. G. McClatchy, B. A. Shepherd, G. T. Venable, T. S. Fuehrer, Image-guided convection-enhanced delivery into agarose gel models of the brain. *J Vis Exp*, (2014).

Chapter 2

Widespread gene transfer to brain tumors via synthetic polymer-based DNA nanoparticles

Abstract

Gene therapy of malignant gliomas has shown a lack of clinical success to date due in part to inability of conventional gene vectors to achieve widespread gene transfer throughout highly disseminated tumor areas within the brain. Here, we demonstrate that newly engineered polymer-based DNA-loaded nanoparticles (DNA-NP) possessing small particle diameters (~50 nm) and non-adhesive surface polyethylene glycol (PEG) coatings efficiently penetrate brain tumor tissue as well as healthy brain parenchyma. Specifically, this brain-penetrating nanoparticle (BPN), following intracranial administration via convection enhanced delivery (CED), provides widespread transgene expression in heathy rodent striatum and an aggressive brain tumor tissue established orthotopically in rats. The ability of BPN to efficiently traverse both tissues is of great importance as the highly invasive glioma cells infiltrated into normal brain tissue are responsible for tumor recurrence. Of note, the transgene expression within the orthotopic tumor tissue occurred preferentially in glioma cells over microglial cells. We also show that three-dimensional (3D) multicellular spheroids established with malignant glioma cells, unlike conventional two-dimensional (2D) cell cultures, serve as an excellent *in vitro* model reliably predicting gene vector behaviors *in vivo*. Briefly, DNA-NP possessing greater surface PEG coverage exhibited more uniform and higher-level transgene expression both in the 3D model and *in vivo*, whereas the trend was opposite in 2D culture. The finding here alerts that gene transfer studies based primarily on 2D cultures should be interpreted with caution and underscores the relevance of 3D models for screening newly engineered gene vectors prior to their *in vivo* evaluation.

1. Introduction

Despite the most advanced multimodal therapeutic regimen, median survival of malignant gliomas remains ~ 14 months (*1*). Gene therapy potentially provides an alternative means to achieve more specific and powerful as well as longer-lasting therapeutic benefits. However, its clinical relevance is yet to be addressed due in large part to suboptimal gene transfer efficacy. Given the highly aggressive, invasive and infiltrative nature of malignant gliomas, inability of conventional gene vectors to provide a widespread therapeutic transgene expression is an utmost challenge (*2-4*). We have previously determined the brain extracellular matrix (ECM) to be a critical adhesive (i.e. hydrophobic and negatively charged) and steric diffusional barrier, and established design criteria for engineering nanoparticle-based therapeutic delivery systems that can efficiently spread through the ECM (*5-7*). Specifically, we found that nanoparticles with diameters small enough (≤ ~110 nm) to fit through the ECM pores while possessing non-adhesive dense surface polyethylene glycol (PEG) coatings rapidly penetrated rodent and human brain tissues (*5, 8-10*).

While being well-characterized for outstanding efficacies as a polymeric gene delivery platform, widespread use of polyethylenimine (PEI) is largely discouraged by its safety concern (*11, 12*). However, we note that PEI toxicity is often overstated based on *in vitro* studies where conventional cytotoxicity is measured with only one or two cell types at very high doses that would unlikely be translatable *in vivo*. In reality, PEI remains one of those few polymer-based platforms most widely explored in clinic (*13, 14*), including an ongoing phase II trial (NCT02806687), with a proven favorable safety profile (NCT01274455) (*15*). Further, PEI has been commonly derivatized with PEG to improve its pharmacokinetic behaviors and/or safety profiles as a gene delivery system (*9, 16-19*). To this end, we have recently demonstrated that DNA-loaded nanoparticles (DNA-NP) formulated with an inclusion of densely PEGylated PEI (PEG-PEI) provide widespread transgene expression in healthy rat brain while exhibiting good *in vivo* safety profiles, namely brain-penetrating nanoparticles (BPN) (*9, 19*). However, the

finding does not readily ensure their ability to penetrate brain tumor tissues, given that the barrier properties of tumor ECM are unlikely analogous to those of normal ECM due to significant pathological changes in cellularity and macromolecular compositions in tumors (*20*). In this study, we thus sought to engineer and evaluate PEI-based DNA-NP possessing a broader range of surface PEG contents to identify a lead system providing widespread transgene expression in brain tumor *in vivo*.

Most of the studies developing gene vectors for cancer therapy employ routine sequential experimental steps of screening newly designed systems using two-dimensional (2D) cell cultures (*21-23*), followed by *in vivo* evaluation. However, conventional 2D cultures are limited in recapitulating the highly complex and heterogeneous nature of tumors established in living organisms, including humans (*24, 25*). Indeed, virtually no correlation has been observed between performances of gene vectors in 2D cultures versus in animals in a recent study (*26*). Alternatively, three-dimensional (3D) models of multicellular tumor spheroids mimic several features found in tumors *in vivo*, including but not limited to dense ECM formation (*27, 28*) and induction of hypoxia and necrosis (*29, 30*), thereby providing a reliable surrogate for screening gene vectors, particularly in terms of predicting their *in vivo* behaviors (*31*). Thus, we here evaluate and compare performances of newly designed PEI-based DNA-NP in a 3D spheroid model as well as in an orthotopically-established rat glioma.

2. Materials and methods

2.1 DNA-NP formulation and characterization

2.1.1 Polymer preparation

Methoxy PEG N-hydroxysuccinimide (mPEG-NHS, 5 kDa, Sigma-Aldrich, St. Louis, MO) was conjugated to 25 kDa branched PEI (Sigma-Aldrich) to yield PEG-PEI copolymers, as previously described (*9, 16*). Briefly, PEI was dissolved in ultrapure distilled water, pH was adjusted to 7.5–8.0 and then mPEG-NHS was added to the PEI solution at various molar ratios,

followed by an overnight reaction at 4 °C under a constant mixing condition. The resultant polymer solution was dialyzed extensively against ultrapure distilled water for 3 days at a molecular weight cut-off (MWCO) of 50,000 kDa (Spectrum Laboratories, Inc., Rancho Dominguez, CA) and subsequently lyophilized. Nuclear magnetic resonance (NMR) analysis was conducted to confirm PEG to PEI molar ratios of 8, 30, 50, 60, and 85. 1H NMR (500 MHz, D_2O): δ 2.48-3.20 (br, CH_2CH_2NH), 3.62-3.72 (br, CH_2CH_2O). The lyophilized polymers were dissolved in ultrapure distilled water with a pH adjustment to ~6.5 - 7 at 30 mg/ml and stored at 4 °C until use.

2.1.2 DNA-NP formulation

The luciferase-expressing plasmids driven by the short-acting cytomegalovirus (CMV) promoter (i.e. pd1GL3-RL) was a kind gift from Professor Alexander M. Klibanov (M.I.T). The ZsGreen- and green-fluorescent protein (GFP)-expressing plasmids driven by the CMV promoter were purchased from Clontech Laboratories Inc. (Mountainview, CA). The luciferase- and mCherry-expressing plasmids driven by human β-actin promoter (i.e. pBAL and pBACH, respectively) were produced and provided by Copernicus Therapeutics (Cleveland, OH). Plasmids were propagated and purified, as previously described (*16, 32*). Briefly, plasmids were transformed into *E. coli* DH5α competent bacterial cells using a heat shock method, and following the bacterial expansion in LB media, plasmids were purified using EndoFree Plasmid Giga Kit (QIAGEN, Valencia, CA), as per manufacturer's protocol. Mirus Label IT Tracker Intracellular Nucleic Acid Localization Kit (MirusBio, Madison, WI) was used to fluorescently tag plasmids with Cy5 fluorophores. DNA-NP were formed by dropwise addition of 10 volumes of labeled or unlabeled plasmids (0.2 mg/mL) to 1 volume of a swirling polymer solution. All DNA-NP were prepared at an optimized nitrogen to phosphate (N/P) ratio of 6. For the formulation of conventional PEGylated nanoparticles (CPN), PEG-PEI copolymers prepared at a PEG to PEI molar ratio of 8 alone were used to condense plasmids. BPN formulations were engineered by condensation of plasmids by a mixture of non-PEGylated PEI (25%) and PEG-PEI (75%)

synthesized at higher PEG to PEI molar ratios of 30 and 50. For microscopic observations, Cy5-labeled plasmids were used to assemble fluorescently-labeled DNA-NP. The plasmid/polymer solution was incubated for 30 minutes at room temperature to spontaneously form DNA-NP. DNA-NP were washed twice with 3 volumes of ultrapure distilled water, and re-concentrated to 1 mg/ml using Amicon Ultra Centrifugal Filters (100,000 MWCO; Millipore Corp., Billerica, MA). Plasmid concentration was determined via absorbance at 260 nm using a NanoDrop ND-1000 spectrophotometer (NanoDrop Technologies, Wilmington, DE).

2.1.3 Physicochemical characterization of DNA-NP

The hydrodynamic diameters as well as polydispersity index (PDI) and ζ-potentials of DNA-NP were measured by dynamic light scattering (DLS) and laser Doppler anemometry, respectively, in 10 mM NaCl solution at pH 7.0 using a Nanosizer ZS90 (Malvern Instruments, Southborough, MA). The size and morphology of DNA-NP were also confirmed by transmission electron microscopy (TEM; Hitachi H7600, Japan). The DNA complexation was confirmed by conventional agarose gel-based electrophoretic analysis. The colloidal stability was assessed by monitoring the change in hydrodynamic diameters and PDI in artificial cerebrospinal fluid (aCSF, Harvard Apparatus, Holliston, MA) over time at 37 °C via DLS. Number of plasmid copies in each DNA-NP was CICS, as previously reported (*33*). Briefly, DNA-NP carrying Cy5-labeled plasmids were passed through a custom-made polydimethylsiloxane-based microfluidic device to spatially constrict particles to ensure single particle detection using a HeNe laser. The fluorescence data was collected with DNA-NP immediately after the preparation or 4 hours after an incubation in aCSF. Then fluorescence readings were detected and analyzed using Labview interface (National Instruments, Austin, TX) and a MATLAB script, respectively, to determine the number of plasmid copies for each DNA-NP population. Of note, quenching artifact was carefully assessed using a particle series of increasing ratio of labeled DNA to unlabeled free-labeled plasmid DNA and including a correction factor in the final plasmid calculation.

2.2 *In vitro* experiments in 2D cell cultures

2.2.1 Cell culture

Highly aggressive rat glioma F98 cells (ATCC, Manassas, VA) were cultured in Dulbecco's modified Eagle's medium (DMEM, Invitrogen Corp., Carlsbad, CA) supplemented with 10% heat-inactivated fetal bovine serum (FBS; Invitrogen Corp.) and 1% penicillin/streptomycin (P/S; Invitrogen Corp.). All the following *in vitro* studies were conducted when cells reached 70% - 80% confluency in respective plates.

2.2.2 Cell viability

Cells were seeded onto 96-well plates at an initial density of 5,000 cells/well and grown overnight at 37 °C. Cells were treated with various DNA-NP at a wide range of plasmid doses for 48 hours at 37 °C. Cell viability was then assessed using Dojindo cell counting kit-8 (Dojindo Molecular Technologies, Inc., Rockville, MD). Absorbance at 450 nm was measured spectrophotometrically using a Synergy Mx Multi-Mode Microplate Reader (Biotek, Instruments Inc. Winooski, VT), and cell viability was determined by normalizing the readouts to absorbance measured with untreated control cells.

2.2.3 Cellular uptake

Cells were seeded onto 6-well plates at an initial density of 200,000 cells/well and grown overnight at 37 °C. Cells were treated with various DNA-NP carrying Cy5-labeled plasmids (5 μg DNA/well) and after 5 hours of incubation, the media was removed. Cells were then thoroughly washed with 1X phosphate buffered saline (PBS) and trypsinized. Flow cytometry was conducted to quantify the cellular uptake of DNA-NP using a Sony Cell Sorter SH800 (Sony, San Jose, CA), followed by data analyzed with a FlowJo software (FlowJo LLC, Ashland, OR).

2.2.4 Transgene expression

Cells were seeded at an initial density of 50,000 cells/well onto 24-well plates and grown overnight at 37 °C. Cells were then treated with various DNA-NP carrying luciferase-expressing

plasmids (i.e. pd1GL3-RL) at a plasmid concentration of 1 μg/well, and the culture media was replaced with fresh media 5 hours after the incubation. After 48 hours of additional incubation, media was removed and 0.5 ml of 1X Reporter Lysis Buffer (Promega, Madison, WI) was added. Subsequently, cells were subjected to three freeze-and-thaw cycles to achieve complete lysis followed by the collection of supernatants by centrifugation. Luciferase activity was measured in relative light units (RLU) using a standard Luciferase Assay Kit (Promega) and a 20/20n luminometer (Turner Biosystems, Sunnyvale, CA). The RLU values were normalized to the total protein content measured by a Bicinchoninic Acid (BCA) Protein Assay Kit (Thermo scientific, Rockford, IL).

In parallel, transgene expression was also evaluated by confocal microscopy. Cells were seeded in 35 mm glass-bottom dishes of which surfaces were coated with poly-D-lysine (MatTek Corporation, Ashland, MA) at an initial density of 30,000 cells/dish and grown overnight at 37 °C. Cells were then treated with various DNA-NP carrying ZsGreen- or GFP-expressing plasmids at a plasmid concentration of 1 μg/dish, and the culture media was replaced with fresh media 5 hours after the incubation. After 48 hours of additional incubation, one drop of NucBlue™ Live Cell Stain (4',6-diamidino-2-phenylindole or DAPI; Invitrogen Corp.) was added to each dish to visualize cell nuclei. Then fluorescence was captured from DAPI and ZsGreen or GFP, respectively, using an LSM 710 confocal microscope (Carl Zeiss; Hertfordshire, UK) under 20X magnification. Subsequently, images were analyzed using an ImageJ software (NIH, Bethesda, MD).

2.3 *In vitro* experiments in 3D multicellular tumor spheroids

2.3.3 Preparation of spheroids

3D tumor spheroids were established by the hanging-drop method, which cultivates the cells within an agarose matrix, blended with a house-made spheroid media, and then transferred to regular DMEM (see Figure 2.1 for various types of cell culture). The spheroid media was prepared by dissolving autoclaved methylcellulose (Sigma-Aldrich) at 2.4% (w/v) in preheated

(60 °C), serum-free DMEM followed by dilution with an equivolume of DMEM supplemented with 10% FBS and an overnight stirring at 4 °C. The solution was then centrifuged at 5,000 xg for 2 hours at 4 °C to precipitate undissolved methylcellulose and the supernatant stored at 4 °C until use. To form each spheroid, we cultured 5,000 cells, either F98 glioma cells or F98 cells engineered to constitutively express a red fluorescent protein, mKate (F98-mKate; provided Dr. Surojit Sur; Johns Hopkins University), in 20 µL spheroid media on the lid of a petri-dish. Spheroids were then grown upside down by covering a PBS-filled/moisturized petri-dish with the cell-seeded lid for 2 days. Finally, spheroids were transferred onto a sterile U-bottom 96-well plate (CELLSTAR®; Sigma-Aldrich) along with DMEM and incubated at 37ºC for 24 hours prior to their use for subsequent experiments.

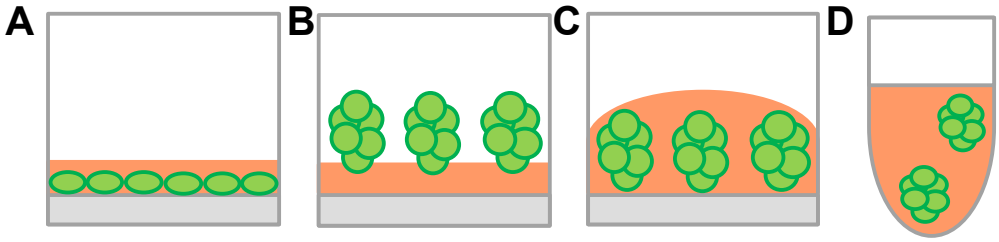

Figure 2.1: Schematic diagrams of various common methods of cell culture. (A) Traditional 2D monolayer cell culture, **(B)** 3D cell spheroids grown on matrix, **(C)** Cells embedded within matrix, or **(D)** Scaffold-free cell spheroids in suspension. Reproduced from Edmondson R. et al. 2014 with permission from Mary Ann Liebert, Inc.

2.3.2 Distribution of DNA-NP in 3D spheroids

To evaluate the ability of DNA-NP to penetrate 3D tumor spheroids, we treated F98-mKate-based spheroids with various DNA-NP carrying Cy5-labeled plasmids (1 µg plasmids/spheroid). The media was removed 5 hours after the incubation and replaced with the background-minimizing FluoroBrite DMEM. Subsequently, spheroids were fixed with 4% formaldehyde, washed with PBS, embedded in Tissue-Tek® optimal cutting temperature compound (Sakura Finetek, Torrance, CA) and sectioned into 20 µm-thick slices using Leica CM 1905 cryostat (Leica Biosystems, Buffalo Grove, IL). Slices were imaged for the fluorescence originated from F98 glioma cells (i.e. mKate) and DNA-NP (i.e. Cy5) using an LSM 710 confocal microscope

under 10X magnification. The radial distribution profile of DNA-NP was obtained by measuring the mean fluorescence intensity throughout the radial coordinates from the edge to the core of the spheroid using an ImageJ software, as previously described (*34*).

2.3.3 Transgene expression by DNA-NP in 3D spheroids

F98-based spheroids were treated with various DNA-NP carrying ZsGreen-expressing plasmids (1 μg plasmids/spheroid) to evaluate the ability of DNA-NP to mediate transgene expression in spheroids. At 5-hour post-incubation, the culture media was replaced by fresh FluoroBrite DMEM. After 48 hours of additional incubation, the spheroids were transferred on to custom-made gel-wells. To prepare a stock gel media, low gelling temperature agarose (Sigma-Aldrich) was dissolved at 5% (w/v) in sterile PBS and subsequently autoclaved. The working gel media was then made by diluting the stock with FluoroBrite DMEM to reach the final agarose concentration of 0.5% (w/v). Subsequently, a 4-well Millicell EZ slide (Millipore Corp) was filled with the working gel media and spheroids were carefully placed in each well. Fluorescence images were then captured using an LSM 710 confocal microscope under 10X magnification and analyzed for spheroid area-normalized mean fluorescence intensity using an ImageJ software.

2.4 Multiple particle tracking – *ex vivo* diffusion of DNA-NP in rat brain

Multiple particle tracking (MPT) experiments were conducted to quantify the diffusion rates of various DNA-NP carrying Cy5-labeled plasmids in healthy rat brain parenchyma *ex vivo*, as previously reported (*9, 16*). Briefly, whole brain tissues were harvested from 6-to-8-week-old female Fischer 344 rats (Harlan Laboratories, Frederick, MD) and incubated in aCSF on ice for 10 minutes. The brain tissues were then sliced using a Zivic brain matrix slicer (Zivic Instruments, Pittsburgh, PA) and the resultant 1.5-mm coronal slices were placed on custom-made slides. Subsequently, we injected 0.5 μL of DNA-NP solution at a plasmid concentration of 2 μg/mL into the cerebral cortex at a depth of 1 mm using a Neuros syringe (50 μL; Hamilton, Reno, NV) mounted on an ultra-precise small-animal stereotactic frame (Stoelting Co., Wood

Dale, IL). Trajectories of DNA-NP were recorded over 20 seconds at an exposure time of 66.7 milliseconds (i.e. 15 fames/s) by an Evolve 512 EMCCD camera (Photometrics, Tucson, AZ) mounted on an inverted epifluorescence microscope (Axio Observer D1; Carl Zeiss, Hertfordshire, UK) equipped with a 100X/1.46 NA oil-immersion objective. Movies were then analyzed with a custom-made automated particle tracking MATLAB script to extract x, y-coordinates of DNA-NP centroids over time from which the mean square displacement (MSD) values of individual DNA-NP were calculated as a function of timescale (*35*). Median MSD was determined based on the measured MSD values of individual DNA-NP at a timescale of 1 second, at which both static and dynamic errors are minimized in MPT experiments (*35*).

2.5 Animal studies

We used 6-to-8-week-old female Fischer 344 rats for the assessment of *in vivo* gene transfer efficacy of various DNA-NP. Animals were treated in accordance with the guidelines and policies of the Johns Hopkins University Animal Care and Use Committee. Surgical procedures were performed using standard sterile surgical techniques. Animals were anesthetized using a mixture of 75 mg/kg ketamine and 7.5 mg/kg xylazine, as previously described (*36*). A midline scalp incision was made to expose the coronal and sagittal sutures and a burr whole was drilled 3 mm lateral to the sagittal suture and 0.5 mm posterior to the bregma. Following the tumor cell inoculation or DNA-NP administration, the skin was sealed using biodegradable sutures (Polysorb™ Braided Absorbable Sutures 5–0) and bacitracin was applied.

2.5.3 Orthotopic tumor cell inoculation

Orthotopic tumor cell inoculation was performed, as previously described (*36*). Briefly, 100,000 cells, either F98 or F98-mKate cells, were administered in 10 µL of DMEM over 5 minutes at a depth of 3.5 mm using a Neuros Syringe mounted on an ultra-precise small-animal stereotactic frame. Of note, we inoculated rat brains with a high numbers of tumor cells, relevant to clinical translation (*37, 38*), to establish a model mimicking malignant gliomas characterized by rapid tumor growth rates.

2.5.4 Intracranial administration - CED

To assess the distribution of transgene expression, various DNA-NP carrying ZsGreen- or luciferase-expressing plasmids were intracranially administered via CED, as previously described (*9, 10*). Briefly, a Neuros syringe connected to a 33-gauge needle was filled with 20 µL of DNA-NP solution at a plasmid concentration of 1 mg/mL and lowered to a depth of 3.5 or 2.5 mm of a healthy or an orthotopic tumor-bearing rat brain, targeting the striatum or the tumor core, respectively. DNA-NP solution was then infused at a rate of 0.33 µL/min as controlled by a Chemyx Nanojet Injector Module (Chemyx, Stafford, TX).

2.5.5 Distribution and overall level of transgene expression

For assessing the distribution of transgene expression, brain tissues of rats received DNA-NP carrying ZsGreen-expressing plasmids were harvested 48 hours after the administration and subsequently fixed with 4% formaldehyde. Tissues were then sectioned using a Leica CM 1905 cryostat into 100 or 50 µm coronal slices for healthy or tumor-bearing rats at ± 3 mm of the infusion plane in striatum or until the tumor tissue was no longer visible, respectively. Slices of F98-based orthotopic tumor tissues were stained with DAPI (Molecular Probes, Eugene, OR) to visualize tumor cell nuclei. All fluorescence images were taken using an LSM 710 confocal microscope under 5X, 20X and/or 40X magnification. We carefully optimized the settings to avoid background fluorescence based on the microscopy of untreated control rat brains. The volume of transgene expression was quantified using a custom-made MATLAB script that subtracted background fluorescence by Otsu's method of thresholding (*39, 40*). The area of DNA-NP spreading in each slice was integrated to calculate the total volume of transgene expression. To reconstruct 3D-rendered imaginings, we stacked and aligned the acquired images using Metamorph ® Microscopy Automation & Image Analysis Software (Molecular Devices, CA). Finally, we used an Imaris Software (Bitplane, CT) to create 3D isosurfaces of the reconstructed images.

The kinetics of transgene expression was also determined based on the distribution of transgene expression over time. For the assessment of a short- and a long-term transgene expression, animals were treated with a BPN formulation carrying ZsGreen- and mCherry-expressing plasmids driven by CMV and human β-actin promoters, respectively. In parallel, we determine the volume of transgene expression mediated by a BPN formulation stored at 4 °C for one month, following a routine physicochemical characterization as described above.

To quantify the overall level of transgene expression, we treated rats using the identical dosing method applied to the distribution study but with various DNA-NP carrying luciferase-expressing plasmids (i.e. pBAL). Seven days after the administration, tissues were harvested and subjected to homogenate-based luciferase assay using a standard Luciferase Assay Kit and a 20/20n luminometer. The RLU values were normalized to the total protein content measured by BCA protein assay.

2.5.6 Immunofluorescence

To assess the transgene expression in different cell types, animals bearing orthotopic F98-mKate-based tumor were treated with a BPN formulation carrying ZsGreen-expressing plasmids as described above. Two days after the administration, brain tissues were harvested, sectioned and subjected to immunochemistry. Specifically, astrocytes and microglial cells were immunostained by antibodies against GFAP (Abcam, Cambridge, UK) and Iba1 (Wako Chem USA Corp., Richmond, VA). Images were taken using an LSM 710 confocal microscope under 20X and/or 40X magnification. The transgene expression in F98-mKate glioma and microglial cells was quantified using an ImageJ software based on the co-localization of different fluorescence. At least three representative fields of view from at least three different coronal sections were used for the analysis.

2.6 Statistical analysis

Statistical analysis between two groups was conducted using a two-tailed Student's t-test assuming unequal variances. If multiple comparisons were involved, one-way analysis of

variance (ANOVA), followed by Sidak's multiple comparisons test, was employed, using GraphPad Software (GraphPad Software Inc., La Jolla, CA). Differences were determined to be statistically significant at $p < 0.05$.

3. Results and discussion

3.1 Formulation and characterization of DNA-NP

We first engineered three PEI-based DNA-NP possessing different surface PEG contents. CPN were formulated by condensing plasmids solely with PEG-PEI synthesized at a moderate PEG to PEI ratio of 8, as previously reported (*9*). In parallel, we engineered two additional DNA-NP with greater surface PEG contents using a method that we have previously developed to endow gene vectors with excellent compaction and colloidal stability in physiological conditions while providing capability to efficiently penetrate healthy brain parenchyma, BPN (*9*). Specifically, a blend of non-PEGylated PEI and PEG-PEI synthesized at a high PEG to PEI ratio of 30 or 50 was used to condense plasmids to yield BPN^{L} (i.e. lower PEG BPN) or BPN^{H} (i.e. higher PEG BPN), respectively (Figure 2.2). Of note, BPN^{L} is a close relative to a PEI-based DNA-NP that we have confirmed for efficient penetration through healthy rat brain tissues *ex vivo* and *in vivo* in our previous study (*9*). We here hypothesized that a greater PEGylation, unless interferes with a capacity of PEI to form stable particles, might further enhance the ability of the resultant DNA-NP to percolate not only in healthy brain parenchyma but also in brain tumor tissues.

We found that all three freshly prepared DNA-NP exhibited similarly small sizes (i.e. ~50 nm in hydrodynamic diameters) and excellent PDI values (≤ 0.20) (Table 2.1). On the other hand, the ζ-potential, an indicative of particle surface charge, decreased from positive towards neutral values with increased PEG contents (i.e. 18.0 ± 0.2, 7.0 ± 0.3 and 2.0 ± 0.1 mV for CPN, BPN^{L} and BPN^{H}, respectively; Table 2.1), indicating that the otherwise cationic DNA-NP surfaces

were effectively masked by PEG corona, particularly more so for BPN^H that showed near-neutral ζ-potential values.

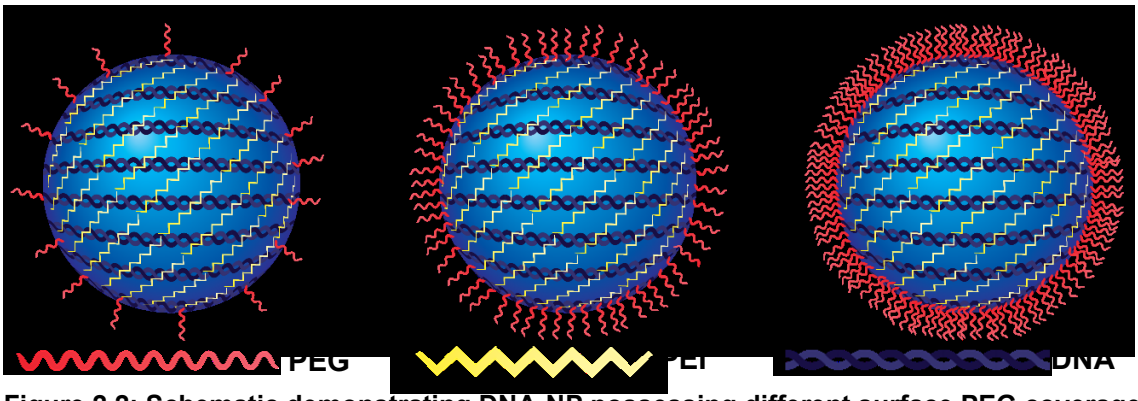

Figure 2.2: Schematic demonstrating DNA-NP possessing different surface PEG coverage. PEI (yellow)-based DNA-NP with varying surface PEG (red) densities are formulated by compacting plasmid DNA (dark blue) with PEGylated PEI alone (i.e. conventional PEGylation) or a blend of non-PEGylated and PEGylated PEI, including **(A)** conventionally PEGylated DNA-NP (CPN) and brain-penetrating DNA-NP possessing **(B)** a lower (BPN^L) and **(C)** a higher (BPN^H) PEG contents.

Table 2.1: Physicochemical properties of DNA-NP.

	Hydrodynamic diameter ± SEM (nm)[a]	PDI[a]	ζ-Potential ± SEM (mV)[b]	Hydrodynamic diameter ± SEM at 12 hours in aCSF (nm)[c]	PDI at 12 hours in aCSF[c]
CPN	50 ± 1	0.16	18.0 ± 0.2	212 ± 3	0.17
BPN^L	49 ± 1	0.19	7.0 ± 0.3	67 ± 6	0.16
BPN^H	48 ± 5	0.20	2.0 ± 0.1	56 ± 3	0.15

[a] Hydrodynamic diameter and polydispersity index (PDI) were measured by dynamic light scattering (DLS) in 10 mM NaCl. Mean ± SEM (n ≥ 3).

[b] ζ-potential was measured by laser Doppler anemometry in 10mM NaCl at pH 7.0. Mean ± SEM (n ≥ 3).

[c] Hydrodynamic diameter and PDI were measured by DLS following a 12-hour incubation in aCSF at 37ºC.

The particle morphology was confirmed by TEM to be ~50 nm spheres regardless of PEG contents (Figure 2.3A-C), in consistent with the measured hydrodynamic diameters (Table 2.1). We found that BPN candidates formulated with an inclusion of PEG-PEI synthesized at even higher PEG to PEI ratios of 60 and 85 exhibited similar physiochemical properties as BPN^H (Table 2.2), and thus excluded in subsequent evaluations. We then verified robust DNA compaction by all three different DNA-NP via a conventional agarose-gel migration assay;

however, CPN, regardless of its lower PEG content, showed a brighter signal in the well compared to BPN^L and BPN^H, suggesting that an inclusion of non-PEGylated PEI in the blended BPN formulations might have enhanced their abilities to compact the plasmid payloads (Figure 2.3D).

In addition to these conventional physicochemical characterization, we conducted an additional analysis to quantify the average number of plasmid copies per different DNA-NP using cylindrical illumination confocal spectroscopy (CICS) technique (*33*). We found that each CPN contained an average of approximately four plasmid copies, whereas BPN^L and BPN^H packaged roughly two copies on average (Figure 2.3F). The finding suggests that double the amount (i.e. number of particles) of both BPN formulations will be administered compared to

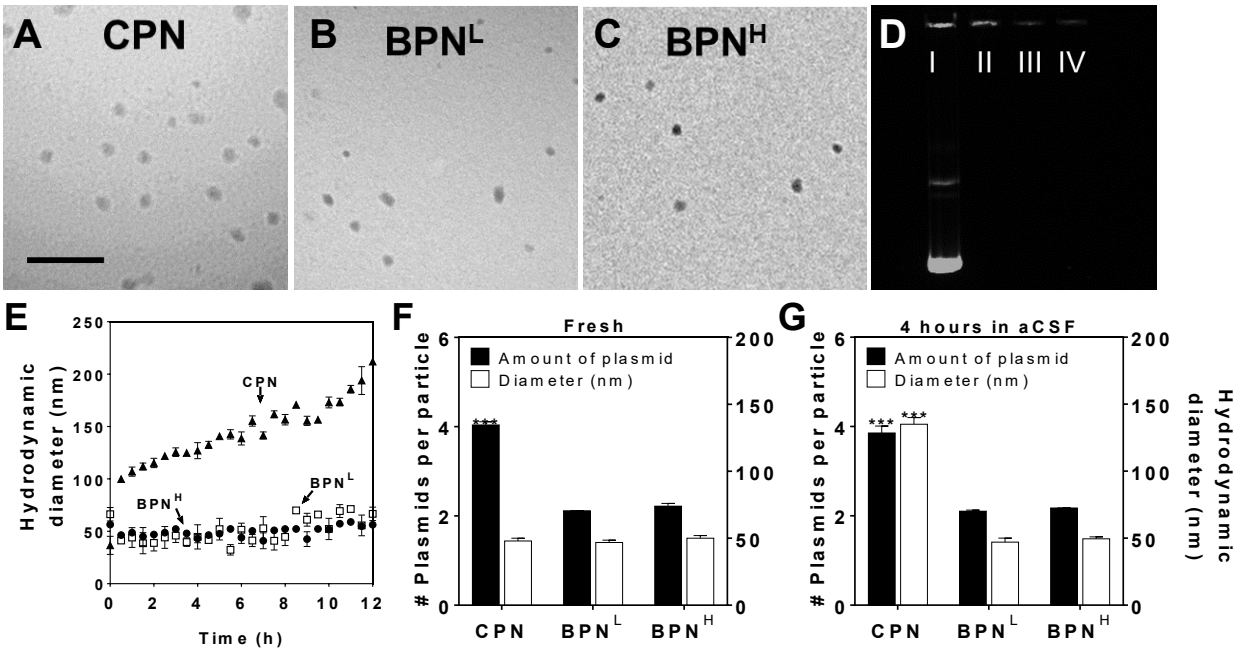

Figure 2.3: Physicochemical properties and stability of DNA-NP. Transmission electron microscopy images of **(A)** CPN, **(B)** BPN^L, and **(C)** BPN^H freshly made in ultrapure water. Scale bar = 400 nm. **(D)** Compaction of plasmids in DNA-NP shown by electrophoresis: I) free DNA, II) CPN, III) BPN^L, IV) BPN^H. Number of plasmids in each DNA-NP and hydrodynamic diameter of DNA-NP when **(E)** freshly made in water and **(F)** when incubated in aCSF for 4 hours. **(G)** Change in hydrodynamic diameters over 12 hours in aCSF at 37°C measured by DLS. ***denotes a statistically significant difference of CPN compared to BPN^L and BPN^H ($p < 0.001$).

CPN at a fixed treatment dose of plasmids; this may be beneficial for enhancing gene transfer efficacy given a prior observation that the total amount of plasmid-containing particles

rather than the overall plasmid quantity is the limiting factor for PEI-mediated transfection (*41*). We next assessed the hydrodynamic diameters and plasmid copies per particle of different DNA-NP following a 4-hour incubation in aCSF at 37ºC to predict potential alteration of particle properties in the physiological brain environment. We found that while both BPN formulations retained their hydrodynamic diameters in aCSF, the size of CPN incremented near to ~150 nm (Figure 2.3E) and continue to grow afterward, suggesting that CPN would be unlikely to efficiently penetrate brain tissues due to large particle size as well as positively charged particle surfaces. In contrast, the average number of plasmid copies per particle did not change upon aCSF incubation regardless of the DNA-NP type. The finding reveals that the increase in CPN size in aCSF is most likely attributed to particle swelling rather than aggregation, providing an additional evidence that inclusion of non-PEGylated PEI in the blended BPN formulations endowed DNA-NP with an enhanced plasmid compaction stability.

Table 2.2: Physicochemical properties of DNA-BPN^{H} at higher PEG:PEI ratios.

PEG:PEI molar ratio	Hydrodynamic diameter ± SEM (nm)[a]	PDI[a]	ζ-Potential ± SEM (mV)[b]
$BPN^{H}_{65:1}$	43 ± 4	0.20	2.2 ± 10
$BPN^{H}_{80:1}$	50 ± 9	0.22	2.1 ± 2.6

[a] Hydrodynamic diameter and polydispersity index (PDI) were measured by dynamic light scattering (DLS) in 10mM NaCl at pH 7.0. Mean ± SEM (n ≥ 3).

[b] ζ-potential was measured by laser Doppler anemometry in 10mM NaCl at pH 7.0. Mean ± SEM (n ≥ 3).

3.2 Transfection efficiency of DNA-NP in 2D culture versus 3D spheroid model

We initially sought to investigate the *in vitro* transfection efficiency of different DNA-NP formulated to carry the most widely used reporter, GFP. However, evidences suggest that immunogenicity and cytotoxicity of GFP potentially confound the interpretation of *in vitro* and/or *vivo* transfection data (*42-44*). Therefore, we compared the cytotoxicity and transfection efficiency, as measured by mean fluorescence intensity, of GFP with those of ZsGreen in F98

rat glioma cells following the treatment of cells with lipofectamine carrying respective plasmids at an identical dose. We found that GFP exhibited greater (i.e. ~3-fold) toxicity and lower (i.e. ~5-fold) transfection efficiency than ZsGreen (Figure 2.4), in agreement with previous reports (*45, 46*). We thus pursed the following studies with different PEI-based DNA-NP, including CPN, BPN^{L} and BPN^{H}, carrying ZsGreen-expressing plasmids.

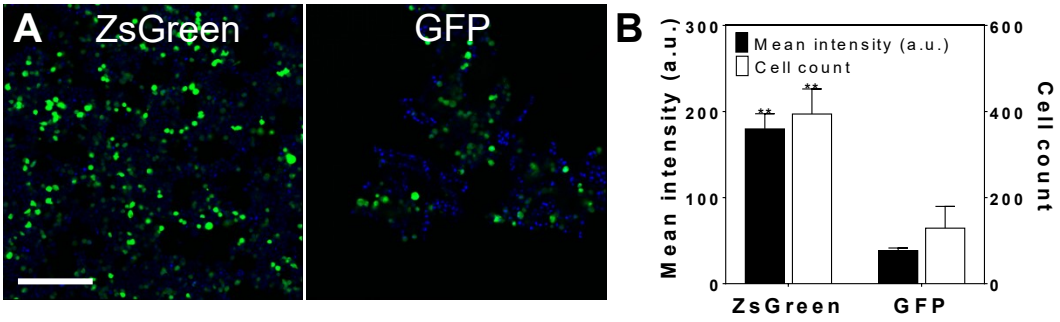

Figure 2.4: Relative *in vitro* transgene expression and toxicity of ZsGreen and GFP in F98 cells. (A) Representative confocal images at 20X magnification showing ZsGreen (left) and GFP (right) transgene expression 2 days after the transfection with lipofectamine. Scale bar = 250 μm. **(B)** Quantitative analysis of transgene expression and toxicity as measured by mean fluorescence intensity and cell viability, respectively. **denotes statistically significant differences compared to GFP ($p < 0.01$).

We first evaluated the cytotoxicity of DNA-NP at various concentrations of plasmid payloads following 48 hours of incubation. All DNA-NP showed comparably good cell viability (i.e. ~100%) at the plasmid concentrations of 1 and 5 μg/mL, but CPN, but not BPN formulations, resulted in over 40% cell death at 10 μg/mL ($p < 0.001$) (Figure 2.5A). However, we note that the 10 μg/mL plasmid concentration is markedly great than conventional working concentrations for *in vitro* transfection experiments.

We then assessed *in vitro* cellular uptake and transfection efficiency of DNA-NP carrying Cy5-labeled and unlabeled plasmids, respectively, using an F98-based 2D cell culture. The percentage of cells that took up detectable amounts of Cy5-labeled plasmid payloads were all ~100% regardless of the type of DNA-NP (Figure 2.5B), in agreement with our and others' observations that PEGylation does not completely block individual cells to engulf small nanoparticles (*9, 10, 47, 48*). However, the amounts of internalized DNA-NP per cell, as

indicated by fluorescence intensity, were significantly lower for BPN^L and BPN^H in comparison to CPN ($p < 0.001$; Figure 2.5B). Considering that each BPN carries 2 copies of DNA compared to 4 for each CPN, it seems to indicate similar or only slightly low uptake efficiency per nanoparticle, although potential impacts of dense PEG on other intracellular processes cannot be fully excluded (*49*). Accordingly, *in vitro* transfection efficiencies of BPN^L and BPN^H, as confirmed by confocal microscopy and homogenate-based luminescence assay ($p < 0.001$), were lower than those of CPN (Figure 2.5C-D).

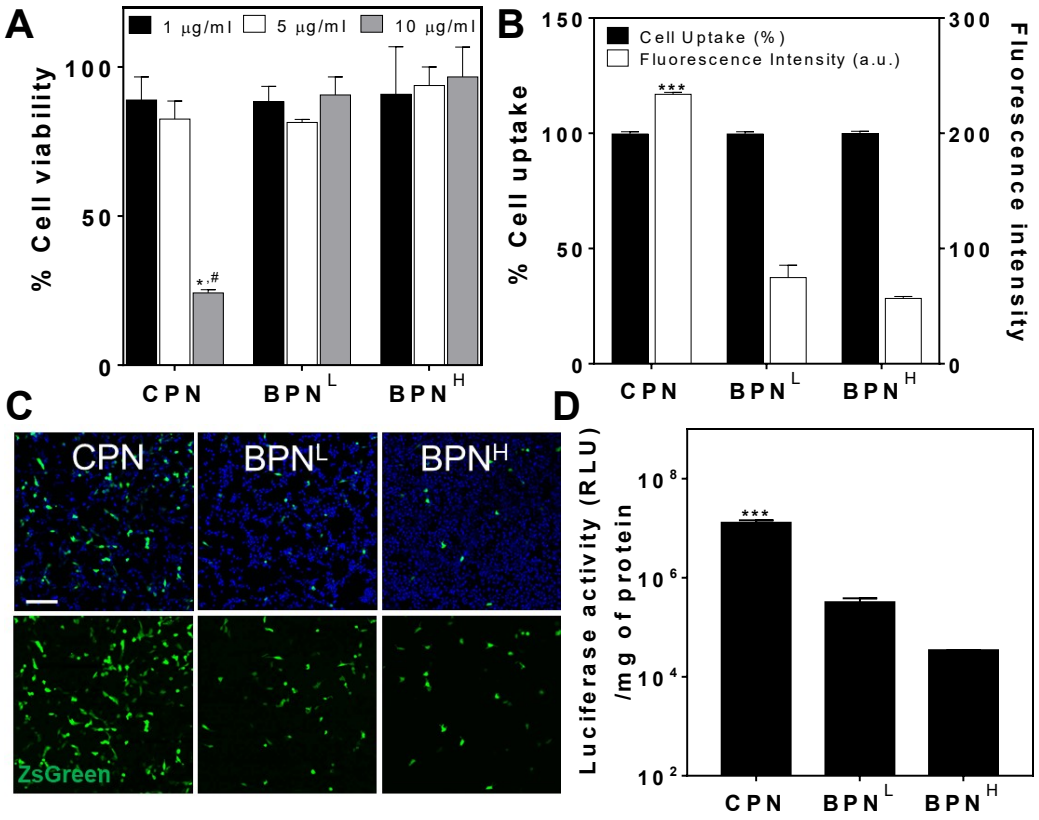

Figure 2.5: Cell viability, cell uptake and transfection in F98-based 2D cell cultures. (A) Cell viability measured 48 hours after NP-treatment at varying plasmid concentrations, in comparison to an untreated control. #denotes statistically significant differences in comparison to other concentrations and *denotes statistically significant differences in comparison to BPN^L and BPN^H at 10 µg/ml ($p < 0.001$). **(B)** Flow cytometry analysis of percentage cell uptake and median fluorescence intensity (i.e. degree of cell uptake per cell) 5 hours after NP-treatment with different DNA-NP. **(C)** Representative confocal images at 20X magnification showing ZsGreen reporter transgene expression (green) 48 hours after NP-treatment carrying ZsGreen-expressing plasmids. Cell nuclei are stained by DAPI (blue). Scale bar = 100 µm. **(D)** *In vitro* luciferase transgene expression 48 hours after NP-treatment carrying luciferase-expressing plasmids. Data represented as mean ± SEM. ***denotes statistically significant differences of CPN compared to BPN^L and BPN^H ($p < 0.001$).

Importantly, 2D cell cultures, due in part to the absence of extracellular components, do not provide a reliable model for predicting *in vivo* performances of gene vectors. We thus investigated *in vitro* behaviors of DNA-NP in an F98-based 3D model of multicellular tumor spheroid that better recapitulates architecture and biology of solid tumors observed *in vivo* (*50*). In particular, 3D spheroid models simulate an ECM-filled intercellular permeability barrier (*50-53*), and thus serve as an excellent model to evaluate the penetration of gene vectors through solid tumor tissues (*54*). To this end, we constructed a 3D spheroid model with F98-mKate cells and assessed distribution of different DNA-NP carrying Cy5-labeled plasmids. As shown by representative confocal images, DNA-NP with denser surface PEG coronas exhibited greater inward penetration compared to those with less PEG contents (BPN^H > BPN^L > CPN; Figure 2.6A).

Quantitatively, BPN^H showed the greatest spheroid penetration in the radial profile from the edge (coordinate 0) to the core (coordinate 1) of the spheroid, followed by the BPN^L and CPN (Figure 2.6B). We then evaluated the distribution and level of transgene expression following the treatment of the spheroids with DNA-NP carrying ZsGreen-expressing plasmids. Similar to the vector distribution study (Figure 2.6A), representative confocal images revealed a greatest distribution of transgene expression by BPN^H compared BPN^L and CPN with CPN exhibiting a weakest distribution (Figure 2.6C). In addition, BPN^H, but BPN^L, showed significantly greater level of transgene expression, as measured by mean fluorescence intensity, compared to CPN ($p < 0.05$; Figure 2.6D). While the average fluorescence intensity of BPN^L was ~4-fold greater than that of CPN, statistical significance was not achieved presumably due to variability of the transgene expression mediated by BPN^L in different individual spheroids (Figure 2.6D). The findings here underscore that, in contrast to the observations with 2D cultures (Figure 2.5), DNA-NP with greater surface PEG coverage provides superior transgene expression compared to those with lesser PEG, due to the ability to efficiently penetrate the extracellular barrier established in tumor spheroids.

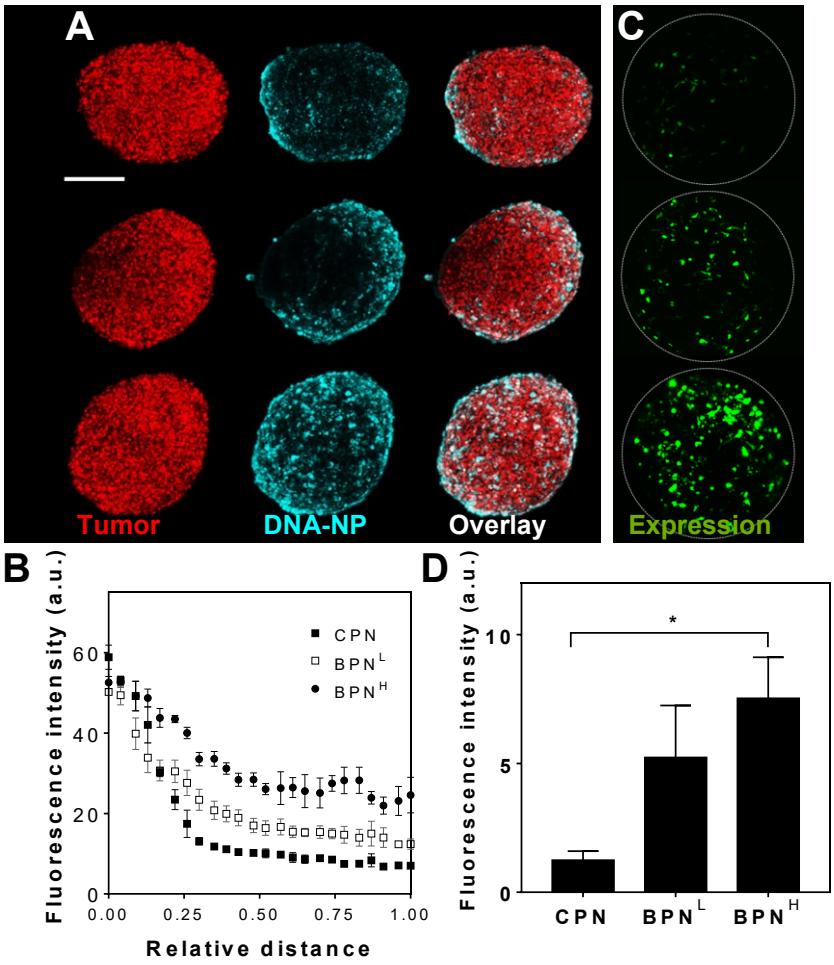

Figure 2.6: *In vitro* DNA-NP distribution and transgene expression in F98-based 3D spheroids. **(A)** Representative images showing F98 tumor spheroids (red; mKate) 5 hours after treatment with DNA-NP (cyan; Cy5). Scale bar = 250 μm. **(B)** Quantification of radial distribution of DNA-NP within the spheroids. The coordinates 0 and 1 indicate the spheroid edge and core, respectively. **(C)** Representative reporter transgene expression (green; ZsGreen) by DNA-NP carrying ZsGreen-expressing plasmids 48 hours after NP-treatment. **(D)** Quantification of ZsGreen transgene expression within the spheroids. *denotes a statistically significant difference ($p < 0.05$).

3.3 *Ex vivo* diffusion of DNA-NP in rodent brain tissues

We have previously demonstrated that diffusion rates of nanoparticles, measured by MPT, in brain tissues *ex vivo* reliably predict their spread in brain parenchyma *in vivo* (*5, 8-10*). We thus conducted MPT experiments to confirm that a greater surface PEG coverage resulted in enhanced brain penetration by DNA-NP. Specifically, DNA-NP carrying Cy5-labled plasmids were injected into a freshly harvested healthy rat brain tissue and their diffusion was monitored over a time period of 20 seconds. As evidenced by the highly constrained trajectory, CPN were

immobilized in the brain parenchyma. In contrast, BPN^L and BPN^H demonstrated relatively unhindered motions, leading to trajectories that span several microns in distance (Figure 2.7A). We then quantified their diffusion rates of DNA-NP by measuring the MSD; which represents an averaged square of distances traveled by individual particles within a given time interval and thus MSD values are directly proportional to respective particle diffusion rates.(*55*) In consistent with our prior observation (*9*), BPN^L exhibited significantly greater MSD values compared to CPN ($p < 0.001$), but we found here that increasing the surface PEG coverage further enhanced the ability of PEI-based DNA-NP to penetrate brain tissue *ex vivo* (i.e. $BPN^H > BPN^L > CPN$; Figure 2.7B). We also note that BPN^H exhibited more uniform high MSD values than BPN^L, suggesting that BPN^H may provide a more consistent ability to penetrate through the highly heterogeneous tumor microenvironment.

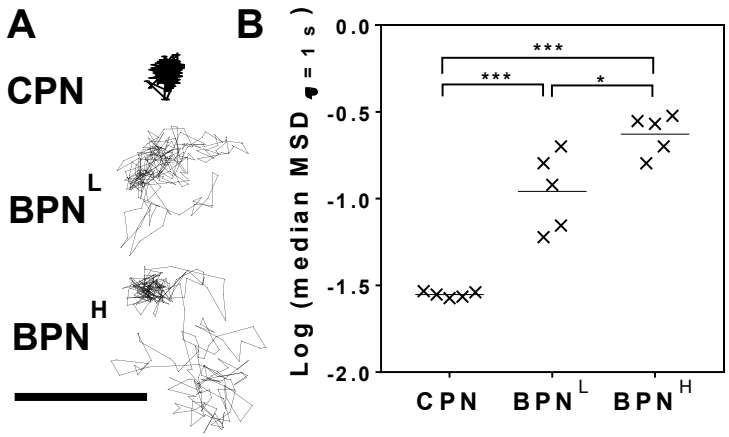

Figure 2.7: *Ex vivo* diffusion of different DNA-NP in rat brain tissues. (A) Representative trajectories of DNA-NP in rat brain tissue over 20 seconds. Scale bar = 1 μm. **(B)** Logarithms of median mean square displacements (MSD) of DNA-NP at a time scale of 1 second. Data represent 5 independent experiments with n ≥ 200 particles tracked for each experiment. Differences are statistically significant as indicated (*$p < 0.05$; ***$p < 0.001$).

3.4 Transgene expression mediated by DNA-NP in healthy brain parenchyma

We next investigated whether *ex vivo* diffusion behaviors of DNA-NP translated to their *in vivo* distribution patterns in healthy rat brain. Different DNA-NP carrying ZsGreen-expressing plasmids were administered into the rat striatum via CED that has been clinically applied to enhance the therapeutic distribution within brain by creating a continuous pressure-driven bulk

flow (*39, 56*). Transgene expression was then assessed 48 hours after the treatment. The 3D reconstruction of confocal images of serial coronal sections of rat brains revealed enhanced volumes of transgene expression when rats were treated with DNA-NP possessing greater surface PEG coverage (Figure 2.8A). The transgene expression mediated by CPN was confined to the site of administration despite the pressure gradient provided by CED. Inability of conventional cationic gene vectors to provide widespread transgene expression regardless of CED may have attributed to a limited success in a phase I/II clinical trial in which patients with glioblastoma received non-PEGylated DNA-NP formulated with cationic lipids via CED (*57, 58*). In agreement with our previous observation (*9*), BPN^{L} exhibited significantly greater volumetric distribution of transgene expression than CPN ($p < 0.01$), but importantly, BPN^{H}, mostly likely due to its superior ability to penetrate the brain parenchyma (Figure 2.8), roughly doubled the transfected volume on average in the rat striatum compared to BPN^{L} ($p < 0.001$; Figure 2.8B). In parallel, we quantitatively determined the overall levels of transgene expression mediated by CED of BPN^{H}, BPN^{L} and CPN carrying luciferase-expressing plasmids, using a homogenate-based luciferase assay. Like the trend observed with the transfected volume, DNA-NP possessing greater surface PEG contents provided greater overall levels of transgene expression; BPN^{H} exhibited statistically significant improvements ($p < 0.001$) with ~20- and ~210-fold greater luciferase activities in comparison to BPN^{L} and CPN, respectively (Figure 2.7C). The findings here suggest that the unique ability of BPN^{H} to further increase the volumetric distribution of transgene expression over BPN^{L} led to quantum enhancement of the overall gene transfer efficacy. Efforts towards greater transfection efficiencies often focus on enhancing cellular gene delivery to a specific cell type of interest, but this study provides an example underscoring the importance of achieving a greater coverage of transgene expression in a target tissue.

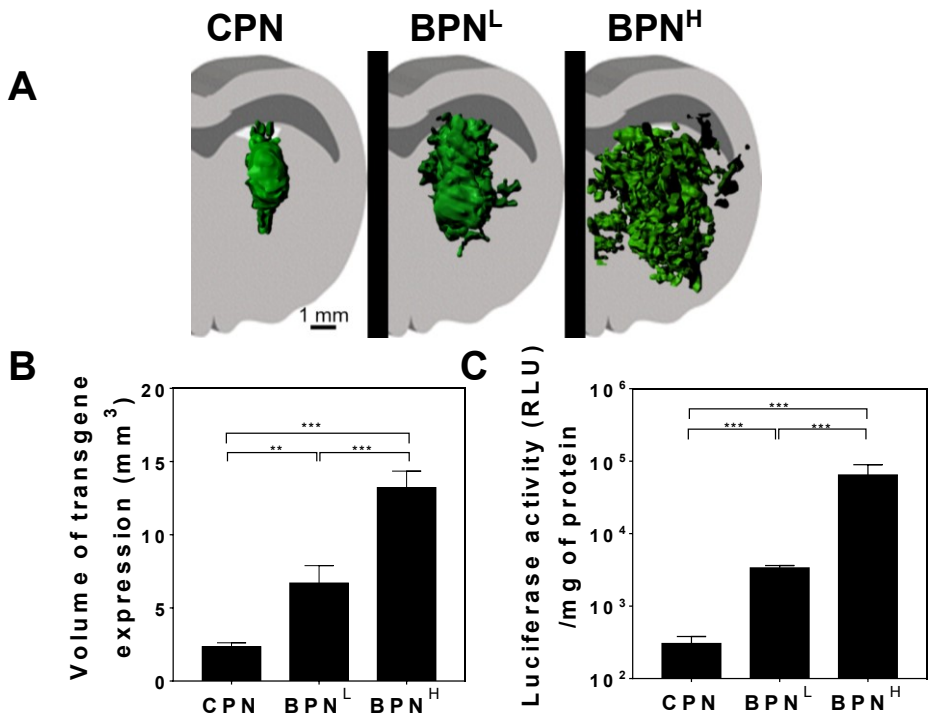

Figure 2.8: *In vivo* transgene expression mediated by CED of different DNA-NP carrying ZsGreen- or luciferase-expressing plasmids in healthy rat brain tissues. (A) Representative isosurface 3D images depicting volumetric distribution of ZsGreen reporter transgene expression (green) in healthy rat brains, obtained by stacking multiple sequential confocal images 48 hours after NP-treatment carrying ZsGreen-expressing plasmids. Scale bar = 1 mm. **(B)** Volume of ZsGreen transgene expression (n ≥ 6 rats). **(C)** Overall level of luciferase transgene expression (n ≥ 6 rats). Differences are statistically significant as indicated (**p < 0.01; ***p < 0.001).

To evaluate the expression kinetics of BPN^H in healthy rat brains, we treated rats via CED with BPN^H carrying plasmids controlled either by the CMV or by the long-acting human β-actin promoter. We found that peak volume of transgene expression lasted up to 2 days or 3 weeks upon a single treatment when regulated by CMV or human β-actin promoter (Figure 2.9), respectively, suggesting that the life span of transgene expression mediated by can be tuned by a careful selection of a promoter. We also confirmed that BPN^H retained the brain-penetrating physiochemical properties (i.e. small particle diameters and near-neutral surface charges; Table 2.3) and the ability to yield widespread transgene expression in rodent striatum at least for 1 month when stored at 4ºC (Figure 2.10).

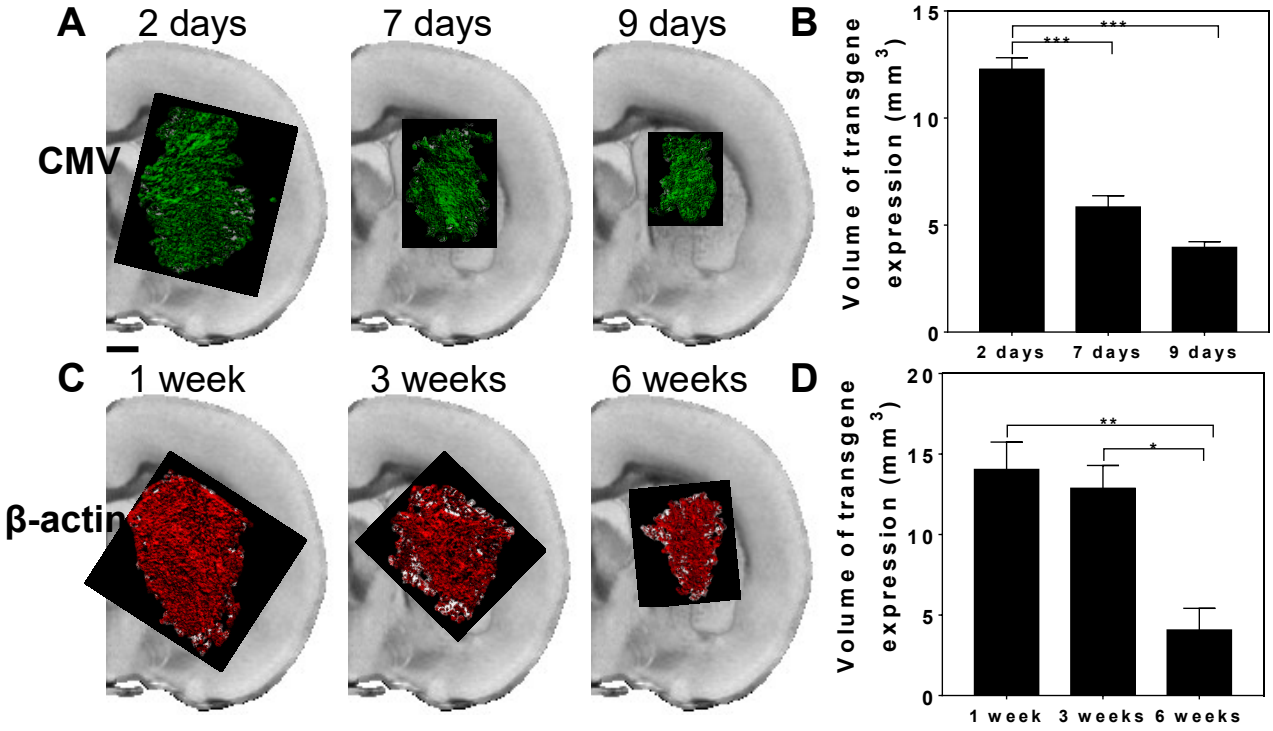

Figure 2.9: Transgene expression kinetics of fluorescent proteins controlled by CMV or β-actin promoter in healthy rat brains following CED of BPN^{H}. (A) Representative isosurface 3D images depicting volumetric distribution of ZsGreen reporter transgene expression (green) driven by CMV promoter in healthy rat brains at varying time points after the administration. **(B)** Volume of ZsGreen transgene expression (n ≥ 3 rats). **(C)** Representative isosurface 3D images depicting volumetric distribution of mCherry reporter transgene expression (red) driven by β-actin promoter in healthy rat brains at varying time points after the administration. **(D)** Volume of mCherry transgene expression (n ≥ 3 rats). Scale bar = 1 mm. Differences are statistically significant as indicated (*p < 0.05; **p < 0.01; ***p < 0.001).

Table 2.3: Physicochemical properties of DNA-BPN^{H} stored at 4ºC for 1 month.

Storage time	Hydrodynamic diameter ± SEM (nm)[a]	PDI[a]	ζ-Potential ± SEM (mV)[b]
Fresh	55 ± 4	0.15	2.1 ± 1.3
1 month	61 ± 2	0.17	3.2 ± 2.4

[a] Hydrodynamic diameter and polydispersity index (PDI) were measured by dynamic light scattering (DLS) in 10mM NaCl at pH 7.0. Mean ± SEM (n ≥ 3).
[b] ζ-potential was measured by laser Doppler anemometry in 10mM NaCl at pH 7.0. Mean ± SEM (n ≥ 3).
***p < 0.001).

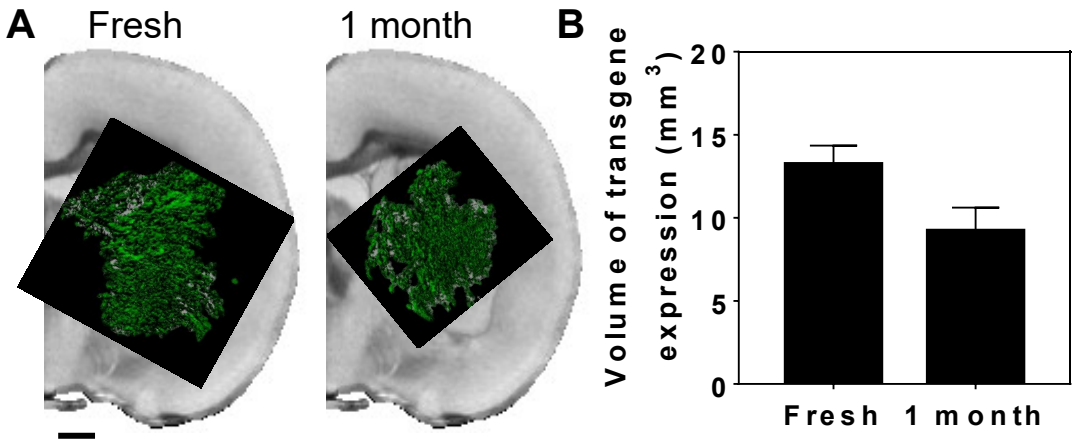

Figure 2.10: *In vivo* transgene expression mediated by BPN^{H} carrying ZsGreen-expressing plasmids, stored at 4ºC for one month, in healthy rat brains following CED. **(A)** Representative isosurface 3D images depicting volumetric distribution of Zsgreen reporter transgene expression (green) in healthy rat brains, obtained by stacking multiple sequential confocal images. Scale bar = 1 mm. **(B)** Volume of Zsgreen transgene expression (n ≥ 3 rats). The difference is not statistically significant.

3.5 Transgene expression mediated by DNA-NP in orthotopic brain tumors

We next evaluated *in vivo* gene transfer efficacy of BPN^{H}, BPN^{L} and CPN carrying ZsGreen-expressing plasmids in an orthotopic model of aggressive brain tumor following CED. The model was established by intracranial stereotactic inoculation of 1 x 10^5 F98 cells and a CED experiment was conducted 10 days after the inoculation when a large volume (~30 mm^3) of orthotopic tumor was established in the rat striatum. As shown by representative 3D-reconstructed images, BPN^{H} exhibited the greatest volumetric distribution of transgene expression, followed by BPN^{L} and CPN (Figure 2.11A). The volume of transgene expression achieved by BPN^{H} was ~2- and ~3.5-fold greater than BPN^{L} ($p < 0.05$) and CPN ($p < 0.001$), respectively, in the orthotopic brain tumor (Figure 2.10B). We then quantified the volumetric fractions of the orthotopic tumor with reporter transgene expression mediated by different DNA-NP. The percentages of total tumor volumes exhibited positive reporter transgene expression were ~90%, ~65% and ~35% for BPN^{H}, BPN^{L} and CPN, respectively, with statistically significant differences between all different DNA-NP groups (Figure 2.11C). Importantly, the finding here is in good accordance with our observation with a 3D tumor spheroid model (Figure 2.5) but

opposite to the trend shown in a 2D culture (Figure 2.4). To this end, 3D tumor spheroid models, providing good *in vivo* correlation unlike 2D culture, may serve as a reliable *in vitro* surrogate to screen newly engineered gene vectors prior to their evaluation for *in vivo* cancer gene delivery.

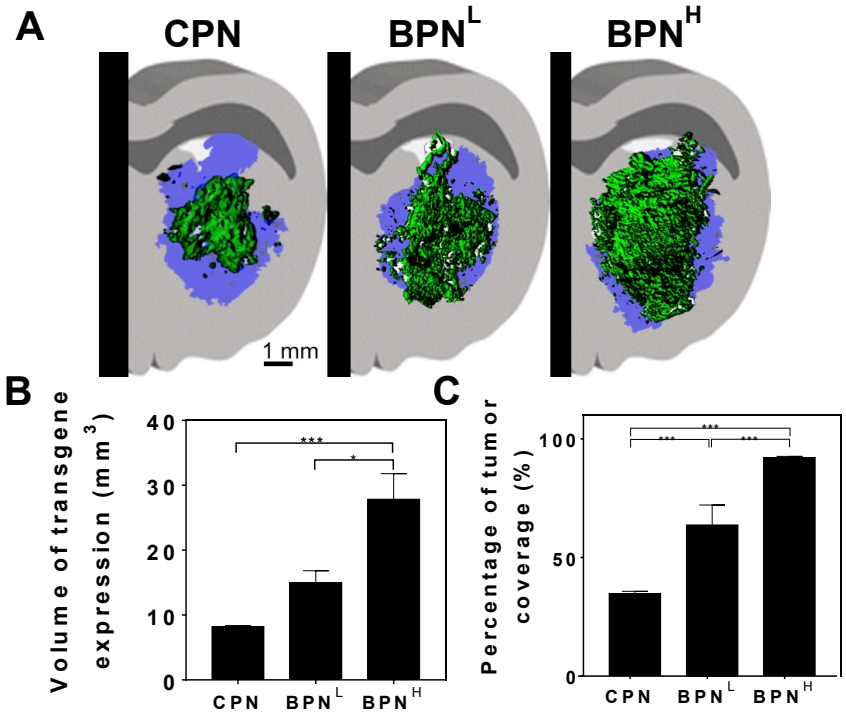

Figure 2.11: Transgene expression mediated by CED of different DNA-NP carrying ZsGreen-expressing plasmids in F98-based orthotopic rat brain tumor tissues. (A) Representative isosurface 3D images depicting volumetric distribution of ZsGreen reporter transgene expression (green) in orthotopic brain tumors (light blue), obtained by stacking multiple sequential confocal images. Scale bar = 1 mm. **(B)** Volume of transgene expression (n ≥ 4 rats). **(C)** Percentage of tumor volume covered by transgene expression (n ≥ 4 rats). Differences are statistically significant as indicated (*$p < 0.05$; ***$p < 0.001$).

In this study, we noticed that the volume of transgene expression mediated by identically administered DNA-NP was significantly greater in F98-based orthotopic tumor than in healthy rat brain (Figure 2.8 and 2.11). This is not readily expected *a prior* as the high cellularity commonly found in tumors would render the intercellular spaces narrower, thereby potentially reinforcing the tumor ECM as a steric barrier. We speculate that the greater volumetric transgene expression shown in the orthotopic model may be in part attributed to the heterogeneous nature of tumor microenvironment (*32*), specifically the necrotic regions through which BPN formulations can spread out relatively unhindered. In addition, the characteristic high

intratumoral pressure (*59*) may have facilitated outward diffusion of DNA-NP from the core to the tumor edge.

Highly invasive tumor cells that migrate beyond the tumor edge and infiltrate into normal brain tissue are responsible for recurrence of malignant gliomas (*60*). Thus, the unique ability of BPN^H to efficiently penetrate both normal brain parenchyma and brain tumor tissue may serve favorably for this specific application. However, an additional method to confine therapeutic transgene expression to tumor cells would be desired, particularly when therapy can exert a toxic effect to normal tissues (e.g. cytotoxic genes).

3.6 *In vivo* cell tropism of BPN^H in orthotopically established malignant glioma

While we showed robust reporter transgene expression by BPN^H in an orthotopically established malignant glioma, the tumor volume and edge were estimated based on the high tumor-cell cellularity, uncovered by a conventional DAPI staining. Therefore, we established an orthotopic model as described above but with F98 cells constitutively expressing fluorescent mKate (i.e. F98-mKate) to confirm whether the transgene expression indeed took place in tumor cells *in vivo*. We first determined F98 cells to be the most abundant cells within the orthotopically-established tumor tissue (Figure 2.12). Microglial cells were also ubiquitously present within the tumor bulk, as expected from their roles in glioma maintenance and progression,(*61*) whereas neuron-supporting astrocytes were rarely found (Figure 2.12).

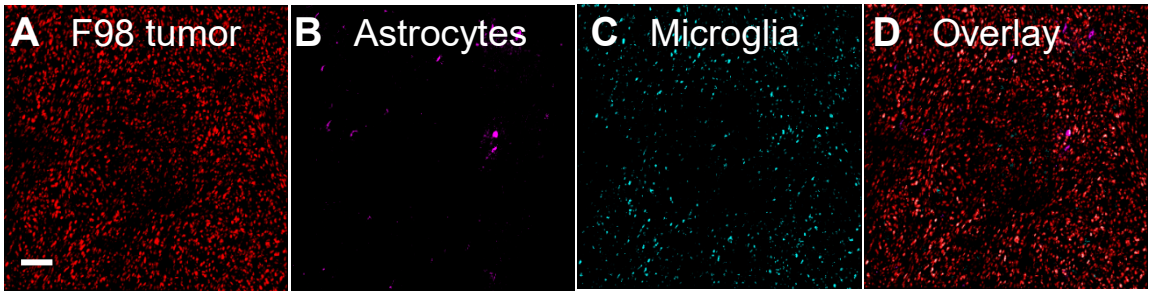

Figure 2.12: Cell population in an orthotopically established F98 rat tumor tissue. Representative 2D confocal images at 20X magnification (tile scan) showing **(A)** F98 tumor cells (red; mKate), **(B)** astrocytes (magenta; GFPA), **(C)** microglia (cyan; Iba1) and **(D)** overlay. Scale bar = 100 μm.

We then treated rats harboring orthotopic mKate-expressing F98 tumor with BPN^{H} carrying ZsGreen-expressing plasmids via CED and evaluated relative transgene expression in those two cells most highly prevalent in the tumor, including F98 and microglial cells. We found that ~90% and ~30% of F98 and microglial cells, respectively, were positive to BPN^{H}-mediated ZsGreen transgene expression, as determined by image-based analysis of randomly selected confocal image fields (Figure 2.13). The BPN^{H} is not specifically designed to preferentially target cancer cells and thus a ~3-folder greater number of transfected cells for F98 over microglial cells was not readily assumed. It is most likely that passive mechanisms have been involved. A relatively larger number of F98 cells in the tumor tissue as well as high endocytic activities often observed with tumor cells (*62-64*) may render them a better "particle sink" compared to other brain-resident cells, such as microglial cells. In addition, mitotic activities of brain-resident cells are very low, whereas glioma cells are highly mitotic (*39*), thereby enhancing the probability of plasmid payloads entering into the nucleus to be transcribed. We note that while the described are reasonable scenarios, further mechanistic underpinning should be followed to elucidate a full picture.

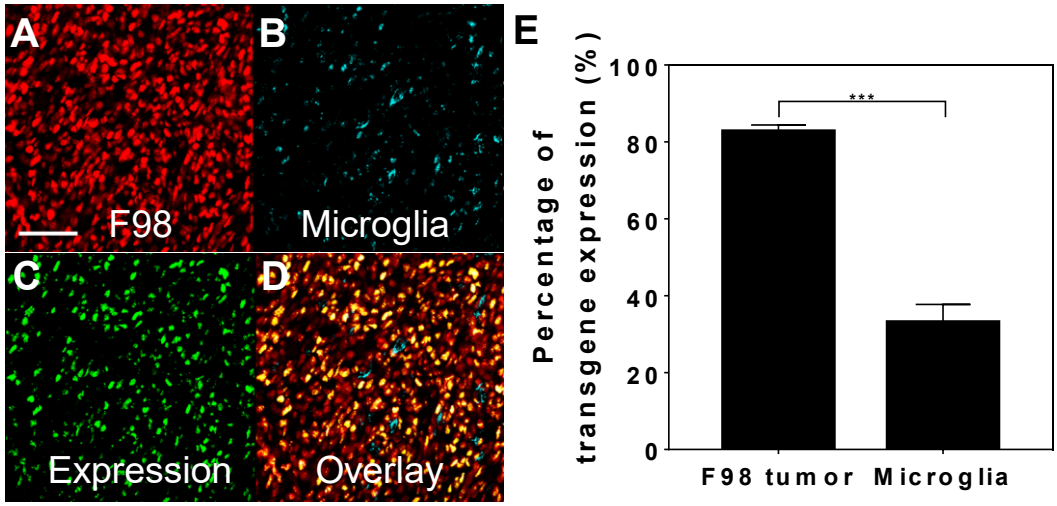

Figure 2.13: Transgene expression mediated by BPN^{H} carrying ZsGreen-expressing plasmids in F98-mKate orthotopic rat tumor tissues. Representative confocal images at 40X magnification showing **(A)** F98 tumor cells (red; mKate), **(B)** microglia (cyan; Iba1), **(C)** transgene expression (green; ZsGreen) and **(D)** overlay. Scale bar = 50 μm. **(E)** Quantification of percentage of F98 tumor and microglia cells with the transgene expression. ***denotes a statistically significant difference ($p < 0.001$).

4. Conclusions

Here, we introduce a novel polymer-based gene vector capable of efficiently penetrating both healthy brain parenchyma and brain tumor tissue. Specifically, a lead formulation, BPN^H, exhibited the greatest ability to provide widespread and high-level transgene expression in 3D tumor spheroids and orthotopically-established brain tumors compared to formulations with inferior surface PEG coatings, with an excellent *in vitro*-to-*in vivo* correlation. We note that while the transgene expression occurred preferentially in gliomas cells within orthotopically-established tumor tissue, a significant expression was observed in microglial cells as well. Thus, an additional strategy is likely needed if highly selective cancer cell transfection is required, while retaining the ability to cover widely scattered tumor areas within the brain. To this end, our current effort focuses on achieving widespread but cancer-selective therapeutic transgene expression via a marriage of BPN^H and promoters designed to drive transgene expression specifically in cancer cells.

5. References

1. M. E. Davis, Glioblastoma: Overview of Disease and Treatment. *Clin J Oncol Nurs* **20**, S2-8 (2016).
2. S. Chira *et al.*, Progresses towards safe and efficient gene therapy vectors. *Oncotarget* **6**, 30675-30703 (2015).
3. K. J. Pulkkanen, S. Yla-Herttuala, Gene therapy for malignant glioma: current clinical status. *Mol Ther* **12**, 585-598 (2005).
4. A. M. Murphy, S. D. Rabkin, Current status of gene therapy for brain tumors. *Transl Res* **161**, 339-354 (2013).
5. E. A. Nance *et al.*, A dense poly(ethylene glycol) coating improves penetration of large polymeric nanoparticles within brain tissue. *Sci Transl Med* **4**, 149ra119 (2012).
6. E. Sykova, C. Nicholson, Diffusion in brain extracellular space. *Physiological reviews* **88**, 1277-1340 (2008).
7. E. Nance, in *Biomedical Nanotechnology: Methods and Protocols,* S. H. Petrosko, E. S. Day, Eds. (Springer New York, New York, NY, 2017), pp. 91-104.
8. C. Zhang *et al.*, Strategies to enhance the distribution of nanotherapeutics in the brain. *J Control Release* **267**, 232-239 (2017).
9. P. Mastorakos *et al.*, Highly PEGylated DNA Nanoparticles Provide Uniform and Widespread Gene Transfer in the Brain. *Adv Healthc Mater* **4**, 1023-1033 (2015).
10. P. Mastorakos *et al.*, Biodegradable DNA Nanoparticles that Provide Widespread Gene Delivery in the Brain. *Small* **12**, 678-685 (2016).
11. J. Chen, Z. Guo, H. Tian, X. Chen, Production and clinical development of nanoparticles for gene delivery. *Mol Ther Methods Clin Dev* **3**, 16023 (2016).
12. O. M. Merkel *et al.*, In vitro and in vivo complement activation and related anaphylactic effects associated with polyethylenimine and polyethylenimine-graft-poly(ethylene glycol) block copolymers. *Biomaterials* **32**, 4936-4942 (2011).

13. B. Shi *et al.*, Challenges in DNA Delivery and Recent Advances in Multifunctional Polymeric DNA Delivery Systems. *Biomacromolecules* **18**, 2231-2246 (2017).

14. H. Yin *et al.*, Non-viral vectors for gene-based therapy. *Nat Rev Genet* **15**, 541-555 (2014).

15. L. Buscail *et al.*, First-in-man phase 1 clinical trial of gene therapy for advanced pancreatic cancer: safety, biodistribution, and preliminary clinical findings. *Mol Ther* **23**, 779-789 (2015).

16. J. S. Suk *et al.*, Lung gene therapy with highly compacted DNA nanoparticles that overcome the mucus barrier. *J Control Release* **178**, 8-17 (2014).

17. H. Petersen *et al.*, Polyethylenimine-graft-Poly(ethylene glycol) Copolymers: Influence of Copolymer Block Structure on DNA Complexation and Biological Activities as Gene Delivery System. *Bioconjugate Chemistry* **13**, 845-854 (2002).

18. A. Zintchenko, A. Philipp, A. Dehshahri, E. Wagner, Simple modifications of branched PEI lead to highly efficient siRNA carriers with low toxicity. *Bioconjug Chem* **19**, 1448-1455 (2008).

19. B. P. Mead *et al.*, Targeted gene transfer to the brain via the delivery of brain-penetrating DNA nanoparticles with focused ultrasound. *J Control Release* **223**, 109-117 (2016).

20. Y. E. Seo, T. Bu, W. M. Saltzman, Nanomaterials for convection-enhanced delivery of agents to treat brain tumors. *Curr Opin Biomed Eng* **4**, 1-12 (2017).

21. E. V. van Gaal *et al.*, How to screen non-viral gene delivery systems in vitro? *J Control Release* **154**, 218-232 (2011).

22. D. G. Anderson *et al.*, A polymer library approach to suicide gene therapy for cancer. *Proc Natl Acad Sci U S A* **101**, 16028-16033 (2004).

23. S. Yamano, J. Dai, A. M. Moursi, Comparison of Transfection Efficiency of Nonviral Gene Transfer Reagents. *Molecular Biotechnology* **46**, 287-300 (2010).

24. M. Zanoni *et al.*, 3D tumor spheroid models for in vitro therapeutic screening: a systematic approach to enhance the biological relevance of data obtained. *Scientific Reports* **6**, 19103 (2016).

25. R. Edmondson, J. J. Broglie, A. F. Adcock, L. Yang, Three-dimensional cell culture systems and their applications in drug discovery and cell-based biosensors. *Assay Drug Dev Technol* **12**, 207-218 (2014).

26. K. Paunovska *et al.*, A Direct Comparison of in Vitro and in Vivo Nucleic Acid Delivery Mediated by Hundreds of Nanoparticles Reveals a Weak Correlation. *Nano Lett* **18**, 2148-2157 (2018).

27. E. Cukierman, R. Pankov, D. R. Stevens, K. M. Yamada, Taking cell-matrix adhesions to the third dimension. *Science* **294**, 1708-1712 (2001).

28. R. Sutherland, Cell and environment interactions in tumor microregions: the multicell spheroid model. *Science* **240**, 177-184 (1988).

29. D. Hambardzumyan, G. Bergers, Glioblastoma: Defining Tumor Niches. *Trends Cancer* **1**, 252-265 (2015).

30. H. Lu, M. H. Stenzel, Multicellular Tumor Spheroids (MCTS) as a 3D In Vitro Evaluation Tool of Nanoparticles. *Small* **14**, e1702858 (2018).

31. P. S. Thakuri, C. Liu, G. D. Luker, H. Tavana, Biomaterials-Based Approaches to Tumor Spheroid and Organoid Modeling. *Adv Healthc Mater* **7**, e1700980 (2018).

32. P. Mastorakos *et al.*, Biodegradable brain-penetrating DNA nanocomplexes and their use to treat malignant brain tumors. *J Control Release* **262**, 37-46 (2017).

33. C. W. Beh *et al.*, Direct interrogation of DNA content distribution in nanoparticles by a novel microfluidics-based single-particle analysis. *Nano Lett* **14**, 4729-4735 (2014).

34. K. S. Kopanska, Y. Alcheikh, R. Staneva, D. Vignjevic, T. Betz, Tensile Forces Originating from Cancer Spheroids Facilitate Tumor Invasion. *PLoS One* **11**, e0156442 (2016).

35. G. A. Duncan *et al.*, Microstructural alterations of sputum in cystic fibrosis lung disease. *JCI Insight* **1**, e88198 (2016).

36. V. R. Recinos *et al.*, Combination of intracranial temozolomide with intracranial carmustine improves survival when compared with either treatment alone in a rodent glioma model. *Neurosurgery* **66**, 530-537; discussion 537 (2010).

37. B. Tyler *et al.*, A thermal gel depot for local delivery of paclitaxel to treat experimental brain tumors in rats. *J Neurosurg* **113**, 210-217 (2010).

38. A. K. Vellimana *et al.*, Combination of paclitaxel thermal gel depot with temozolomide and radiotherapy significantly prolongs survival in an experimental rodent glioma model. *Journal of Neuro-Oncology* **111**, 229-236 (2013).

39. E. Song *et al.*, Surface chemistry governs cellular tropism of nanoparticles in the brain. *Nat Commun* **8**, 15322 (2017).

40. A. Greensted. (The Lab Book Pages, 2010).

41. E. V. van Gaal, R. S. Oosting, W. E. Hennink, D. J. Crommelin, E. Mastrobattista, Junk DNA enhances pEI-based non-viral gene delivery. *Int J Pharm* **390**, 76-83 (2010).

42. A. M. Ansari *et al.*, Cellular GFP Toxicity and Immunogenicity: Potential Confounders in in Vivo Cell Tracking Experiments. *Stem Cell Rev* **12**, 553-559 (2016).

43. A. Gambotto *et al.*, Immunogenicity of enhanced green fluorescent protein (EGFP) in BALB/c mice: identification of an H2-Kd-restricted CTL epitope. *Gene Ther* **7**, 2036-2040 (2000).

44. H. S. Liu, M. S. Jan, C. K. Chou, P. H. Chen, N. J. Ke, Is green fluorescent protein toxic to the living cells? *Biochem Biophys Res Commun* **260**, 712-717 (1999).

45. M. V. Matz *et al.*, Fluorescent proteins from nonbioluminescent Anthozoa species. *Nature Biotechnology* **17**, 969 (1999).

46. N. O. Alieva *et al.*, Diversity and evolution of coral fluorescent proteins. *PLoS One* **3**, e2680 (2008).

47. S. Pamujula *et al.*, Cellular delivery of PEGylated PLGA nanoparticles. *J Pharm Pharmacol* **64**, 61-67 (2012).

48. Y. Hu, J. Xie, Y. W. Tong, C. H. Wang, Effect of PEG conformation and particle size on the cellular uptake efficiency of nanoparticles with the HepG2 cells. *J Control Release* **118**, 7-17 (2007).

49. S. Mishra, P. Webster, M. E. Davis, PEGylation significantly affects cellular uptake and intracellular trafficking of non-viral gene delivery particles. *Eur J Cell Biol* **83**, 97-111 (2004).

50. S. Sant, P. A. Johnston, The production of 3D tumor spheroids for cancer drug discovery. *Drug Discov Today Technol* **23**, 27-36 (2017).

51. B. M. Baker, C. S. Chen, Deconstructing the third dimension: how 3D culture microenvironments alter cellular cues. *J Cell Sci* **125**, 3015-3024 (2012).

52. C. S. Shin, B. Kwak, B. Han, K. Park, Development of an in vitro 3D tumor model to study therapeutic efficiency of an anticancer drug. *Mol Pharm* **10**, 2167-2175 (2013).

53. C. J. Lovitt, T. B. Shelper, V. M. Avery, Miniaturized three-dimensional cancer model for drug evaluation. *Assay Drug Dev Technol* **11**, 435-448 (2013).

54. M. Oishi *et al.*, Enhanced growth inhibition of hepatic multicellular tumor spheroids by lactosylated poly(ethylene glycol)-siRNA conjugate formulated in PEGylated polyplexes. *ChemMedChem* **2**, 1290-1297 (2007).

55. B. S. Schuster, L. M. Ensign, D. B. Allan, J. S. Suk, J. Hanes, Particle tracking in drug and gene delivery research: State-of-the-art applications and methods. *Adv Drug Deliv Rev* **91**, 70-91 (2015).

56. A. Jahangiri *et al.*, Convection-enhanced delivery in glioblastoma: a review of preclinical and clinical studies. *J Neurosurg* **126**, 191-200 (2017).

57. J. Voges *et al.*, Clinical protocol. Liposomal gene therapy with the herpes simplex thymidine kinase gene/ganciclovir system for the treatment of glioblastoma multiforme. *Hum Gene Ther* **13**, 675-685 (2002).

58. J. Voges *et al.*, Imaging-guided convection-enhanced delivery and gene therapy of glioblastoma. *Ann Neurol* **54**, 479-487 (2003).

59. Takamasa Kayama, Takashi Yoshimoto, Shunichi Fujimoto, Yoshiharu Sakurai, Intratumoral oxygen pressure in malignant brain tumor. *Journal of Neurosurgery* **74**, 55-59 (1991).

60. A. Giese, R. Bjerkvig, M. E. Berens, M. Westphal, Cost of Migration: Invasion of Malignant Gliomas and Implications for Treatment. *Journal of Clinical Oncology* **21**, 1624-1636 (2003).

61. D. Hambardzumyan, D. H. Gutmann, H. Kettenmann, The role of microglia and macrophages in glioma maintenance and progression. *Nat Neurosci* **19**, 20-27 (2016).

62. N. D. Amoedo, J. P. Valencia, M. F. Rodrigues, A. Galina, F. D. Rumjanek, How does the metabolism of tumour cells differ from that of normal cells. *Biosci Rep* **33**, (2013).

63. S. Romero-Garcia, J. S. Lopez-Gonzalez, J. L. Baez-Viveros, D. Aguilar-Cazares, H. Prado-Garcia, Tumor cell metabolism: an integral view. *Cancer Biol Ther* **12**, 939-948 (2011).

64. I. Mellman, Y. Yarden, Endocytosis and cancer. *Cold Spring Harb Perspect Biol* **5**, a016949 (2013).

Chapter 3

Widespread gene transfer to brain tumors via biodegradable polymer-based DNA nanoparticles

Abstract

Biodegradable DNA nanoparticles offer a safe non-viral gene delivery platform devoid of adverse effects associated with synthetic nonbiodegradable systems. State-of-the-art biodegradable polymer, poly(β-amino ester) (PBAE), forms colloidally stable sub-100 nm DNA-brain penetrating nanoparticles (BPN) that sufficiently penetrate and transfect healthy and brain-tumor tissue. We have developed a series of PBAE polymer variants possessing different end-capping groups (Cx; x = 1-8) that have successfully shown DNA complexation and colloidal stability in artificial cerebrospinal fluid. Furthermore, nanoparticle characterization in three-dimensional multicellular *in vitro* tumor model, and *in vivo*, established a new BPN formulation, named BPN-C8, as the leading nanoparticle formulation for better widespread, yet safe, transgene expression in mice brain tissue after local administration. Moreover, for the first time we showed BPN-C8 achieving widespread tumor gene transfer in three highly aggressive orthotopic brain tumor models: GL261 (mouse glioblastoma), BT37 and CHLA-06 (AT/RT cell lines derived from pediatric human xenografts). Lastly, we successfully developed a method for cryo-protection of this BPN without compromising their penetrating properties nor their transgene expression efficiency. This provides a promising delivery platform for localized gene therapy of malignant brain tumors.

1. Introduction

As previously discussed, achieving widespread gene transfer in the brain parenchyma is crucial in order to experience complete cure or survival benefits when treating brain tumors via gene therapy platforms. Given this significant challenge, our group has focused on developing polymer-based DNA-loaded brain penetrating nanoparticles (BPN) possessing favorable physicochemical properties, including colloidal stability in physiological environments and *in vivo*. Importantly, we have previously demonstrated that synthetic BPNs, made with lead polymers tested in clinical trials, albeit not for brain, including polyethyleneimine (PEI) (*1-6*) and poly-L-lysine (PLL) (*7*), when possessing small particle diameters (<100 nm) and non-adhesive surface coatings with dense polyethylene glycol (PEG), can be locally administered via convection-enhanced delivery (CED) to provide widespread gene transfer in healthy brain tissues (*8, 9*). Furthermore, we recently reported that PEI-BPN with heavier PEG coatings, and the state-of-the-art biodegradable polymer-based poly(β-amino ester) (PBAE) BPN can also achieve widespread gene transfer in orthotopic brain tumors after CED (PEI-BPN studies shown in Chapter 2) (*10*). Encouragingly, PBAE BPN demonstrated significant anti-tumor efficacy in F98 rat glioblastoma and 9L rat gliosarcoma tumor models when carrying plasmids encoding for thymidine kinase and p53 gene, respectively, whereas PBAE unPEGylated nanoparticles (UPN) were unable to do so (*11*).

Anderson D. G., Lynn D. M., and Langer R. described the first synthesis and high-throughput screening from a large library of PBAE polymers variants, composed of ~2350 candidates, and confirmed their ability to achieve gene transfer in mammalian cell culture (*12*). Since then, a series of other PBAE generations have been reported in the literature as strong candidates for *in vitro* gene transfer in various cell types with potential use for *in vivo* applications (*13-19*). Here, we identified a few (up to eight) candidates that possess different terminal ends previously shown to provide excellent *in vitro* efficiency and sought to engineer and test BPN formulated based on these variants for widespread transgene expression in brain.

While two-dimensional (2D) monolayer cells, cultured on flat and rigid surfaces, have been widely used for screening DNA-loaded nanoparticles and other transfection reagents, i.e. viral vectors and lipofectamine, its limitations have been increasingly recognized (*20*). Although the time-honored 2D cell culture has proven to be a valuable method for cell-based studies, it has been reported the 2D *in vitro* and *in vivo* do not correlate *(20)*. In Chapter 2, we found that it is reverse-correlated. On the other hand, it has been shown that three-dimensional (3D) multicellular spheroids, represent more accurately the actual microenvironment where cells reside in tissues (*20*), which served as a reliable model to predict *in vivo* performances of DNA-loaded nanoparticles, confirmed in our previous PEI-BPN studies from Chapter 2. Here we thus formulated and thoroughly characterized BPN based on PBAE variants and test *in vitro* with 3D model and *in vivo* with healthy and tumor-bearing mice brain tissue. Lastly, we then formulated a "ready-to-use" lyophilized version of the lead BPN candidate for long-term storage and pertinent clinical applications.

2. Materials and Methods

2.1 Polymer synthesis

For the PBAE backbone polymer, monomers 1,4-butanediol diacrylate and 4-amino-1-butanol were purchased from Alfa Aesar (Ward Hill, MA). For the end-capping groups, **C1** (1,3-diaminopropane) and **C2** (2,2-dimethyl-1,3-propanediamine) were purchased from Sigma-Aldrich (St. Louis, MO); **C3** (N-(3-aminopropyl)pyrrolidine) was purchased from Acros Organics (New Jersey); **C4** (1-(3-aminopropyl)-4-methylpiperazine) was purchased from Alfa Aesar; **C5** (2-(3-aminopropylamino) ethanol) was purchased from Oakwood Chemical (West Columbia, SC); **C6** (N,N-bis(2-hydroxyethyl)ethylenediamine) was purchased from Alfa Aesar; **C7** (N-(3-aminopropyl)diethanolamine) and **C8** (1,11-diamino-3,6,9-trioxaundecane) were purchased from Tokyo Chemical Industry (Cambridge, MA). For the PEGylation reaction, methoxy-PEG-succinimidyl succinate from JenKem Technology (Plano, TX). Solvents were purchased as

follows: ethyl ether anhydrous from Fischer Scientific (Pittsburgh, PA); dimethyl sulfoxide anhydrous (DMSO) and tetrahydrofuran (THF) from Sigma-Aldrich.

Following an in-depth literature search (*13, 14, 16, 19, 21-24*), we established a series of leading PBAE polymers previously shown to provide efficient *in vitro* gene transfer (Figure 3.1). PBAE polymers were synthesized by a two-step Michael addition reaction, as previously reported (*24, 25*). First, 1,4-butanediol diacrylate and 4-amino-1-butanol were reacted at a 1.1:1 molar ratio at 90 °C for 24 hours to synthesize high–molecular-weight (MW) uncapped PBAE polymer (6.0–6.5 kDa). Polymers were then precipitated in cold ether three times to remove any unreacted species, dried under vacuum, and lyophilized. The molecular mass of 6.0–6.5 kDa was estimated using NMR, assuming two end acrylate groups per polymer and characterized by gel permeation chromatography (GPC) (see Mastorakos et al. 10.1073/pnas.1502281112, PNAS supplementary materials for NMR and GPC details) (*24*). For capping of the end acrylate groups, PBAE backbone polymer was dissolved in THF at 100 mg/mL and 30 molar equivalents of one of C1–C8 capping groups was added (to ensure end capping rather than further propagation). The reactions occurred while stirring at room temperature for 4–5 hours. The end-capped PBAE polymers were retrieved by precipitation in cold ether to remove unreacted groups, dried under vacuum, and lyophilized. Purity and complete end capping were confirmed by the absence of the acrylate proton peaks in the NMR spectrum (data not shown) (*24*).

For the synthesis of PEGylated PBAE polymer (PEG-PBAE), a three-step reaction scheme was used. First, a PBAE polymer possessing lower MW was synthesized by reacting 1,4-butanediol diacrylates and 4-amino-1-butanol at a 1.2:1 molar ratio. Based on NMR analysis, the molecular mass was estimated to be 3.8–4.2 kDa, assuming two end acrylate groups per polymer. The low-MW PBAE polymer was then capped with C1 as described earlier, and the end capping was confirmed by NMR. Subsequently, methoxy-PEG succinimidyl succinates were reacted with the two terminal primary amine groups at both ends of the C1-capped PBAE

polymer chain. To do this, we transferred the resulting PBAE-C1 polymer and 2.05 molar equivalents of 5 kDa methoxy-PEG-succinimidyl succinate to a glass vial, vacuumed, and purged with nitrogen. The mixture of reactants was dissolved in THF and reacted while stirring at room temperature overnight. The final PEG-PBAE polymer product was precipitated and washed with cold ether three times, dried under vacuum, and lyophilized. PEG conjugation was confirmed with NMR. Of note, the lower-MW PBAE polymer was used for the synthesis of PEG-PBAE (at a PEG-to-PBAE molar ratio of 2:1) to increase the PEG-to-PBAE weight-to-weight (wt/wt) ratio of the individual PEG-PBAE polymers and, thus, achieve a higher PEG content when particles are formulated at a fixed amount of PBAE polymer. All polymers were dissolved in DMSO at 100 mg/mL and stored at −20 °C for further use. Previous publications from our group used PBAE-C5 as a core polymer for the formulation of BPN (*10, 11, 24*), however, this is the first time we test all eight variants in the brain for gene transfer in malignant tumors followed by intracranial administration.

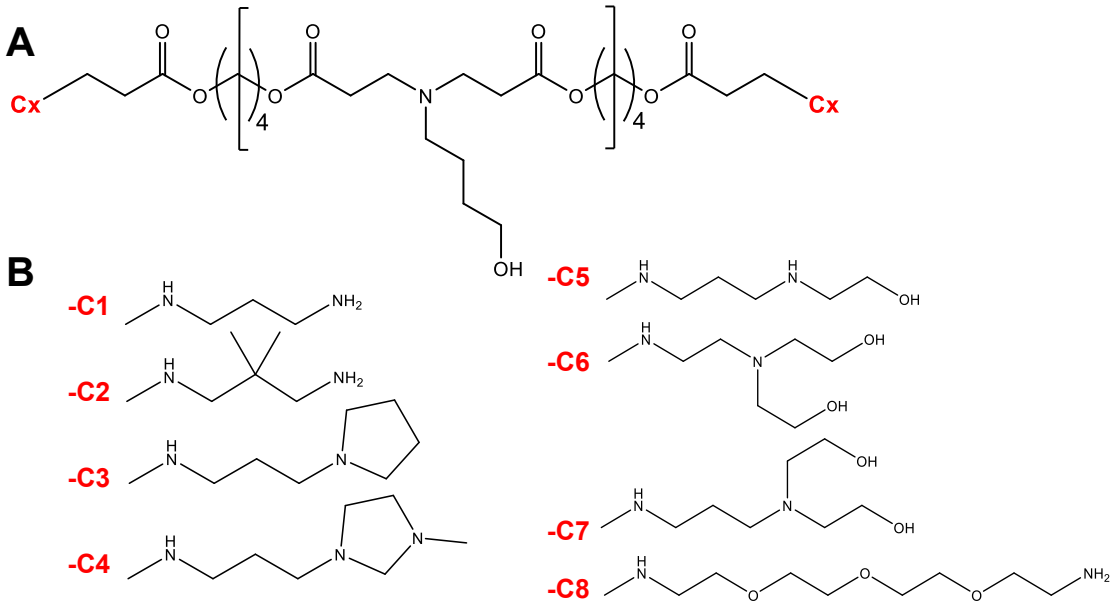

Figure 3.1: Poly(β-amino esters) (PBAE) polymer variants. (A) Chemical structure of the polymer backbone. **(B)** Chemical structure of the different end-capping groups used to synthesize PBEA polymer variants (Cx; x = 1-8).

2.2 Nanoparticle formulation

The luciferase-expressing plasmids driven by the short-acting cytomegalovirus (CMV) promoter (i.e. pd1GL3-RL) was a kind gift from Professor Alexander M. Klibanov (M.I.T). The ZsGreen-expressing plasmid driven by the CMV promoter was purchased from Clontech Laboratories Inc. (Mountainview, CA). Plasmids were propagated and purified, as previously described (*11, 26*). Briefly, plasmids were transformed into *E. coli* DH5α competent bacterial cells using a heat shock method, and following the bacterial expansion in LB media, plasmids were purified using EndoFree Plasmid Giga Kit (QIAGEN, Valencia, CA), as per manufacturer's protocol.

PBAE UPN were formulated and characterized as previously reported (*10, 11, 21*). BPN were formulated using a protocol we have recently established (*11*). Briefly, 5 volumes of plasmid DNA (0.1 mg/ml) were added drop-wise to 1 volume of polymer solution, consisting of a mixture of PBAE and PEG-PBAE at a w/w ratio of 2:3 based on PBAE mass and at a PBAE to plasmid DNA ratio of 60:1 w/w. Using a 0.1 M hydrochloric acid solution, both the DNA and the polymer solutions were adjusted to pH 6.0. Following formulation, nanoparticles were washed with 3 volumes of ultrapure water, and concentrated to 1 mg/ml of plasmid DNA using Amicon® Ultra Centrifugal Filters (100,000 MWCO, Millipore Corp., Billerica, MA) as measured using the Quant-iT™ PicoGreen® dsDNA Assay Kit (Life Technologies, Grand Island, NY). The hydrodynamic diameters as well as polydispersity index (PDI) and ζ-potentials of UPN and BPN-Cx were measured by dynamic light scattering (DLS; in ultrapure water) and laser Doppler anemometry (in 10 mM NaCl solution at pH 7.0), respectively, using a Nanosizer ZS90 (Malvern Instruments, Southborough, MA). The size and morphology of nanoparticles were also confirmed by transmission electron microscopy (TEM) (Hitachi H7600, Japan). The DNA complexation was confirmed by conventional agarose gel-based electrophoretic analysis. Colloidal stability was assessed by monitoring the change in hydrodynamic diameters and PDI in artificial cerebrospinal fluid (aCSF) (Harvard Apparatus, Holliston, MA) at 37 °C.

2.3 Cell culture

Highly aggressive mice GL261 glioblastoma cells were provided by Dr. Kannan Rangaramanujam. Cells were cultured in Roswell Park Memorial Institute (RPMI) 1640 Medium purchased from ThermoFischer Scientific (Waltham, MA) supplemented with 1% L-Glutamine, 10% heat-inactivated fetal bovine serum (FBS) and 1% penicillin/streptomycin from Invitrogen Corp. (Carlsbad, CA). Upon reaching the confluent state, the monolayers were treated with trypsin and the dispersed cells were transferred into new culture flasks. The spheroid media for GL261 cells was prepared by dissolving autoclaved methylcellulose from Sigma-Aldrich at 2.4% (w/v) in preheated (60 °C) serum-free RPMI followed by dilution with an equivolume of RPMI supplemented with 10% FBS and an overnight stirring at 4 °C. The solution was then centrifuged at 5,000 x g for 2 hours at 4 °C to precipitate undissolved methylcellulose and the supernatant stored at 4 °C until use. The *in vitro* studies in three-dimensional (3D) multicellular spheroids and *in vivo* studies were conducted when GL261 cells reached 70% - 80% confluency in the flask.

Highly aggressive pediatric BT37 and CHLA-06 AT/RT cells, derived from human xenografts, were provided by Dr. Eric H. Raabe (*27*). BT37 cells were cultured in RPMI-1640 medium containing 1% penicillin/streptomycin, and 20% FBS. CHLA-06 cells were initially cultured as neurospheres in modified Neurobasal medium consisting of 1:1 DMEM:F12 containing 15 mM HEPES purchased from StemCell Technologies (Cambridge, MA), 110 mg/L sodium pyruvate from ThermoFischer Scientific, 1.2 g/L sodium bicarbonate, B27 supplement from Gibco (Grand Island, NY), 20 ng/mL epidermal growth factor from Peprotech, Inc. (Rocky Hill, NJ), 20 ng/mL basic fibroblast growth factor (Peprotech), and 25 µg/ml gentamicin (Gibco). Gentamicin was removed after the first 2 weeks of culture. For BT37, upon reaching the confluent state, the monolayers were treated with trypsin and the dispersed cells were transferred into new culture flasks. For CHLA-06 suspension cells, the passaging was at ratio of 1:2–3 with 25% (v/v) conditioned medium in the new flask every 4 to 5 days. The cultures were incubated at 37°C in

a humidified atmosphere of 5% CO2. Both AT/RT cell lines used in this manuscript were previously authenticated to be human and did not match the short tandem repeat profile of any other cell line in the established databases (ATCC, DSMZ, and JCRB) (*27*).

2.3.1 Cellular uptake

Cells were seeded onto 6-well plates at an initial density of 200,000 cells/well and grown overnight at 37 °C. Cells were treated with the various BPN carrying Cy5-labeled plasmids (5 μg DNA/well) and after 5 hours of incubation, the media was removed. Cells were then thoroughly washed with 1X phosphate buffered saline (PBS) and trypsinized. Flow cytometry was conducted to quantify the cellular uptake of DNA-NP using a Sony Cell Sorter SH800 (Sony, San Jose, CA), followed by data analyzed with a FlowJo software (FlowJo LLC, Ashland, OR).

2.3.2 Luciferase assay

Cells were seeded at an initial density of 5,000 cells/well onto 96-well plates and grown overnight at 37 °C. Cells were then treated with the various BPN carrying luciferase-expressing plasmids (i.e. pd1GL3-RL) at a plasmid concentration of 0.5 μg/well, and the culture media was replaced with fresh media 5 hours after the incubation. After 48 hours of additional incubation, media was removed and 100 μl of 1X Reporter Lysis Buffer purchased from Promega (Madison, WI) was added. Subsequently, cells were subjected to three freeze-and-thaw cycles to achieve complete lysis followed by the collection of supernatants by centrifugation. Luciferase activity was measured in relative light units (RLU) using a standard Luciferase Assay Kit (Promega) and a 20/20n luminometer (Turner Biosystems, Sunnyvale, CA). The RLU values were normalized to the total protein content measured by a Bicinchoninic Acid (BCA) Protein Assay Kit (Thermo scientific).

2.3.3 Transgene expression in 3D multicellular spheroids

3D multicellular spheroids were established by the hanging-drop method as previously described in Chapter 2. Briefly, for each spheroid, 5,000 GL261 cells were suspended in 20 μL of spheroid media on the lid of a petri-dish. Spheroids were then grown upside down by

covering a PBS-filled/moisturized petri-dish with the cell-seeded lid for 2 days. Then, spheroids were transferred onto a sterile U-bottom 96-well plate (CELLSTAR®) (Sigma-Aldrich, St. Louis, MO) along with RPMI 1640 Medium (ThermoFischer Scientific, Waltham, MA) and incubated at 37ºC for 48 hours prior treatment. Subsequently, GL261 spheroids were treated with the various BPN formulations carrying ZsGreen-expressing plasmids (1 µg plasmids/spheroid). After 48 hours of additional incubation, the spheroids were transferred on to poly-d-lysine coated 35 mm glass bottom dishes (MatTek Corp., Ashland, MA). Fluorescence images were then captured using an LSM 710 confocal microscope (Carl Zeiss; Hertfordshire, UK) under 10X magnification and analyzed for spheroid area-normalized mean fluorescence intensity using an ImageJ software (NIH, Bethesda, MD).

2.4 Animal studies

Female C57BL/6 mice, 6–8-week-old, were used for the assessment of *in vivo* gene transfer of UPN and the various BPN formulations in healthy and GL261 tumor tissue. Female NSG mice, 6-8-week-old, were used for assessment of in vivo gene transfer of BPN-C8 in BT37 and CHLA-06 tumor tissue. All animals were treated in accordance with the policies and guidelines of the Johns Hopkins University Animal Care and Use Committee.

2.4.1 Orthotopic tumor inoculations

Surgical procedures were performed using standard sterile surgical techniques. Intracranial xenografts were produced in anesthetized animals using a mixture of 75 mg/kg ketamine and 7.5 mg/kg xylazine, as previously described (*28-30*). For GL261 tumors, a midline scalp incision was made to expose the coronal and sagittal sutures and a burr whole was drilled 2 mm lateral to the sagittal suture and 0.5 mm anterior to the bregma. Then 100,000 GL261 viable cells were administered in 2 µL of RPMI 1640 Medium over 2 minutes at a depth of 3.5 mm using a Neuros syringe (Hamilton, Reno, NV) mounted on an ultra-precise small-animal stereotactic frame (Stoelting Co., Wood Dale, IL). For BT37 and CHLA-06 human xenografts, injection guide holes were produced by an 18-gauge beveled needle from, where 100,000

viable cells were administered in 5 µl of respective growth medium into the right striatum 2 mm lateral to the sagittal suture and 3 mm anterior to the bregma at a depth of 3 mm using a Neuros syringe mounted on an ultra-precise small-animal stereotactic frame. Following the tumor cell inoculation, the skin was sealed with a 9 mm Autoclip Applier using stainless steel wound clips (Braintree Scientific Inc., Braintree, MA).

2.4.2 Intracranial administration – CED

Various nanoparticles carrying ZsGreen- or luciferase-expressing plasmids were intracranially administered via CED, as previously described (*9, 10*). Briefly, a Neuros syringe connected to a 33-gauge needle was filled with 2 µL of nanoparticle solution at a plasmid concentration of 0.5 mg/mL and lowered to a depth of 3.0 or 2.5 mm, for healthy or orthotopic tumor-bearing mice brain, targeting the striatum or the tumor core, respectively. Note that for safety analysis, sterile medical-grade normal saline was administered as a control. The solution was then infused at a rate of 0.22 µL/min as controlled by a Chemyx Nanojet Injector Module (Chemyx, Stafford, TX). Following the administration, the skin was sealed using biodegradable sutures (Polysorb™ Braided Absorbable Sutures 5–0) and bacitracin was applied.

2.4.3 Distribution of transgene expression

To assess the distribution of transgene expression, brain tissues of mice that received UPN or various BPN carrying ZsGreen-expressing plasmids were harvested 48 hours after the administration and subsequently fixed with 4% formaldehyde. Tissues were then sectioned using a Leica CM 1905 cryostat into 50 µm coronal slices at ± 3 mm of the infusion plane in striatum or until the tumor tissue was no longer visible. Slices of orthotopic tumor tissues were stained with DAPI (Molecular Probes, Eugene, OR) to visualize tumor cell nuclei. All fluorescence images were taken using an LSM 710 confocal microscope under 5X magnification. We carefully optimized the settings to avoid background fluorescence based on the microscopy of untreated control rat brains. The volume of transgene expression was quantified using a custom-made MATLAB script that subtracted background fluorescence by

Otsu's method of thresholding (*31, 32*). The area of transgene expression in each slice was integrated to calculate the total volume of transgene expression. To reconstruct 3D-rendered images of volumetric transgene expression, we stacked and aligned the acquired images using Metamorph ® Microscopy Automation & Image Analysis Software (Molecular Devices, CA). Finally, we used an Imaris Software (Bitplane, CT) to create 3D isosurfaces of the reconstructed images.

To quantify the overall level of transgene expression, we treated mice using the identical dosing method applied to the distribution study but with UPN or various BPN carrying luciferase-expressing plasmids (i.e. pd1GL3-RL). Brains were harvested 72 hours after the administration and subjected to homogenate-based luciferase assay using a standard Luciferase Assay Kit and a 20/20n luminometer. The RLU values were normalized to the total protein content measured by BCA protein assay.

2.4.4 Histological analysis and safety profile

Animals were sacrificed 3 days following administration and the harvested brains were fixed in 4% formaldehyde, processed, sectioned and stained with hematoxylin and eosin (H&E) by the Johns Hopkins Reference Histology Laboratory. The point of infusion was identified by the tissue cavity imparted by the needle and the region immediately adjacent was imaged and evaluated. Blind histopathological analysis was performed by a board-certified neuropathologist and tissues were scored from 0–3 for indications of inflammation and hemorrhage (0: no inflammation/hemorrhage, 1: mild, 2: moderate, 3: severe).

2.5 Lyophilization of BPN

For lyophilized nanoparticle formation and evaluation, BPN were initially formed as described above. Subsequently, sucrose (OPS Diagnostics, Lebanon, NJ) was added as a cryoprotectant to a final concentration of 30 mg/mL, diluting BPN 2-fold. BPN were frozen in dry-ice and lyophilized overnight. Lyophilized BPN were stored at -20 °C until use and were then

reconstituted in sterile ultrapure water and used at the same concentration as freshly prepared BPN.

2.6 Statistical Analysis

Statistical analysis between two groups was conducted using a two-tailed Student's t-test assuming unequal variances. If multiple comparisons were involved, one-way analysis of variance (ANOVA), followed by Sidak's multiple comparisons test, was employed, using GraphPad Software (GraphPad Software Inc., La Jolla, CA). Differences were determined to be statistically significant at $p < 0.05$. Values are presented as mean ± standard error of the mean (SEM).

3. Results

3.1 Physicochemical characterization of UPN and BPN

We complexed DNA into nanoparticles with one of the PBAE polymer variants possessing different end-capping groups (Cx; x = 1-8; Figure 3.1) consisting of a mixture of PBAE and PEG-PBAE at a w/w ratio of 2:3 based on PBAE mass and at a PBAE to plasmid DNA ratio of 60:1 w/w to form BPN. Hydrodynamic diameter and PDI were measured by DLS in ultrapure water. The ζ -potential was measured by laser Doppler anemometry in 10mM NaCl at pH 7.0. At least 3 independent experiments were performed for this analysis. Table 3.1 shows that all BPN-Cx, possessed a hydrodynamic diameter of ~60 nm, a low PDI ~0.1, and near neutral surface charge as indicated by ζ-potential ~3-4 mV when freshly made in ultrapure water; whereas BPN-C6 possessed a higher PDI of 0.2 and a highly cationic surface charge of 14.8 ± 1.2 mV. For control purposes, UPN were formulated and characterized as previously reported (*10, 11, 21*). Figure 3.2 shows that UPN possessed a hydrodynamic diameter of 130 ± 11 nm and highly cationic surface charge of 26 ± 6.5 mV when freshly made in ultrapure water.

Table 3.1: Physicochemical properties of different BPN formulations.

BPN[a]	Hydrodynamic diameter ± SEM (nm)[b]	PDI[b]	ζ-potential ± SEM (mV)[c]	Hydrodynamic diameter ± SEM at 4 hours in aCSF (nm)[d]	PDI at 4 hours in aCSF[d]
C1	60 ± 5	0.09	3.6 ± 2.6	79 ± 10	0.28
C2	60 ± 2	0.09	2.8 ± 2.8	64 ± 3	0.40
C3	67 ± 1	0.07	4.3 ± 2.3	74 ± 21	0.30
C4	58 ± 5	0.13	6.5 ± 0.5	62 ± 1	0.28
C5	62 ± 2	0.09	4.2 ± 0.7	80 ± 5	0.20
C6	65 ± 9	0.20	14.8 ± 1.2	271 ± 14	0.41
C7	63 ± 2	0.07	1.7 ± 0.9	67 ± 8	0.38
C8	60 ± 1	0.07	4.5 ± 0.8	73 ± 2	0.04

[a] Each BPN was formulated with one of the core PBAE polymer variants possessing different end-capping groups (Cx; x = 1-8; Figure 3.1)

[b] Hydrodynamic diameter and polydispersity index (PDI) were measured by dynamic light scattering (DLS) in ultrapure water. Mean ± SEM (n ≥ 3).

[c] ζ-potential was measured by laser Doppler anemometry in 10mM NaCl at pH 7.0. Mean ± SEM (n ≥ 3).

[d] Hydrodynamic diameter and PDI were measured by DLS following a 4-hour incubation in aCSF at 37ºC.

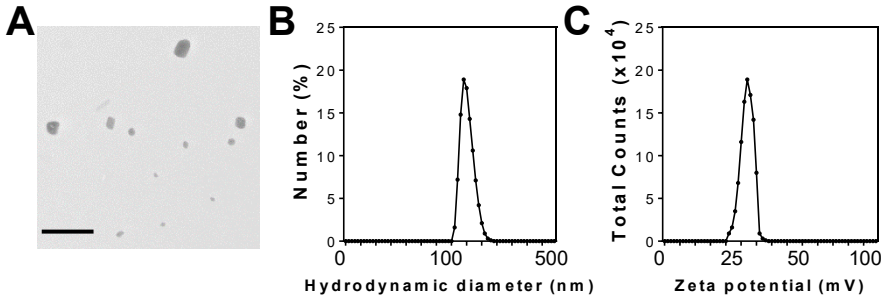

Figure 3.2: Physicochemical characterization of UPN. (A) Transmission electron micrograph of fresh UPN formulated in ultrapure water. Scale bar = 800 nm. **(B)** Hydrodynamic diameter was measured by dynamic light scattering (DLS) in ultrapure water (n ≥ 3). **(C)** ζ-potential was measured by laser Doppler anemometry in 10 mM NaCl at pH 7.0 (n ≥ 3).

The particle morphology was confirmed by TEM to be ~60 nm spheres regardless of end-capping groups (only BPN-C6 and BPN-C8 are shown in Figure 3.3A), consistent with the measured hydrodynamic diameters (Table 3.1). We then verified robust DNA compaction in all eight BPN compared to free plasmid via a conventional agarose-gel migration assay (Figure 3.3B). Lastly, we assessed the hydrodynamic diameters of the various BPN following a 4-hour

incubation in aCSF at 37ºC to predict potential alteration of particle properties in the physiological brain environment. We found most BPN formulations slightly increased their hydrodynamic diameters in aCSF to ~70-80 nm and their PDI to ~0.3 (Table 3.1). Notably, BPN-C8, although with slight increase, retained the diameter for up to 5 hours at 73 ± 2 nm and maintained a very low PDI of 0.04, whereas BPN-C6 incremented to a size of 271 ± 14 nm and showed a high PDI of 0.41 (Figure 3.3C). This suggests that BPN-C6 would be unlikely to efficiently penetrate brain tissues due to large particle size as well as positively charged particle surfaces.

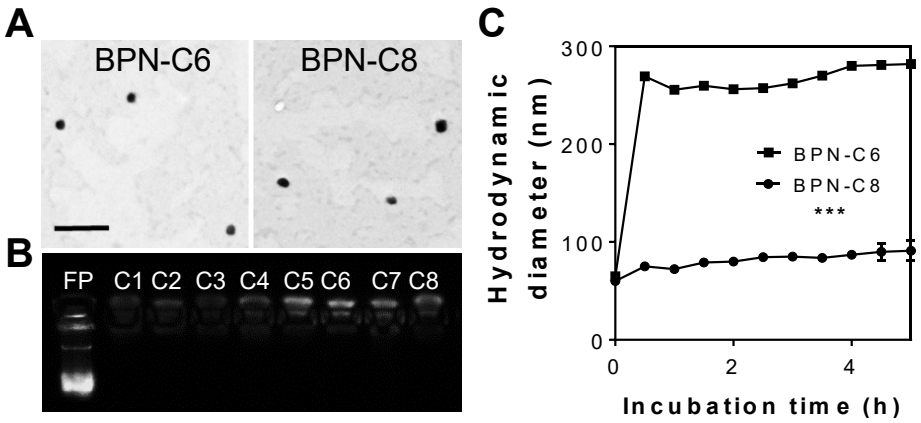

Figure 3.3: Physicochemical characterization of BPN formulations. (A) Transmission electron micrographs of BPN-C6 (left) and BPN-C8 (right). Scale bar = 400 nm. **(B)** Gel electrophoretic analysis demonstrating complexation of plasmids by different BPN formulations (FP = free plasmid; BPN-Cx; x = 1 - 8). **(C)** Colloidal stability of BPN-C6 and BPN-C8 in aCSF at 37°C over 5 hours, measured by DLS. The difference is statistically significant as indicated (***$p < 0.001$).

3.2 Transgene expression in healthy mice brains

UPN and various BPN carrying ZsGreen-expressing plasmids were administered into the mice striatum via CED that has been clinically applied to enhance the therapeutic distribution within brain by creating a continuous pressure-driven bulk flow (*31, 33*). Transgene expression was then assessed 48 hours after the treatment. The 3D reconstruction of confocal images of serial coronal sections of rat brains revealed enhanced volumes of transgene expression when mice were treated with BPN-C5 and BPN-C8 (Figure 3.4A). In agreement with our previous observation (*10*), the transgene expression mediated by UPN was confined to the site of

administration (image not shown) despite the pressure gradient provided by CED, giving a volume of transgene expression of 0.6 ± 0.2 mm^3. Most BPN variants, except for BPN-C6 and BPN-C7, exhibited significantly greater volumetric distribution of transgene expression compared to UPN (Figure 3.4B). Notably, BPN-C8 and BPN-C5 showed the two highest values for distribution of transgene expression, 7.2 ± 0.4 mm^3 and 5.9 ± 1.2 mm^3, respectively. Importantly, BPN-C8 roughly doubled the transfected volume on average in the mice striatum compared to BPN-C6 (3.1 ± 1.0 mm^3; $p < 0.05$; Figure 3.4B).

In parallel, we quantitatively determined the overall levels of transgene expression mediated by CED of UPN and the various BPN carrying luciferase-expressing plasmids, using a homogenate-based luciferase assay. BPN-C8 exhibited the highest levels of transgene expression (134,813 ± 23,262 RLU/mg of protein), with ~600-fold greater luciferase activity in comparison to UPN (219 ± 26 RLU/mg of protein) (Figure 3.4C). Furthermore, BPN-C8 exhibited statistically significant improvements ($p < 0.05$) with ~1.8-fold greater luciferase activity in comparison to BPN-C5, which was the next variant with the highest level of transgene expression (74,003 ± 13,969 RLU/mg of protein; ~330-fold greater than UPN). The findings here suggest that the unique ability of BPN-C8 to further increase the volumetric distribution of transgene expression over our previously reported BPN-C5.

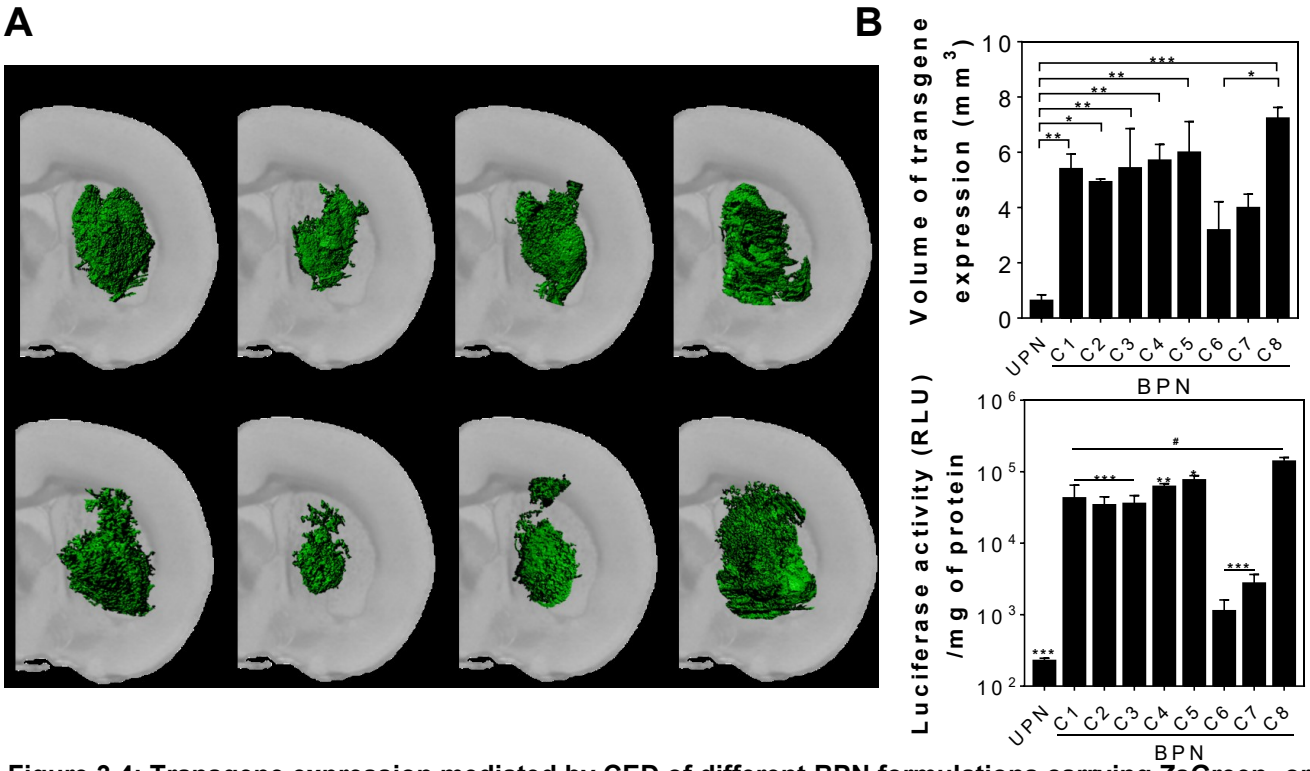

Figure 3.4: Transgene expression mediated by CED of different BPN formulations carrying ZsGreen- or luciferase-expressing plasmids in healthy mouse brain tissues. (A) Representative isosurface 3D images depicting volumetric distribution of ZsGreen reporter transgene expression (green) in healthy mice brains 48 hours after the treatment carrying, obtained by stacking multiple sequential confocal images. Scale bar = 1 mm. **(B)** Volume of ZsGreen transgene expression (n ≥ 6 mice). UPN denotes an un-PEGylated nanoparticle control. **(C)** Overall level of luciferase transgene expression (n ≥ 6 mice). Differences are statistically significant compared to BPN-C8 as indicated (*p < 0.05; **p < 0.01; ***p < 0.001). All BPN formulations exhibit statistically significant differences compared to UPN as indicated ($^{\#}p$ < 0.05).

3.3 Histopathological analysis and safety profile

To demonstrate the safety of PBAE-based nanoparticles followed by intracranial administration by CED, we compared the toxicity of UPN, BPN-C6, and BPN-C8 to medical-grade normal saline by histology safety profile in the mice striatum. Followed 3 days from the nanoparticle administration, the average toxicity scores of the brain tissues for UPN and both BPN were comparable to those of normal saline-treated controls (Figure 3.5), with an average score of ~1.5-2 for hemorrhage and ~0.5-1.5 for inflammation, suggesting that they were well-tolerated at the dose administered (0.5 mg/mL, 2 µL). Notably, the inflammation score increased with the respective volume of distribution in the brain (BPN-C8 > BPN-C6 > UPN). Importantly,

regardless of the gene vector type, inflammatory and hemorrhagic changes were confined around the injection site and did not propagate throughout the brain tissue.

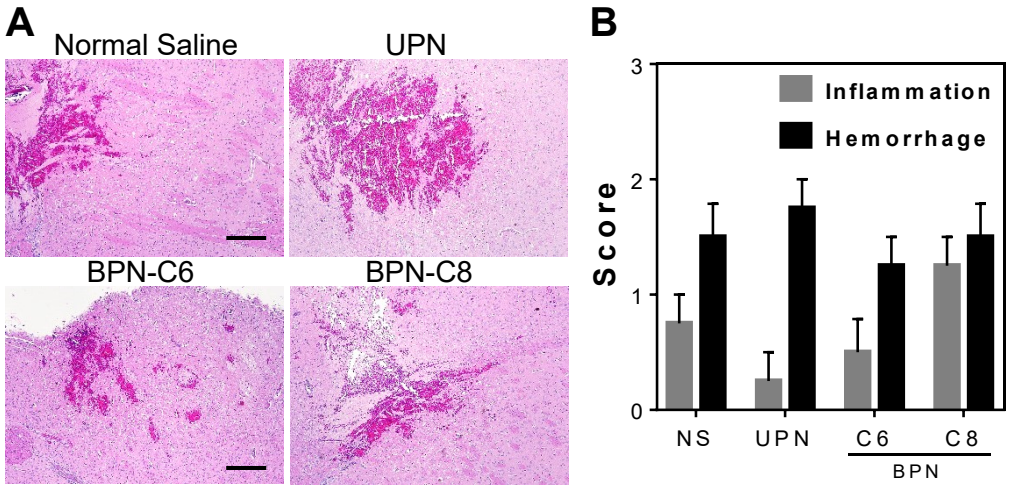

Figure 3.5: Histopathological analysis and safety profile of different BPN formulations in comparison to UPN following intracranial administration by CED. **(A)** Representative images showing H&E staining at the infusion site in healthy mouse brain tissue 3 days after nanoparticle administration (40X magnitude). Normal saline was infused as a control. Scale bar = 100 µm. **(B)** Inflammation and hemorrhage in healthy brain tissues were scored by a board-certified neuropathologist using a custom scale (0: no inflammation/hemorrhage; 1: mild; 2: moderate; 3: severe).

3.4 Transgene expression in GL261 tumor cells

We have previously confirmed that *in vitro* screening of gene vectors in two-dimensional (2D) culture is not accurate to predict *in vivo* gene transfer in the brain (Chapter 2). Despite this limitation, we assessed *in vitro* cellular uptake and transfection efficiency of the various BPN carrying Cy5-labeled and unlabeled luciferase-expressing plasmids, respectively, using a GL261-based 2D cell culture. As expected from our previous studies, there was no clear difference between the cellular uptake/mean intensity and the transfection efficiency of the eight BPN variants (Figure 3.6). To this end, we constructed a 3D tumor-spheroid model with GL261 cells and assessed the transgene expression of the various BPN carrying ZsGreen-expressing plasmids. As shown by representative confocal images (Figure 3.7A), four BPN (C1, C3, C5, and C8) exhibited greater levels of transgene expression compared to the other four variants (C2, C4, C6, and C7). Among the top four variants, BPN-C8 > BPN-C5 > BPN-C3 > BPN-C1.

Quantitatively, BPN-C8 showed significantly greater level of transgene expression (11.6 ± 1.7 a.u.), as measured by mean fluorescence intensity, compared to BPN-C1 (7.2 ± 0.9 a.u.; $p < 0.05$), BPN-C2 (3.7 ± 0.3 a.u.; $p < 0.001$), BPN-C4 (6.3 ± 0.6 a.u.; $p < 0.01$), BPN-C6 (3.3 ± 1.6 a.u.; $p < 0.001$), BPN-C7 (4.8 ± 0.9 a.u.; $p < 0.001$) (Figure 3.7B). This is also in agreement with the volume of transgene expression seen *in vivo*, which suggests the unique ability of BPN-C8 to further increase the volumetric distribution of transgene expression over our previously reported BPN-C5, and the poor gene transfer of BPN-C6.

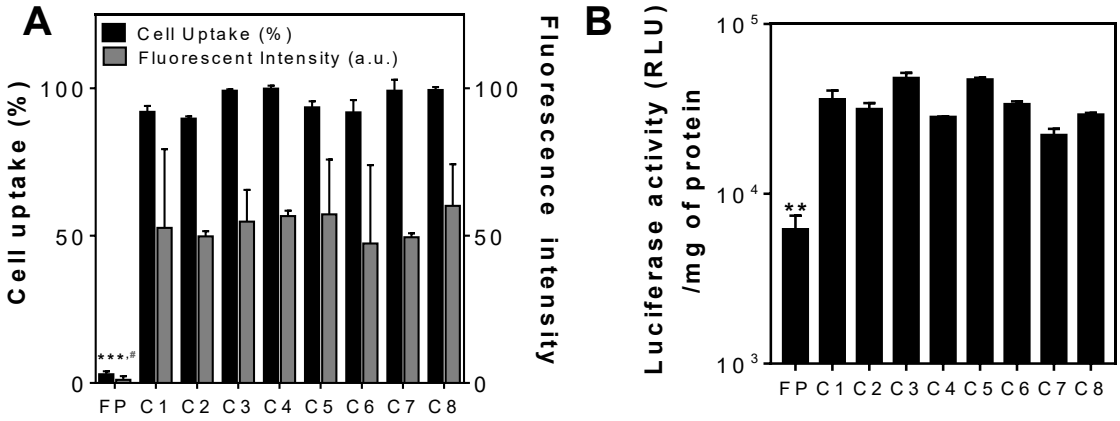

Figure 3.6: Cell uptake and transfection of BPN candidates in 2D cell cultures. (A) Flow cytometric analysis of percentage cell uptake and median fluorescence intensity (i.e. degree of cell uptake per cell) 5 hours after treatment with BPN candidates carrying ZsGreen-expressing plasmids or a respective carrier-free plasmid (FP) control. **(B)** *In vitro* luciferase transgene expression 48 hours after treatment with BPN candidates carrying luciferase-expressing plasmids or a respective FP control. The differences between all BPN candidates and respective FP controls are statistically significant ($^{\#}p < 0.05$; $^{**}p < 0.01$; $^{***}p < 0.001$).

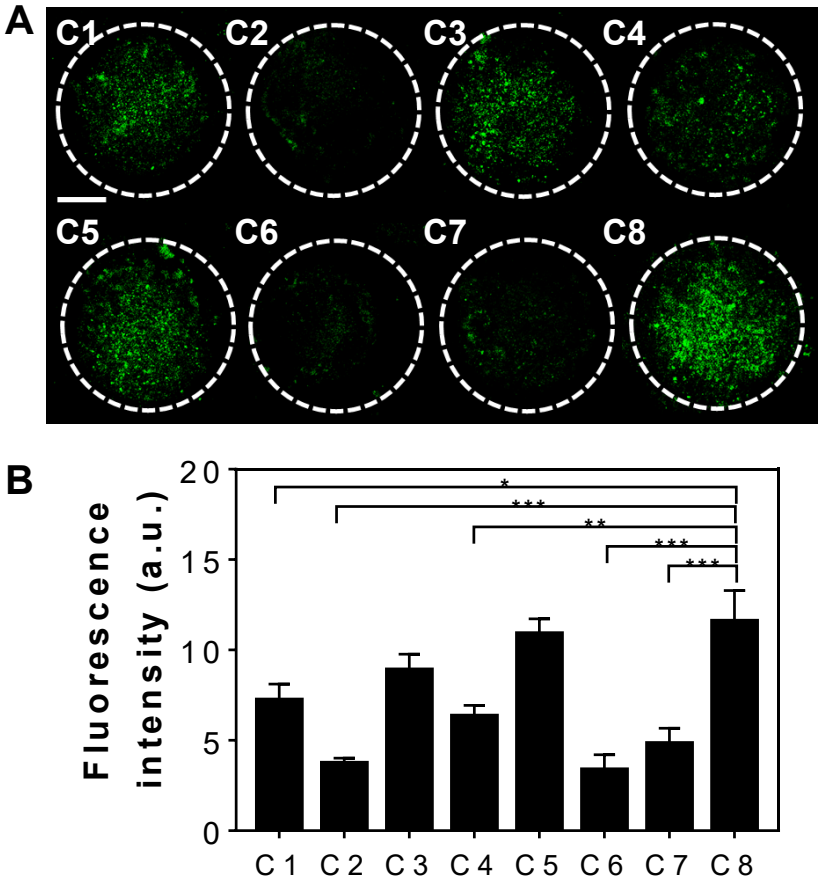

Figure 3.7: Transgene expression by BPN formulations in GL261-based 3D spheroids. (A) Representative reporter transgene expression (green) by BPN carrying ZsGreen-expressing plasmids 48 hours after the treatment. Scale bar = 250 μm. **(B)** Quantification of ZsGreen transgene expression within the spheroids. Differences are statistically significant as indicated (*$p < 0.05$; **$p < 0.01$; ***$p < 0.001$).

3.5 Transgene expression in orthotopic brain tumors

The Gl261 tumor is one of the few available murine glioma models. Originally this tumor was induced originally by intracranial injection of 3-methylcholantrene into C57BL/6 mice and propagated in vivo by transplanting small tumor pieces on its syngeneic host (*34*). This tumor model was used in many immune therapeutic and gene therapeutic investigations, and it is included among the aggressively growing tumors, compared to 9L and F98 (previous work). In contrast, the C6 rat glioma and the 4C8 mouse glioma models are much less aggressive (*35*). Furthermore, Gl261 cells and the 'original' brain tumor contain several molecular biological

alterations characteristic of human gliomas, such as p53 and K-RAS mutations, and it is only moderately immunogenic (*36*).

We next evaluated *in vivo* gene transfer efficacy of BPN-C6 and BPN-C8 carrying ZsGreen-expressing plasmids in the orthotopic model GL261, following CED. The CED experiment was conducted 12 days after the inoculation. BPN-C6 was used as a negative control. As shown by representative 3D-reconstructed images, BPN-C8 exhibited the greatest volumetric distribution of transgene expression (7.4 ± 1.2 mm ^{3}), which is ~1.8 greater than BPN-C6 ($p < 0.05$) (Figure 3.8). We then quantified the volumetric fractions of the GL261 tumor with reporter transgene expression mediated by the nanoparticles. The percentages of total tumor volumes exhibited positive reporter transgene expression were ~85% and ~53% for BPN-C8 and BPN-C6, respectively ($p < 0.05$).

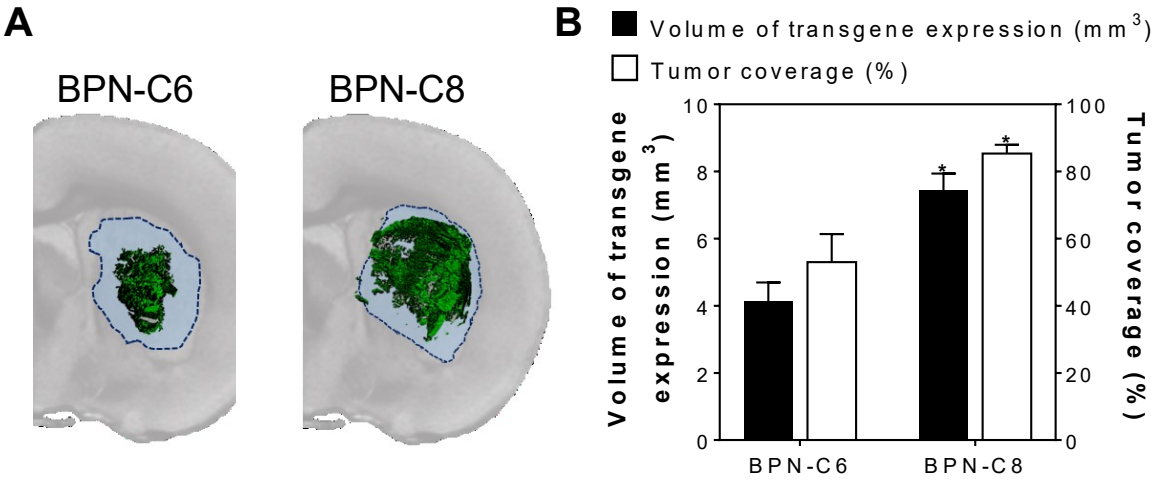

Figure 3.8: Transgene expression mediated by CED of BPN formulations carrying ZsGreen-expressing plasmids in GL261-based orthotopic tumor tissues. (A) Representative isosurface 3D images depicting volumetric distribution of reporter transgene expression (green) in orthotopic brain tumors (outlined by blue-dashed lines) 48 hours after the treatment, obtained by stacking multiple sequential confocal images. Scale bar = 1 mm. **(B)** Volume of transgene expression (n ≥ 3 mice) and percentage of tumor volume covered by transgene expression (n ≥ 3 mice). Differences are statistically significant as indicated (*$p < 0.01$).

Atypical teratoid/rhabdoid tumors AT/RTs are highly aggressive and deadly pediatric brain tumors with a very poor prognosis (*37*). Therapeutic failure in aggressive brain tumors such as AT/RTs is due to the lack of potency of existing agents, intratumoral and intertumoral

heterogeneity, and activation of anti-apoptotic and metabolic programs that allow tumor cells to survive treatment (*38*). AT/RTs share many characteristics with stem cells, including an ability to differentiate into cells with neuronal and “rhabdoid” features, as well as resistance to transfection reagents, chemotherapy and radiation (*27*). Identification and validation of novel gene targets and delivery strategies are essential to develop better therapies and improve the dismal prognosis of these lethal pediatric tumors.

Since BPN-C8 demonstrated better widespread transgene expression in healthy and brain tumor tissue compared to the other candidates, we continued our studies for *in vivo* gene transfer of BPN-C8 in human xenografts for AT/RTs, BT37 and CHLA-06, following CED. The CED experiment was conducted 14 days after the inoculation. Here we confirmed that BPN-C8 can transfect the tumor core in both xenografts model (Figure 3.9). Thus, further validation will be needed to confirm therapeutic efficacy when widespread transgene expression of a tumor-suppressor or a suicide-gene occurs throughout the tumor tissue by BPN-C8 via CED.

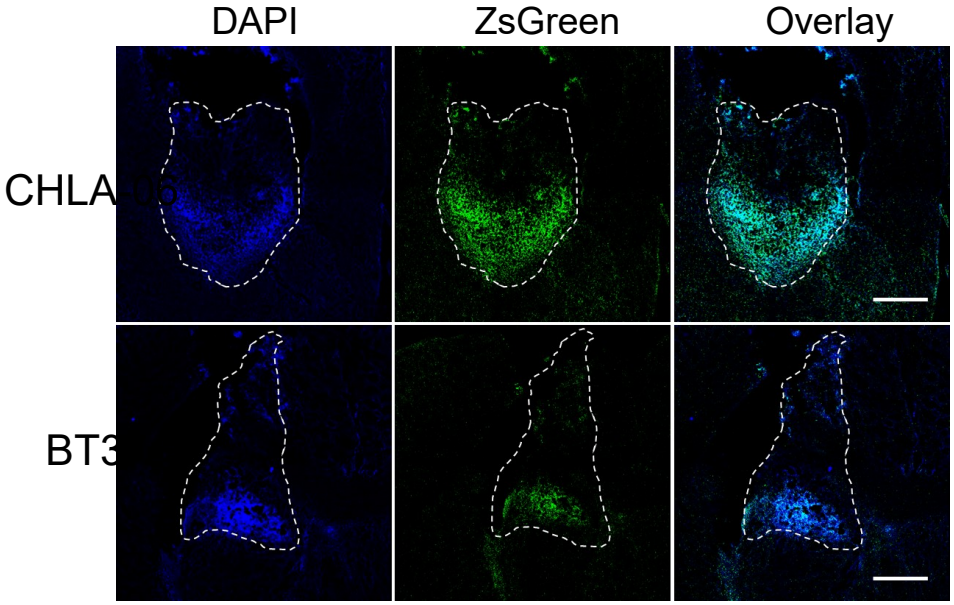

Figure 3.9: Transgene expression mediated by CED of BPN-C8 carrying ZsGreen-expressing plasmids in CHLA-06- and BT37-based orthotopic human xenografts tumor tissues.
Representative images depicting volumetric distribution of reporter transgene expression (green) in orthotopic brain tumors (DAPI, blue). Scale bar = 500 µm.

3.6 Transgene expression mediated by lyophilized BPN-C8

Lyophilized PBAE nanoparticles can be stored for years without losing efficacy (*14*), and are easier to administer, as the user simply needs to add water and inject. To ensure that BPN-C8 did not lose effectiveness after lyophilization, we compared the physicochemical properties of the freshly prepared and lyophilized nanoparticles and found no significant difference between them (Table 3.2). We also compared *in vivo* transgene expression of fresh versus lyophilized BPN-C8 and found that measurements of volumetric distribution of transgene expression showed no statistical difference ($p > 0.05$) (Figure 3.10). This demonstrates that BPN-C8 nanoparticles can be lyophilized with no change in properties or efficacy.

Table 3.2: Physicochemical properties of fresh and lyophilized BPN-C8.

BPN-C8	Hydrodynamic diameter ± SEM (nm)[a]	PDI[a]	ζ-potential ± SEM (mV)[b]	Volume of transgene expression ± SEM (mm^3)
Fresh	60 ± 7	0.09	3.5 ± 4.1	7.2 ± 0.4
Lyophilized	64 ± 4	0.13	4.9 ± 5.5	7.3 ± 0.7

[a] Hydrodynamic diameter and polydispersity index (PDI) were measured by dynamic light scattering (DLS) in ultrapure water. Mean ± SEM (n ≥ 3).

[b] ζ-potential was measured by laser Doppler anemometry in 10mM NaCl at pH 7.0. Mean ± SEM (n ≥ 3).

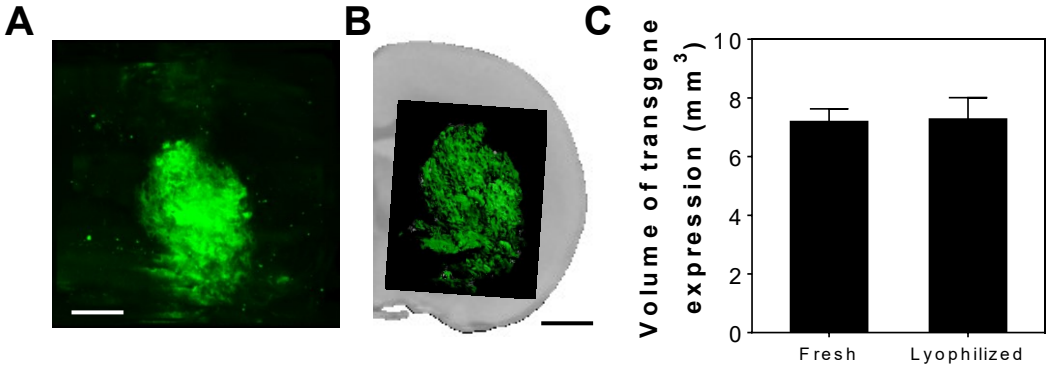

Figure 3.10: Transgene expression mediated by CED of lyophilized BPN-C8 carrying ZsGreen-expressing plasmids in healthy mice brain tissues. (A) Representative Z-stacked confocal images and **(B)** Isosurface 3D images depicting volumetric distribution of reporter transgene expression (green) in healthy mouse brains, obtained by stacking multiple sequential confocal images 48 hours after the treatment. Scale bar = 1 mm. **(B)** Comparative volume of transgene expression mediated by CED of fresh and lyophilized BPN-C8 (n ≥ 4 mice).

4. Discussion

Here we established a series of eight leading PBAE polymers, with similar chemical structure, previously shown to provide efficient *in vitro* gene transfer in 2D cell culture. These polymer variants have never been tested as BPN formulations for widespread gene transfer in the brain following intracranial infusion by CED. Although we did not compare the structure-function relationship of the various candidates in this study, we saw that the small differences in the chemical structure of the end-capping groups led to significant changes in colloidal stability, varying their performance in 3D culture and *in vivo*. As a result, we discover a better BPN formulation for widespread gene transfer in healthy and tumor brain than the previously reported PBAE BPN. Furthermore, this new and stable BPN formulation, when combined with a cryo-protectant, can be lyophilized without changing the physicochemical properties or effectiveness *in vivo*. This allows for reconstitution at a higher concentration, which is particularly beneficial for intracranial injections, in which infusion volumes are limited due to size and pressure constraints within the brain.

The CED approach overcomes a major obstacle hindering the development of drug or gene therapies, i.e. blood-brain barrier permeability. However, as we have shown before, the CED technique is not enough for achieving widespread distribution and transgene expression. Based on our results, a balanced combination of small diameter (< 100 nm), near-neutral surface charge (< 6 mV), small PDI (< 0.2), and colloidal stability in physiological environments (diameter <100 nm and PDI < 0.3, maintained up to 4 hours) is crucial for achieving the best possible distribution and transfection in the brain. Furthermore, in agreement with our previous observations using the gold-standard polyethyleneimine (PEI) polymer (Chapter 2), we confirmed that the overall protein expression level is directly proportional to the volume of transgene expression. This indicates that more cells are getting transfected by the widespread distribution, not by being exposed to a higher amount of DNA nanoparticle in a localized region.

Blind scoring by a certified neuropathologist after nanoparticle delivery via CED is rarely found. Some studies report H&E staining or immunofluorescent images taken within 1 mm around the injection site a few days after nanoparticle administration (*24, 39-41*), with very few reporting long-term safety profiles (*39, 42*). Overall, except for one of our previous studies, there are no reported scores for hemorrhage and inflammation after intracranial nanoparticle delivery (*24*), which makes the comparison of neurotoxicity profiles more challenging. Nevertheless, in agreement with similar studies, we observed no severe neurotoxicity 3 days post-nanoparticle administration, only minimal tissue disruption and inflammation in relation to the acute injury at the needle track. This was comparable for all 4 study groups including sterile medical-grade normal saline, which confirms that the combinational approach of BPN and CED could safely translate into clinical trials, specifically for patients that must undergo brain surgery for tumor resection.

Interestingly, some studies suggest that 2D *in vitro* screening for PBAE polymer-based nanoparticles is more suitable for comparison of transfection efficiencies than multicellular 3D spheroids. This is attributed to the fact that cationic nanoparticles (i.e. UPN) are primarily taken up by the cells in the periphery of the 3D structure, while most of the cells in the interior remain untransfected (*43*). However, we have previously shown (Chapter 2), that 3D multicellular spheroids, unlike 2D cell cultures, serve as an excellent *in vitro* model reliably predicting gene vector behaviors, particularly for DNA nanoparticles possessing greater surface PEG coverage (i.e. BPN) because it better recapitulates architecture and biology of solid tumors observed *in vivo* by simulating an ECM-filled intercellular permeability barrier (*44-47*). Here we confirmed that PBAE BPN efficiently transfect 3D tumor spheroids, with more accurate *in vivo*-correlation than 2D *in vitro* studies. More importantly, we clearly detected a trend with the colloidal stability and physicochemical properties of the eight BPN variants that facilitated the selection of the lead BPN candidate (BPN-C8) and the “negative control BPN” (BPN-C6) for orthotopic tumor studies.

One of the biggest limitations for gene therapy in the brain is poor distribution of therapeutic transgene expression in the tumor region due to high intratumoral pressure (*48*) that facilitates outward diffusion of DNA nanoparticles from the core to the tumor edge. In this study, we noticed that the volume of transgene expression mediated by identically administered BPN was comparable in healthy brain tissue and in GL261-based orthotopic tumor. This is not readily expected as the high cellularity commonly found in tumors would render the intercellular spaces narrower, thereby potentially reinforcing the tumor ECM as a steric barrier. Furthermore, the ability of BPN-C8 to efficiently transfect the tumor tissue in a widespread-manner was consistent in all three orthotopic brain tumor models, including human xenografts for AT/RTs. However, an additional method to confine and sustained therapeutic transgene expression to tumor cells would be desired, particularly when surgery is required, and therapy can exert a toxic effect to normal tissues (e.g. cytotoxic genes).

5. Conclusions

Here we introduce a state-of-the-art biodegradable polymer-based DNA nanoparticle capable of efficiently penetrating both healthy brain parenchyma and brain tumor tissue. Specifically, a lead formulation, BPN-C8, exhibited the greatest ability to provide widespread and high-level transgene expression in 3D tumor spheroids and orthotopically-established brain tumors compared to the other seven BPN candidates. We note that while the PBAE polymer is biodegradable and cannot be store for long term use in water, BPN-C8, when combined with a cryo-protectant, can be lyophilized without changing the physicochemical properties or effectiveness *in vivo*. To this end, our current effort focuses on achieving widespread but cancer-selective therapeutic transgene expression via a marriage of BPN-C8 and promoters designed to drive transgene expression specifically in cancer cells. The non- invasiveness of delivery, the non-immunogenicity of the BPN, and the possibility of re-dosing are all advantages that combine to make an intracranial gene therapy a promising strategy for various types of brain tumors.

6. References

1. A. T. I. Ltd, Phase 2b, Trial of Intravesical DTA-H19/PEI in Patients With Intermediate-Risk Superficial Bladder Cancer. *NCT00595088*, (2008-2014).
2. A. T. I. Ltd., Phase 1/2a Study of DTA-H19 in Advanced Stage Ovarian Cancer. *NCT00826150*, (2009-2012).
3. A. T. I. Ltd., Phase 1/2a DTA-H19 in Patients With Unresectable Pancreatic Cancer. *NCT00711997*, (2008-2013).
4. G. O. Group, EGEN-001 in Treating Patients With Persistent or Recurrent Ovarian Epithelial Cancer, Fallopian Tube Cancer, or Primary Peritoneal Cancer. *NCT01118052*, (2010-present).
5. I. EGEN, Safety and Efficacy of EGEN-001 Combined With Carboplatin and Docetaxel in Recurrent, Platinum-Sensitive, Ovarian Cancer. *NCT00473954*, (2007-2013).
6. J. Chen, Z. Guo, H. Tian, X. Chen, Production and clinical development of nanoparticles for gene delivery. *Mol Ther Methods Clin Dev* **3**, 16023 (2016).
7. M. W. Konstan *et al.*, Compacted DNA nanoparticles administered to the nasal mucosa of cystic fibrosis subjects are safe and demonstrate partial to complete cystic fibrosis transmembrane regulator reconstitution. *Hum Gene Ther* **15**, 1255-1269 (2004).
8. S. Berry *et al.*, Enhancing Intracranial Delivery of Clinically Relevant Non-viral Gene Vectors. *RSC Adv* **48**, 41665-41674 (2016).
9. P. Mastorakos *et al.*, Highly PEGylated DNA Nanoparticles Provide Uniform and Widespread Gene Transfer in the Brain. *Adv Healthc Mater* **4**, 1023-1033 (2015).
10. P. Mastorakos *et al.*, Biodegradable DNA Nanoparticles that Provide Widespread Gene Delivery in the Brain. *Small* **12**, 678-685 (2016).
11. P. Mastorakos *et al.*, Biodegradable brain-penetrating DNA nanocomplexes and their use to treat malignant brain tumors. *J Control Release* **262**, 37-46 (2017).

12. D. G. Anderson, D. M. Lynn, R. Langer, Semi-automated synthesis and screening of a large library of degradable cationic polymers for gene delivery. *Angew Chem Int Ed Engl* **42**, 3153-3158 (2003).

13. D. G. Anderson, A. Akinc, N. Hossain, R. Langer, Structure/property studies of polymeric gene delivery using a library of poly(beta-amino esters). *Mol Ther* **11**, 426-434 (2005).

14. H. Guerrero-Cazares *et al.*, Biodegradable polymeric nanoparticles show high efficacy and specificity at DNA delivery to human glioblastoma in vitro and in vivo. *ACS Nano* **8**, 5141-5153 (2014).

15. C. D. Kamat *et al.*, Poly(beta-amino ester) nanoparticle delivery of TP53 has activity against small cell lung cancer in vitro and in vivo. *Molecular cancer therapeutics* **12**, 405-415 (2013).

16. M. Keeney *et al.*, Development of poly(beta-amino ester)-based biodegradable nanoparticles for nonviral delivery of minicircle DNA. *ACS Nano* **7**, 7241-7250 (2013).

17. H. J. Park *et al.*, Sonic hedgehog intradermal gene therapy using a biodegradable poly(beta-amino esters) nanoparticle to enhance wound healing. *Biomaterials* **33**, 9148-9156 (2012).

18. G. T. Zugates *et al.*, Rapid optimization of gene delivery by parallel end-modification of poly(beta-amino ester)s. *Molecular therapy : the journal of the American Society of Gene Therapy* **15**, 1306-1312 (2007).

19. G. T. Zugates *et al.*, Gene delivery properties of end-modified poly(beta-amino ester)s. *Bioconjug Chem* **18**, 1887-1896 (2007).

20. R. Edmondson, J. J. Broglie, A. F. Adcock, L. Yang, Three-dimensional cell culture systems and their applications in drug discovery and cell-based biosensors. *Assay Drug Dev Technol* **12**, 207-218 (2014).

21. A. Akinc, D. G. Anderson, D. M. Lynn, R. Langer, Synthesis of poly(beta-amino ester)s optimized for highly effective gene delivery. *Bioconjug Chem* **14**, 979-988 (2003).

22. J. J. Green *et al.*, Biodegradable polymeric vectors for gene delivery to human endothelial cells. *Bioconjug Chem* **17**, 1162-1169 (2006).

23. J. R. Greenland *et al.*, Beta-amino ester polymers facilitate in vivo DNA transfection and adjuvant plasmid DNA immunization. *Mol Ther* **12**, 164-170 (2005).

24. P. Mastorakos *et al.*, Highly compacted biodegradable DNA nanoparticles capable of overcoming the mucus barrier for inhaled lung gene therapy. *Proc Natl Acad Sci U S A* **112**, 8720-8725 (2015).

25. J. J. Green, R. Langer, D. G. Anderson, A combinatorial polymer library approach yields insight into nonviral gene delivery. *Acc Chem Res* **41**, 749-759 (2008).

26. J. S. Suk *et al.*, Lung gene therapy with highly compacted DNA nanoparticles that overcome the mucus barrier. *J Control Release* **178**, 8-17 (2014).

27. H. Kaur *et al.*, The chromatin-modifying protein HMGA2 promotes atypical teratoid/rhabdoid cell tumorigenicity. *J Neuropathol Exp Neurol* **74**, 177-185 (2015).

28. V. R. Recinos *et al.*, Combination of intracranial temozolomide with intracranial carmustine improves survival when compared with either treatment alone in a rodent glioma model. *Neurosurgery* **66**, 530-537; discussion 537 (2010).

29. M. F. Weingart *et al.*, Disrupting LIN28 in atypical teratoid rhabdoid tumors reveals the importance of the mitogen activated protein kinase pathway as a therapeutic target. *Oncotarget* **6**, 3165-3177 (2015).

30. X. G. Mao *et al.*, LIN28A facilitates the transformation of human neural stem cells and promotes glioblastoma tumorigenesis through a pro-invasive genetic program. *Oncotarget* **4**, 1050-1064 (2013).

31. E. Song *et al.*, Surface chemistry governs cellular tropism of nanoparticles in the brain. *Nat Commun* **8**, 15322 (2017).

32. A. Greensted. (The Lab Book Pages, 2010).

33. A. Jahangiri *et al.*, Convection-enhanced delivery in glioblastoma: a review of preclinical and clinical studies. *J Neurosurg* **126**, 191-200 (2017).

34. J. I. Ausman, W. R. Shapiro, D. P. Rall, Studies on the chemotherapy of experimental brain tumors: development of an experimental model. *Cancer Res* **30**, 2394-2400 (1970).

35. N. E. Weiner *et al.*, A syngeneic mouse glioma model for study of glioblastoma therapy. *J Neuropathol Exp Neurol* **58**, 54-60 (1999).

36. T. Szatmari *et al.*, Detailed characterization of the mouse glioma 261 tumor model for experimental glioblastoma therapy. *Cancer Sci* **97**, 546-553 (2006).

37. A. Biswas, L. Kashyap, A. Kakkar, C. Sarkar, P. K. Julka, Atypical teratoid/rhabdoid tumors: challenges and search for solutions. *Cancer Manag Res* **8**, 115-125 (2016).

38. P. C. Burger *et al.*, Atypical teratoid/rhabdoid tumor of the central nervous system: a highly malignant tumor of infancy and childhood frequently mistaken for medulloblastoma: a Pediatric Oncology Group study. *Am J Surg Pathol* **22**, 1083-1092 (1998).

39. A. Mangraviti *et al.*, Polymeric nanoparticles for nonviral gene therapy extend brain tumor survival in vivo. *ACS Nano* **9**, 1236-1249 (2015).

40. C. Zhang *et al.*, Strategies to enhance the distribution of nanotherapeutics in the brain. *J Control Release* **267**, 232-239 (2017).

41. A. Arshad *et al.*, Convection-Enhanced Delivery of Carboplatin PLGA Nanoparticles for the Treatment of Glioblastoma. *PLoS One* **10**, e0132266 (2015).

42. W. G. Singleton *et al.*, Convection enhanced delivery of panobinostat (LBH589)-loaded pluronic nano-micelles prolongs survival in the F98 rat glioma model. *Int J Nanomedicine* **12**, 1385-1399 (2017).

43. N. S. Bhise *et al.*, The relationship between terminal functionalization and molecular weight of a gene delivery polymer and transfection efficacy in mammary epithelial 2-D cultures and 3-D organotypic cultures. *Biomaterials* **31**, 8088-8096 (2010).

44. B. M. Baker, C. S. Chen, Deconstructing the third dimension: how 3D culture microenvironments alter cellular cues. *J Cell Sci* **125**, 3015-3024 (2012).

45. C. S. Shin, B. Kwak, B. Han, K. Park, Development of an in vitro 3D tumor model to study therapeutic efficiency of an anticancer drug. *Mol Pharm* **10**, 2167-2175 (2013).

46. C. J. Lovitt, T. B. Shelper, V. M. Avery, Miniaturized three-dimensional cancer model for drug evaluation. *Assay Drug Dev Technol* **11**, 435-448 (2013).

47. S. Sant, P. A. Johnston, The production of 3D tumor spheroids for cancer drug discovery. *Drug Discov Today Technol* **23**, 27-36 (2017).

48. Takamasa Kayama, Takashi Yoshimoto, Shunichi Fujimoto, Yoshiharu Sakurai, Intratumoral oxygen pressure in malignant brain tumor. *Journal of Neurosurgery* **74**, 55-59 (1991).

Chapter 4

Widespread distribution in brain tissue via Pluronic-coated biodegradable nanoparticles

Abstract

Methods capable of providing safe, yet widespread drug delivery to brain cancer cells are much needed**.** It is now well established that simple diffusion-mediated dispersion of conventional therapeutics, including small molecule-, and protein-based drugs, do not provide widespread coverage throughout highly disseminated disease areas within the brain parenchyma. Given that malignant gliomas are characterized by such areas, it is critical to address this issue to deliver the therapeutic cargo to most target cells. Here we developed a nanoparticles (NPs) system using a most widely explored biodegradable polymer for drug delivery platforms made of poly(lactic-co-glycolic acid) (PLGA) blended with various Pluronic-coatings that demonstrated favorable colloidal stability for brain penetration after intracranial administration. After careful analysis of the volumetric distribution of the various Pluronic candidates in healthy rat brain tissue followed by convection enhanced delivery (CED), we identified the formulation with a dense layer of poloxamer 407, Pluronic F127 (F127/PLGA-NPs), as the lead candidate for efficient shielding and brain penetration. Furthermore, F127/PLGA-NPs effectively achieved widespread distribution in a highly aggressive orthotopic brain tumor model. Lastly, we successfully developed a method for cryoprotection of this formulation without compromising their penetrating properties and yet significantly improved brain distribution by infusing F127/PLGA-NPs via CED in a hyperosmolar infusate solution. This multimodal delivery strategy minimizes the hindrance of NPs diffusion imposed by the brain extracellular matrix and reduces NPs confinement within the perivascular spaces. These findings provide a strategy to overcome several key limitations previously observed in clinical trials.

1. Introduction

Achieving widespread distribution in the brain parenchyma is essential when it comes to the design of therapeutic nanoparticles (NPs) for treating brain diseases (*1, 2*). As previously discussed, NPs delivery systems used for the treatment of brain tumors is challenging due to the presence of multiple anatomical barriers. Furthermore, the lack of efficacy of locally delivered systems stem from the impaired diffusional capabilities of the chemotherapeutic released after infusion. This limits their application for long-term treatment regimens, further supporting a need for a NP platform that can penetrate within the brain and provide sustained release of a therapeutic.

Surfactants are frequently used to stabilize particle emulsions, enhance drug loading, alter drug release, and change surface properties (*3*). As early as 1994, it was demonstrated that nanospheres, synthesized from amphiphilic copolymers composed of two biocompatible blocks (including PEG), exhibit dramatically increased blood circulation times and low liver accumulation in mice (*4*). Several PEG-containing block copolymers were then developed and among them, the amphiphilic and polymeric characters of Pluronic® block copolymers such as poloxamer 188 (F68), poloxamer 288 (F98), and poloxamer 407 (F127) have raised growing interest for the design of drug delivery systems (*5*) (Figure 4.1). F68 and F127 have been used to coat poly(lactic-co-glycolic acid) (PLGA) NPs to promote blood-brain barrier penetration (*6*). They have also been shown to improve efficacy against intracranial gliomas compared to uncoated particles (*7-9*). However, their effect on brain tissue penetration within the brain extracellular matrix (ECM) followed by convection-enhanced delivery (CED) is still unknown, particularly for F98, which has not received the same attention as F68 and F127 in scientific literature.

Pluronic-coated biodegradable NPs present a potential drug delivery platform that could enhance treatments against diffusive brain diseases, particularly, infiltrative glioblastomas, by providing greater brain tissue penetration and broader therapeutic distribution in a safely

manner. To this end, we studied the impact of three Pluronic candidates (F68, F98, and F127), in relationship to their physicochemical properties favoring brain penetration followed by CED, using concepts and optimized procedures discussed in previous chapters. Moreover, we used PLGA, one of the most successfully developed biodegradable polymers for protection of drug from degradation, sustained release, and possibility to modify surface properties to provide stealthness and/or better interaction with biological materials (Figure 4.1B) (*10, 11*). We then compared the volumetric distribution of the three types of Pluronic-coated PLGA NPs in relationship to their size and charge, to select the lead NP formulation for further CED optimization and tumor studies.

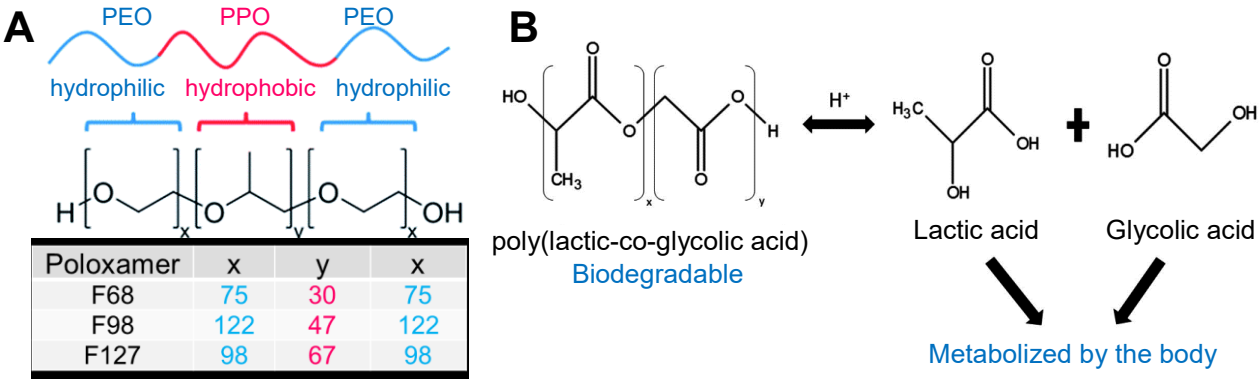

Poloxamer	x	y	x
F68	75	30	75
F98	122	47	122
F127	98	67	98

Figure 4.1: (A) Pluronic block copolymers (also known as "poloxamers"), consist of hydrophilic poly(ethylene oxide) (PEO) and hydrophobic poly(propylene oxide) (PPO) blocks arranged in X-Y-X tri-block structure: PEO-PPO-PEO. Reproduced by Gottschalck and McEwen, 2004. **(B)** Biodegradability of PLGA based on the hydrolysis of the copolymer to generate the monomers, lactic and glycolic acid, which are metabolized by the body via the Krebs cycle. Reproduced by Nanovex Biotech Inc.

2. Materials and Methods

2.1 PLGA labeling with a fluorescence dye

PLGA polymer (carboxyl terminated, 50:50 monomer ratio) (Resomer RG 503-H, MW: 30,500) was purchased from Evonik Industries (Darmstadt, Germany) and conjugated with fluorescein cadaverine dye ($\lambda_{Ex}/\lambda_{Em}$: 493/517 nm) (Biotium, Fremont, CA). The reaction was carried out by carbodiimide conjugation, activating carboxyl groups from PLGA for direct reaction with the primary amine via amide bond formation (Figure 4.2). Briefly, PLGA polymer was dissolved in dimethylformamide (DMF) and activated by N', N-di-cyclohexyl carbodiimide

(DCC) and N-hydroxysulfosuccinimide (NHS). The reaction was carried out for 3 hours under constant stirring at room temperature and controlled vacuum with inert N_2 gas. Then, pH was adjusted to 7.5 and the fluorescein cadaverine dye was dissolved in DMF and added immediately to the activated polymer solution to react at a polymer:dye molar ratio of 1:1.2, respectively. This reaction was carried out overnight under constant stirring at room temperature and protected from light. Next, DMF was added to dissolve the precipitates and the solution was filtered by gravity using a Pasteur pipette. Then, the solution was dialyzed for 3 hours against DMF using a Spectra/Por® 6 Standard RC 1kD dialysis membrane (Spectrum Laboratories, Inc., Rancho Dominguez, CA). Lastly, DMF was evaporated using a Biotage® V-10 Touch evaporation system (Biotage, Charlotte, NC) and dye conjugation was confirmed by nuclear magnetic resonance (NMR) analysis.

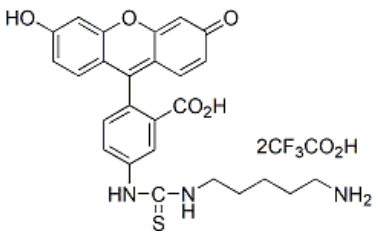

HO-polymer-COOH #1 + Dye-NH_2 #2 → HO-polymer-CO-NH-Dye

DCC #3, NHS #4

	#1	#2	#3	#4
MW	30,500	719.6	206.33	11
Amount	200 mg	**5.66 mg**	**2.6 mg**	**1.5 mg**
mmols	**0.0065**	0.0078		
	Eq 1	Eq 1.2	Eq 2	Eq 2

Figure 4.2: Reaction scheme for polymer-dye conjugation.

2.2 Nanoparticle formulation in ultrapure water

Organic solvents used for preparing polymer solution are known to affect the size of PLGA NPs synthesized through emulsion procedures (*12*). Partially water-miscible organic solvents—such as benzyl alcohol, butyl lactate, and ethyl acetate—allow nanoparticle formulation through an emulsion-diffusion mechanism and can produce smaller nanoparticles than water-immiscible

solvents such as dichloromethane (DCM). Furthermore, Saltzman et al. reported that replacing DCM with ethyl acetate and using the double-emulsion technique improved the yield of small nanoparticles (< 100 nm in diameter) (*13*).

We adapted this protocol to formulate uncoated PLGA NPs by double-emulsion method (Figure 4.3). Briefly, fluorescently labeled PLGA polymer was dissolved in acetonitrile (ACN) at 30 mg/ml and 500 µL of the polymer solution was added dropwise into 2 mL of ultrapure water using an SGE syringe (Supelco Inc., Bellefonte, PA). The solution was stirred for 1 hour at room temperature for the primary emulsion, where nanoparticles were formed spontaneously. Then, the emulsion was poured into a beaker with 10 mL of ultrapure water to allow the secondary emulsion to form. This was followed by an additional 4 hours of stirring to allow the solvent to evaporate and particles to harden. After solvent evaporation, the particle solution was washed once with 1 volume of ultrapure water and collected using Amicon Ultra Centrifugal Filters (100,000 MWCO; Millipore Corp., Billerica, MA) at 4,000 x g for 12 minutes until final volume in the filter unit was 500 µL.

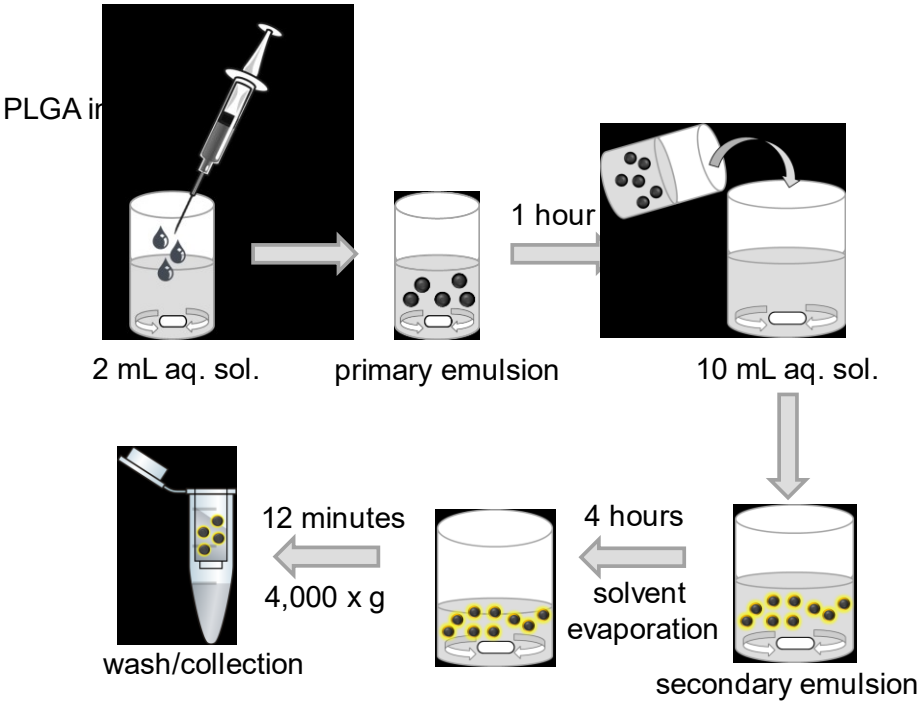

Figure 4.3: Schematic protocol for the formulation of PLGA NPs.

2.3 Nanoparticle formulation in F68, F98, and F127 aqueous solution

Similarly, fluorescently labeled PLGA polymer was dissolved in ACN at 30 mg/ml and 500 µL of the polymer solution was added dropwise into 2 mL of 1% F68, 1% F98, or 1% F127 aqueous solution, using an SGE syringe. The solution was stirred for 1 hour at room temperature for the primary emulsion, where nanoparticles were formed spontaneously. Then, the emulsion was poured into a beaker with 10 mL of 0.5% F68, 0.5% F98, or 0.5% F127 aqueous solution to allow the secondary emulsion to form. This was followed by an additional 4 hours of stirring to allow the solvent to evaporate and particles to harden. After solvent evaporation, the particle solution was washed once with 1 volume of ultrapure water and collected using Amicon Ultra Centrifugal Filters (100,000 MWCO; Millipore Corp., Billerica, MA) at 4,000 x g for 12 minutes until final volume in the filter unit was 500 µL.

Particle diameter is directly proportional to the polymer concentration (*14*). Thus, the same protocol was used to formulate F127/PLGA-NPs of various sizes (~60 to 350 nm) by adjusting the PLGA starting concentration to 5, 10, 30, 50, 60, 80 mg/ml in ACN.

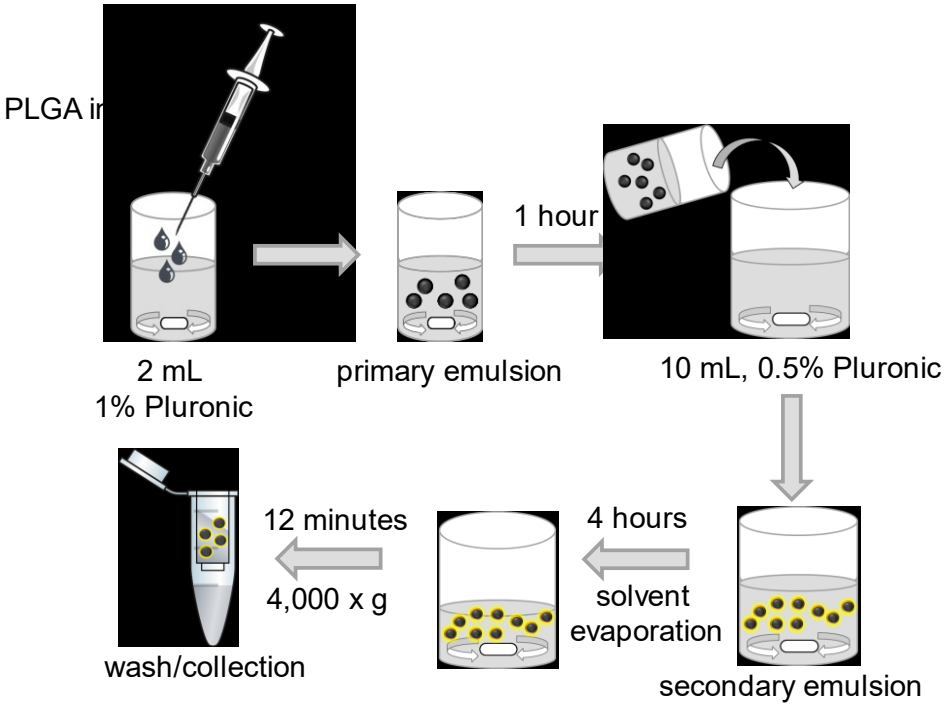

Figure 4.4: Schematic protocol for the formulation of Pluronic-coated PLGA NPs.

2.4 Physicochemical characterization of PLGA NPs

The hydrodynamic diameters as well as polydispersity index (PDI) and ζ-potentials of uncoated and Pluronic-coated PLGA NPs were measured by dynamic light scattering (DLS) and laser Doppler anemometry in 10 mM NaCl solution at pH 7.0, using a Nanosizer ZS90 (Malvern Instruments, Southborough, MA). The size and morphology of nanoparticles were also confirmed by transmission electron microscopy (TEM) (Hitachi H7600, Japan). Colloidal stability was assessed by monitoring the change in hydrodynamic diameters and PDI in artificial cerebrospinal fluid (aCSF) (Harvard Apparatus, Holliston, MA) at 37 °C.

2.5 Animal studies

We used 6-to-8-week-old female Fischer 344 rats for the assessment of the volume of distribution of the various PLGA NPs. Animals were treated in accordance with the guidelines and policies of the Johns Hopkins University Animal Care and Use Committee. Surgical procedures were performed using standard sterile surgical techniques. Animals were anesthetized using a mixture of 75 mg/kg ketamine and 7.5 mg/kg xylazine, as previously described (*15*). A midline scalp incision was made to expose the coronal and sagittal sutures and a burr whole was drilled 3 mm lateral to the sagittal suture and 0.5 mm posterior to the bregma. Following the tumor cell inoculation or PLGA NPs administration, the skin was sealed using biodegradable sutures (Polysorb™ Braided Absorbable Sutures 5–0) and bacitracin was applied.

2.5.1 Orthotopic tumor inoculations

Orthotopic tumor cell inoculations were performed as previously described in Chapter 2 (*15*). Briefly, 100,000 cells of rat glioblastoma cells expressing mKate fluorescent protein (F98-mKate), were administered in 10 µL of DMEM over 5 minutes at a depth of 3.5 mm using a Neuros Syringe (50 µL; Hamilton, Reno, NV) mounted on an ultra-precise small-animal stereotactic frame. Of note, we inoculated rat brains with a high numbers of tumor cells, relevant

to clinical translation (*16, 17*), to establish a model mimicking malignant gliomas characterized by rapid tumor growth rates.

2.5.2 Intracranial administration - CED

To assess the volume of distribution of the various PLGA NPs, fluorescently labeled NPs were intracranially administered via CED. Briefly, a Neuros syringe connected to a 33-gauge needle was filled with 20 µL of PLGA NPs solution at a polymer concentration of 15 mg/mL and lowered to a depth of 3.5 or 2.5 mm of a healthy or an orthotopic tumor-bearing rat brain, targeting the striatum or the tumor core, respectively. PLGA NPs were then infused at a rate of 0.5 µL/min as controlled by a Chemyx Nanojet Injector Module (Chemyx, Stafford, TX).

2.5.3 Imaging and quantification of volumetric of distribution

Brains were harvested immediately after PLGA NPs administration and flash-frozen in dry-ice. Tissues were then sectioned using a Leica CM 1905 cryostat into 100 or 50 µm coronal slices for healthy or tumor-bearing rats at ± 3 mm of the infusion plane in striatum or until the tumor tissue was no longer visible, respectively. All fluorescence images were taken using an LSM 710 confocal microscope under 5X magnification. We carefully optimized the settings to avoid background fluorescence based on the microscopy of untreated control rat brains. The volume of distribution was quantified using a custom-made MATLAB script that subtracted background fluorescence by Otsu's method of thresholding (39, 40). The area of PLGA NPs coverage in each slice was integrated to calculate the total volume of distribution.

To reconstruct 3D-rendered imaginings of F127/PLGA-NPs distribution in orthotopic tumor, we stacked and aligned the acquired images using Metamorph ® Microscopy Automation & Image Analysis Software (Molecular Devices, CA). Finally, we used an Imaris Software (Bitplane, CT) to create 3D isosurfaces.

2.5.4 Histological analysis and safety profile

Animals were sacrificed 3 days following administration and the harvested brains were fixed in 4% formaldehyde, processed, sectioned and stained with hematoxylin and eosin (H&E) by the Johns Hopkins Reference Histology Laboratory. The point of infusion was identified by the tissue cavity imparted by the needle and the region immediately adjacent was imaged and evaluated. Blind histopathological analysis was performed by a board-certified neuropathologist and tissues were scored from 0–3 for indications of inflammation and hemorrhage (0: no inflammation/hemorrhage, 1: mild, 2: moderate, 3: severe).

2.6 Lyophilization and administration of the “ready-to-use” F127/PLGA NPs

For lyophilized F127/PLGA-NPs formation and evaluation, NPs were initially formed as described above at two different PLGA concentrations, 5 and 30 mg/ml. Subsequently, sucrose (OPS Diagnostics, Lebanon, NJ) was added as a cryoprotectant to a final concentration of 30 mg/mL, diluting the solution of F127/PLGA-NPs by 2-fold. Particles were then frozen in dry-ice and lyophilized overnight. Lyophilized F127/PLGA-NPs were stored at -20 °C until use and then reconstituted in sterile ultrapure water and used at the same concentration as freshly prepared F127/PLGA-NPs.

To assess the effect of osmolality of infusate solutions on the distribution of the “ready-to-use” F127/PLGA-NPs in the brain parenchyma, the osmotic pressures were adjusted by addition of NaCl to a final osmolality of 300 mOsm/kg, 370 mOsm/kg, and 480 mOsm/kg and intracranially administered via CED. The CED and imaging procedure were executed as described above.

2.7 Statistical Analysis

Statistical analysis between two groups was conducted using a two-tailed Student's t-test assuming unequal variances. If multiple comparisons were involved, one-way analysis of variance (ANOVA), followed by Sidak's multiple comparisons test, was employed, using

GraphPad Software (GraphPad Software Inc., La Jolla, CA). Differences were determined to be statistically significant at $p < 0.05$. Values are presented as mean ± standard error of the mean (SEM).

3. Results

3.1. Physicochemical characterization of PLGA NPs

We formulated Pluronic-coated PLGA NPs by double-emulsion method, mixing the organic PLGA solution into various aqueous Pluronic solutions, F68, F98, and F127. The uncoated PLGA NPs were formed in ultrapure water as a negative control. Hydrodynamic diameter and PDI were measured by DLS in 10 mM NaCl. The ζ-potential was measured by laser Doppler anemometry in 10mM NaCl at pH 7.0. At least 3 independent experiments were performed for this analysis. Table 4.1 shows that all Pluronic-coated PLGA NPs possessed a hydrodynamic diameter of ~130 nm and a low PDI ~0.1, whereas uncoated PLGA NPs possessed a slightly larger hydrodynamic diameter of ~140 nm and higher PDI of ~0.18. On the other hand, the surface charge showed a trend from highly negative to near neutral, as indicated by the ζ-potential, in the following order: uncoated > F68 > F98 > F127: -50 ± 9 , -26 ± 3 , -9 ± 3 , -4 ± 3 mV , respectively (Figure 4.5). The particle morphology was confirmed by TEM to be ~150 nm spheres regardless of type of coating (Figure 4.5C), consistent with the measured hydrodynamic diameters (Table 4.1).

Lastly, we assessed the hydrodynamic diameters of the various PLGA NPs following a 12-hour incubation in aCSF at 37ºC to predict potential alteration of particle properties in the physiological brain environment. We found all formulations retained their hydrodynamic diameters and PDI in aCSF. Notably, F98 showed less colloidal stability than the other groups, but even with the drastic and sudden changes, it retained the diameter in similar range as the other PLGA NPs (Figure 4.6).

Table 4.1: Physicochemical properties of PLGA NPs with various Pluronic

	Z-Average ± SEM (nm)[a]	Number mean ± SEM (nm)[a]	PDI[a]	ζ-Potential ± SEM (mV)[b]
Uncoated	180 ± 8	140 ± 6	0.18	-50 ± 9
F68	158 ± 2	126 ± 3	0.09	-26 ± 3
F98	162 ± 5	128 ± 4	0.12	-9 ± 3
F127	161 ± 1	134 ± 3	0.07	-4 ± 3

[a] Hydrodynamic diameter and polydispersity index (PDI) were measured by dynamic light scattering (DLS) in 10 mM NaCl at pH 7.0. Mean ± SEM (n ≥ 3).

[b] ζ-potential was measured by laser Doppler anemometry in 10 mM NaCl at pH 7.0. Mean ± SEM (n ≥ 3).

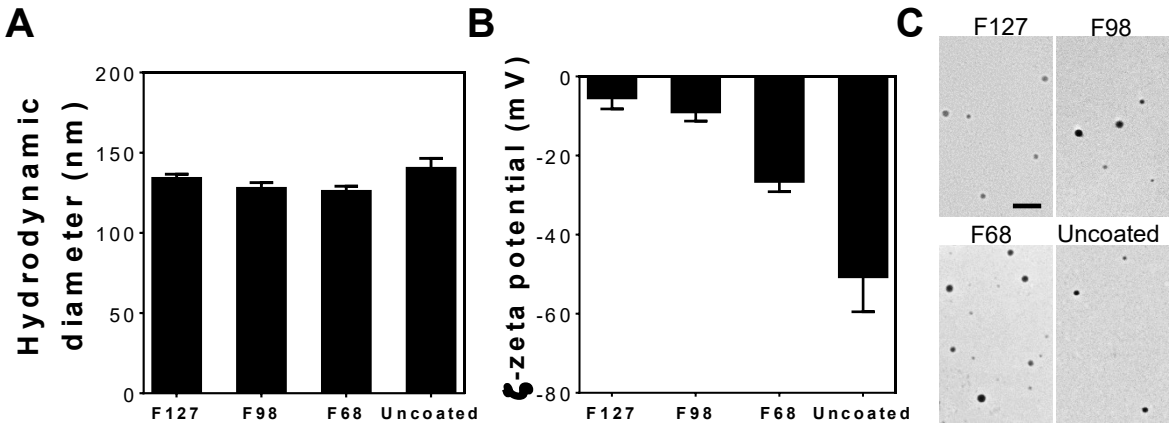

Figure 4.5. Physicochemical properties of various PLGA NPs. (A) Hydrodynamic diameters of 30 mg/ml PLGA NPs were measured by DLS in 10 mM NaCl at pH 7.0. Mean ± SEM (n ≥ 3). **(B)** ζ-potential was measured by laser doppler anemometry in 10 mM NaCl at pH 7.0. Mean ± SEM (n ≥ 3). **(C)** Transmission electron microscopy images of PLGA NPs coated with F127, F98, F68, and uncoated when freshly made in ultrapure water. Scale bar = 800 nm.

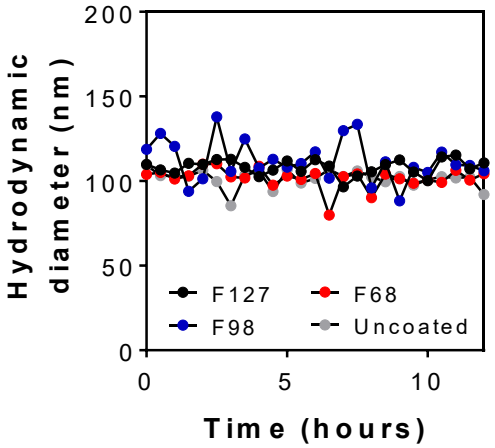

Figure 4.6: Colloidal stability over 12 hours in aCSF at 37°C measured by DLS.

3.2. Volume of distribution in healthy rat brains

The various PLGA NPs were administered into the rats striatum via CED, which, as previously described, has been clinically applied to enhance the therapeutic distribution within brain by creating a continuous pressure-driven bulk flow (*18, 19*). The volume of distribution was then assessed immediately after the treatment. The representative images showing the coronal plane at the site of administration revealed enhanced volumes of distribution for all Pluronic-coated PLGA NPs, whereas the uncoated control was confined around the needle track (Figure 4.7A). The trend seen in the volume of distribution of PLGA NPs in rat brains was inversely correlated to their surface charge: F127 > F98 > F68 > uncoated. Quantitively, F127/PLGA-NPs exhibited significantly greater volumetric distribution compared to all the groups (Figure 4.7B), with an average volumetric distribution of 38 ± 5 mm^3, 23 ± 3 mm^3, 13 ± 0.7 mm^3, 4 ± 0.7 mm^3, for F127, F98 (p <0.05), F68 (p < 0.001), uncoated (p < 0.001), respectively. Notably, F98/PLGA-NPs showed the second highest value for volume of distribution, exhibiting statistical significance when compared to F68 (p < 0.05) and uncoated (p < 0.01) NPs.

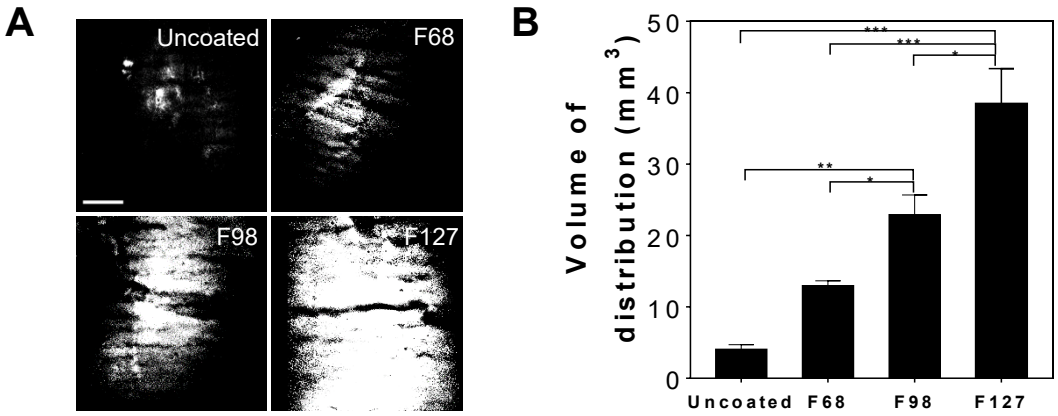

Figure 4.7: Volume of distribution mediated by CED of various PLGA NPs in healthy rat brain tissues. (A) Representative 2D images depicting volumetric distribution at the infusion site of PLGA NPs when uncoated, and coated with F68, F98, and F127 in healthy rat brains, obtained by confocal microscopy immediately after NPs treatment. Sale bar = 1 mm. **(B)** Quantification of the volume of distribution of PLGA NPs (n ≥ 4 rats). Differences are statistically significant as indicated (*p < 0.05, **p < 0.01, ***p < 0.001).

We also confirmed that the two best Pluronic candidates, F98 and F127, were still present in the brain parenchyma after 48 hours from NPs treatment, albeit, the volume of distribution

decreased by ~2-fold when compared to the volume of distribution achieved immediately after CED. Quantitively, F98 showed a volumetric distribution of 10 ± 2 mm^3, whereas F127 demonstrated significantly greater distribution than F98 by ~2-fold, with 22 ± 3 mm^3 ($p < 0.05$).

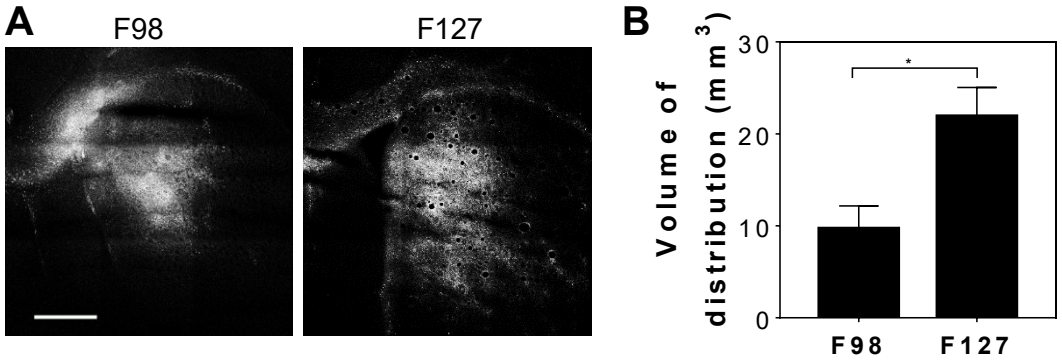

Figure 4.8: Volume of distribution of F98/PLGA-NPs and F127/PLGA-NPs 48 hours after CED. (A) Representative 2D images depicting volumetric distribution at the infusion site in healthy rat brains, obtained by confocal microscopy 48 hours after NPs treatment. Sale bar = 1 mm. **(B)** Quantification of the volume of distribution of F98/PLGA-NPs and F127/PLGA-NPs (n ≥ 3 rats) (t-test, *$p < 0.05$).

3.3. Effect of polymer concentration on F127/PLGA-NPs

Next, we evaluated the effect of PLGA concentration on the physicochemical properties of the F127/PLGA-NPs. The aforementioned data of the various types of PLGA NPs was taken from batches at a starting polymer concentration of 30 mg/ml. This same protocol was then adjusted to formulate F127/PLGA-NPs of various sizes (~60 to 350 nm) by changing the PLGA starting concentration to 5, 10, 30, 50, 60, 80 mg/ml. Here, the batch of F127/PLGA-NPs at a starting concentration of 30 mg/ml was used as a control. The highest polymer concentration that provided consistent NPs yield, according to DLS, was 80 mg/ml; concentrations greater than that one did not allow successful recovery during the washing process due to significant polymer aggregation (data not shown).

Table 4.2 shows a tendency consistent with the expected results, where increments of the starting PLGA concentration yielded larger diameters. Although the PDI was not significantly affected by the polymer concentration, the surface charge showed a “more negative” inclination as the PLGA concentration increased. Note, we named each condition based on the

hydrodynamic diameter after the number mean reported by DLS. For example, “F127/PLGA-130” refers to the control batch of 30 mg/ml, which showed a hydrodynamic diameter of 135 ± 5 nm. Lastly, we assessed the colloidal stability of the various F127/PLGA-NPs (only four are shown in Figure 4.9) and confirmed that the hydrodynamic diameters did not change over time in physiological conditions.

Table 4.2: Effect of polymer concentration on physiochemical properties of F127/PLGA-NPs.

F127/PLGA-NPs	Polymer concentration (mg/ml)	Z-Average ± SEM (nm)[a]	Number mean ± SEM (nm)[a]	PDI[a]	ζ-Potential ± SEM (mV)[b]
F127/PLGA-60	5	89 ± 2	63 ± 3	0.07 ± 0.05	-1.6 ± 6.2
F127/PLGA-100	10	111 ± 8	89 ± 8	0.08 ± 0.04	-2.2 ± 5.8
F127/PLGA-130	30	160 ± 7	135 ± 5	0.08 ± 0.03	-3.5 ± 4.5
F127/PLGA-170	50	198 ± 9	171 ± 13	0.10 ± 0.02	-4.0 ± 4.2
F127/PLGA-200	60	257 ± 1	198 ± 4	0.16 ± 0.02	-4.6 ± 4.3
F127/PLGA-350	80	387 ± 14	341 ± 36	0.10 ± 0.04	-4.8 ± 4.1

[a] Hydrodynamic diameter and PDI were measured by DLS in 10 mM NaCl ± SEM (n ≥ 3).
[b] ζ-potential was measured by laser Doppler anemometry in 10 mM NaCl. Mean ± SEM (n ≥ 3).

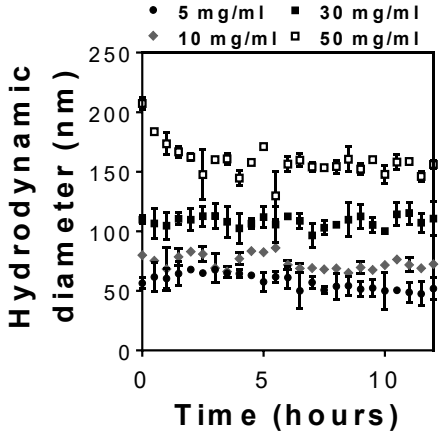

Figure 4.9: Effect of polymer concentration in colloidal stability of F127/PLGA-NPs. Colloidal stability over 12 hours in aCSF at 37°C measured by DLS.

3.4. Effect of changes in diameter on *in vivo* volume of distribution

As discussed in previous chapters, cationic polymer-based NPs have a “sticky” limitation when it comes to brain penetration, which is due to the adhesive moieties of brain ECM and other brain-related barriers. Moreover, we have shown that NPs larger than ~120 nm cannot

efficiently diffuse in *ex vivo* and *in vivo* brain tissue even after PEGylation (*20*). To this end, we evaluated whether F127/PLGA-NPs possessing large diameters and a near neutral, yet slightly negative, surface charge can still achieve widespread distribution when combined with the CED technique. For this study we selected four of the six groups from Table 4.2, F127/PLGA-60, 130, 170, and 200 nm.

Figure 4.10 establishes that the widespread distribution is inversely correlated with the hydrodynamic diameter. Quantitively, there was no significant difference between the particles in the smaller range, 60 nm and 130 nm, showing 40 ± 4 mm^3 and 38 ± 5 mm^3, for the volume of distribution, respectively. Similarly, the particles in the larger range, 170 nm and 200 nm, achieved comparable distribution, showing 25 ± 5 mm^3 and 24 ± 3 mm^3, respectively. Both, 60 and 130 nm NPs demonstrated statistical significance when compared to 200 nm NPs ($p < 0.05$) but not against 170 nm NPs.

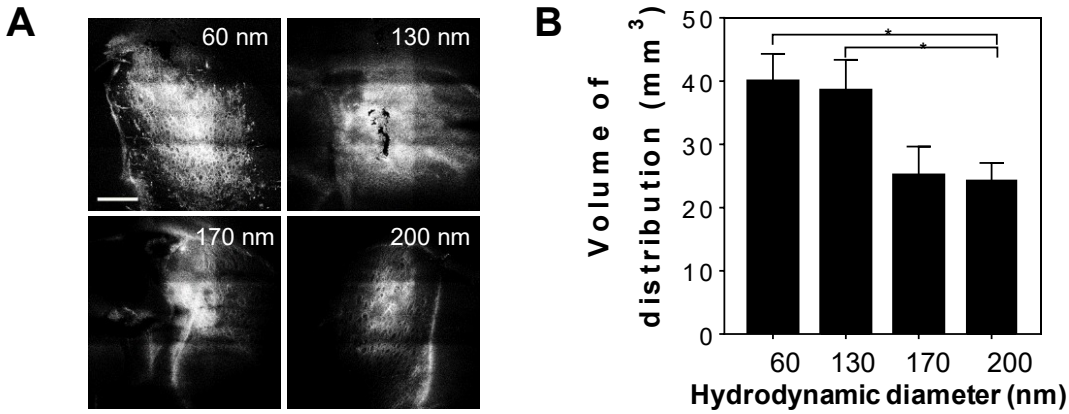

Figure 4.10: Volume of distribution mediated by CED of different sizes of F127/PLGA-NPs in healthy rat brain tissues. (A) Representative 2D images depicting volumetric distribution at the infusion site in healthy rat brains, obtained by confocal microscopy immediately after NPs treatment. Sale bar = 1 mm. **(B)** Quantification of the volume of distribution of the various F127/PLGA-NPs (n ≥ 4 rats) (t-test *$p < 0.05$).

3.5. Histopathological analysis and safety profile

To demonstrate the safety of Pluronic-coated PLGA NPs followed by intracranial administration via CED, we compared the toxicity of F98/PLGA NPs and F127/PLGA NPs to medical-grade normal saline (NS) by histology safety profile in the rats' striatum. Followed 3

days from the NPs administration, the average toxicity scores of the brain tissues for both Pluronic coatings were comparable to those of NS-treated controls (Figure 4.11), with an average score of ~1.5-2 for hemorrhage and inflammation, suggesting that they were well-tolerated at the dose administered (15 mg/mL, 20 µL). Notably, the inflammation score increased with the respective volume of distribution in the brain (F127 > F98). Importantly, regardless of the type of particle, inflammatory and hemorrhagic changes were confined around the injection site and did not propagate throughout the brain tissue. All hemorrhage and inflammation scores were negligible, ~0-1, after 30 days (data not shown).

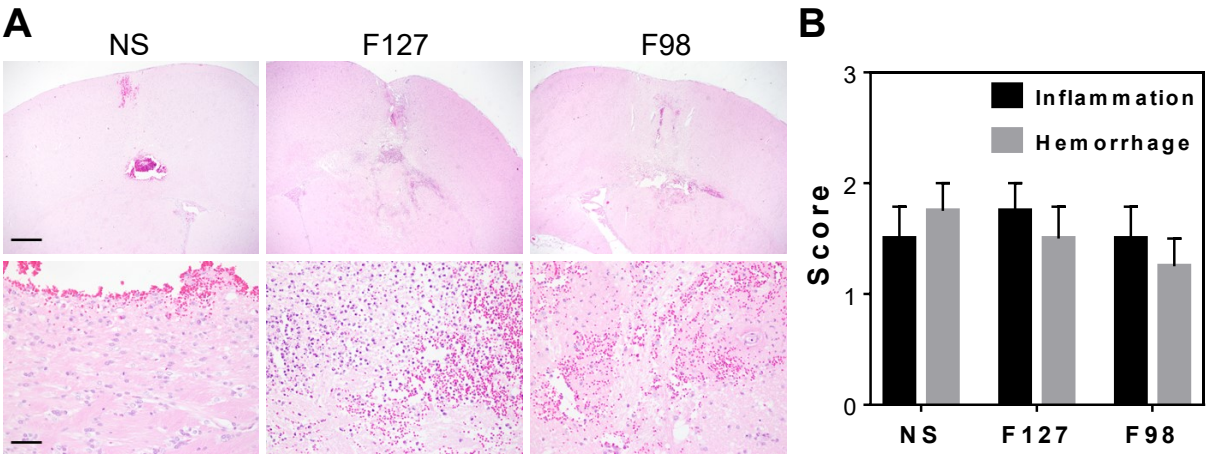

Figure 4.11: Histopathological analysis and safety profile of F98/PLGA-NPs and F127/PLGA-NPs following CED administration. (A) Representative images of the injection site with hematoxylin and eosin staining in healthy brain tissue 3 days after CED at 20X (top, scale bar = 500 µm) and 200X (bottom, scale bar = 100 µm) magnitude. Normal saline was used as a control. **(B)** Inflammation and hemorrhage were scored by a board-certified neuropathologist using a custom scale (0: no inflammation/hemorrhage, 1: mild, 2: moderate, 3: severe).

3.6. Widespread distribution in orthotopic brain tumors

We next evaluated whether F127/PLGA-NPs can effectively diffuse and penetrate the dense cellularity within an orthotopic model of aggressive brain tumor following CED. The model was established by intracranial stereotactic inoculation of 1 x 10^5 F98 cells and a CED experiment was conducted 10 days after the inoculation when a large volume (~50 mm^3) of orthotopic tumor was established in the rat striatum. As shown by representative 3D-reconstructed images, F127/PLGA-NPs exhibited almost 100% tumor coverage, with

widespread distribution inside and outside the tumor core (Figure 4.12). Highly invasive tumor cells that migrate beyond the tumor edge and infiltrate into normal brain tissue are responsible for recurrence of malignant gliomas (*21*). Thus, the unique ability of F127/PLGA-NPs to efficiently penetrate both normal brain parenchyma and brain tumor tissue may serve favorably for this specific application.

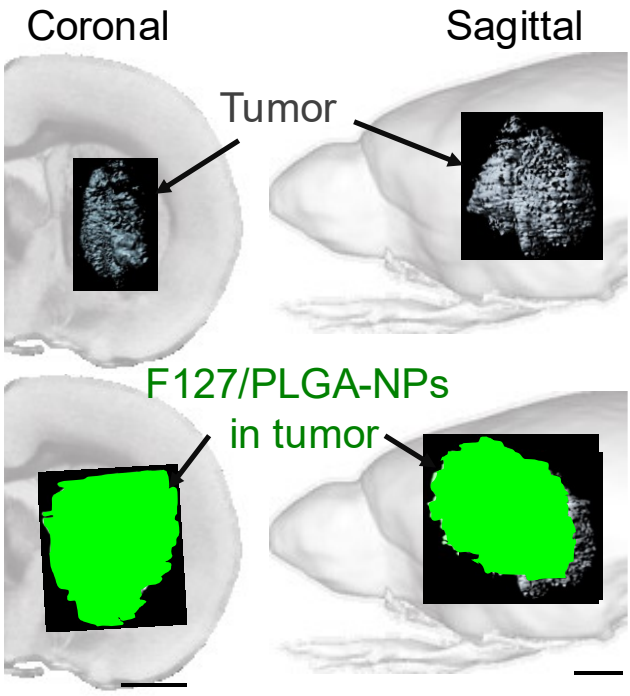

Figure 4.12: Volume of distribution mediated by CED of F127/PLGA-NPs in F98-mKate rat tumor brain tissues. Representative 3D-rendered images depicting volumetric distribution of F127/PLGA-NPs (green, outlined by short-green-dashed lines) in orthotopic F98-mKate brain tumors (light gray, outlined by long-red-dashed lines), obtained by stacking multiple sequential confocal images. Top panel shows overlap between F127/PLGA-NPs and tumor bulk. Bottom panel shows areas where F127/PLGA-NPs are surrounding the tumor. Scale bar = 2 mm.

3.7. Lyophilization and cryoprotection of F127/PLGA-NPs

Pluronic-coated PLGA NPs are stable at room temperature in aqueous solution, therefore, they can retain their colloidal stability for weeks and even months (Table 4.3). However, without proper care, the polymer concentration can be affected over time due to water evaporation, which could lead to “gel-like” consistency. Therefore, lyophilized NPs are more convenient for handling, as they the user simply needs to add water to adjust the desired concentration and

inject. To ensure that F127/PLGA-NPs do not lose their nanoparticle characteristics after lyophilization, we compared the physicochemical properties of two different types of F127-coated NPs, 60 nm and 130 nm, with and without sucrose as a cryoprotectant. As Table 4.4 shows, particles without sucrose do not retain the original size and charge, whereas particles properly mixed with sucrose kept comparable values as the original solution.

Table 4.3: Physiochemical properties of Pluronic-coated PLGA NPs after a month.

NP condition	Z-Average ± SEM (nm)[a]	Number mean ± SEM (nm)[a]	PDI[a]	ζ-Potential ± SEM (mV)[b]
F98/PLGA-130 (1 month)	172 ± 5	131 ± 5	0.13	-8 ± 4
F127/PLGA-130 (1 month)	170 ± 6	129 ± 2	0.11	-4 ± 3

[a] Hydrodynamic diameter and PDI were measured by DLS in 10 mM NaCl ± SEM (n ≥ 3).
[b] ζ-potential was measured by laser Doppler anemometry in 10 mM NaCl at pH 7.0. Mean ± SEM (n ≥ 3).

Table 4.4: Physiochemical properties of F127/PLGA-NPs after lyophilization.

NP condition	Z-Average ± SEM (nm)[a]	Number mean ± SEM (nm)[a]	PDI[a]	ζ-Potential ± SEM (mV)[b]
F127/PLGA-60 (no sucrose)	124 ± 3	93 ± 2	0.14 ± 0.03	-3.7 ± 8.8
F127/PLGA-60 (with sucrose)	93 ± 5	52 ± 4	0.17 ± 0.04	-1.9 ± 6.9
F127/PLGA-130 (no sucrose)	549 ± 135	180 ± 97	0.49 ± 0.12	-4.5 ± 3.5
F127/PLGA-130 (with sucrose)	170 ± 6	127 ± 2	0.10 ± 0.02	-5.3 ± 5.1

[a] Hydrodynamic diameter and PDI were measured by DLS in 10 mM NaCl ± SEM (n ≥ 3).
[b] ζ-potential was measured by laser Doppler anemometry in 10 mM NaCl at pH 7.0. Mean ± SEM (n ≥ 3).

3.8. Effect of osmolality on *in vivo* volume of distribution

Prior studies have demonstrated that administration of hyperosmolar saline in brain tissue results in enlargement of the ECM mesh spacings as water is drawn out of cells into intercellular space via an osmotic gradient established by the hyperosmolar saline (*22-24*).To verify that the osmotic modulation of the intercellular space translates *in vivo*, we administered lyophilized F127/PLGA-NPs via CED in saline-based infusate solutions with varying osmolality and determined their effects on the volume of distribution. Fresh particles were infused at 300 mOsm/kg (iso-osmolar, 0.9 % saline) as a control, yielding 41 ± 4 mm^3. We discovered that the volume of distribution was positively correlated with the osmolality of the infusate solution (Figure 4.13). Quantitively, NPs infused at 480 mOsm/kg (hyper-osmolar) exhibited significantly greater volume of distribution, showing 69 ± 6 mm^3, compared to 370 and 300 mOsm/kg, which exhibited 63 ± 3 mm^3 and 45 ± 5 mm^3, respectively.

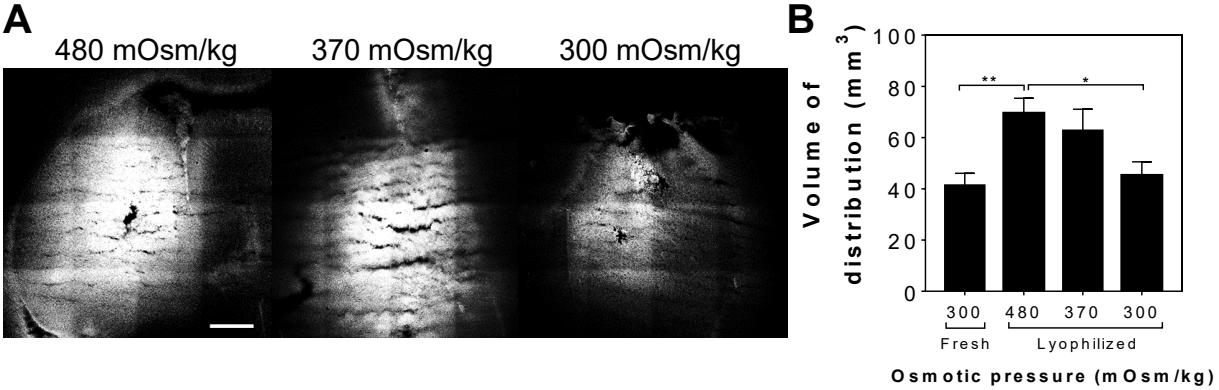

Figure 4.13: Volume of distribution of lyophilized F127/PLGA-NPs in healthy rat brain tissues at various osmotic pressures. (A) Representative 2D images depicting volumetric distribution at the infusion site of lyophilized F127/PLGA-NPs in healthy rat brains at various osmotic pressures: 480 mOsm/kg, 370 mOsm/kg, and 300 mOsm/kg, obtained by confocal microscopy immediately after NPs treatment. Sale bar = 1 mm. **(B)** Quantification of the volume of distribution of lyophilized F127/PLGA-NPs (n ≥ 3 rats). Differences are statistically significant as indicated (* $p < 0.05$, ** $p < 0.01$).

4. Discussion

Pluronic-coating enhances NPs physicochemical properties for brain penetration, including colloidal stability and near-neutral surface charge. The size and charge can be manipulated as necessary by adjusting the starting PLGA concentration but keeping into consideration that the volumetric distribution is inversely correlated to the hydrodynamic diameter, without altering the colloidal stability. This demonstrates that the “mesh-like” pores sizes of the brain tolerate for a dynamic equilibrium when slow pressure gradients occur, which allow “expansion” and “flexibility” for enough penetration when larger, but well coated, NPs are infused via CED. F127/PLGA-NPs provided the highest volume of distribution in healthy brain parenchyma, with great particle retention after 48 hours from CED. We also confirmed that this new design, F127/PLGA-NPs, can efficaciously achieved widespread distribution into a highly aggressive orthotopic brain tumor model when combined with CED, becoming the lead Pluronic-coated formulation for our further NPs studies, utilizing chemotherapeutics for brain tumors (next Chapter). Lastly, we sought to alter the pore sizes of the rat brain ECM by using lyophilized NPs with infusate solutions of varying osmolality, which improved the volumetric distribution *in vivo*. The combination approach of the “ready-to-use” F127/PLGA-NPs, administered in hyper-osmolar infusate solutions via CED, may be widely employed to promote widespread delivery of therapeutics throughout the brain.

As discussed in previous chapters, the CED approach overcomes a major obstacle hindering the development of drug therapies, i.e. poor local diffusion, by allowing slower infusion rates and controlled pressure gradients in the brain parenchyma. However, as we have shown before, the CED technique is not enough for achieving widespread distribution. Poloxamers such as F127, F98, and F68, consist of a hydrophobic polypropylene oxide (PPO) block and hydrophilic polyethylene oxide (PEO) segments, where the composition (PPO:PEO) and MW (block length) impact the properties of the surfactant (*25*). Without Pluronic coatings, PLGA NPs have exposed hydrophobic regions on the particle core and ζ-potentials more negative

than -40 mV. These particles showed to adhere to components within the brain parenchyma by electrostatic or hydrophobic interactions, limiting the diffusive nature of the particles even after CED. Furthermore, we confirmed that although the significant differences in the surface charge of the various types of PLGA NPs do not affect the colloidal stability under physiological conditions, widespread distribution remains inversely correlated with the ζ-potentials. Since F127 has a longer PPO segment compared to F98 and F68 (*5*), it allowed better shielding of any exposed hydrophobic regions. Consequently, F127 demonstrated better volumetric distribution in healthy brain tissues than F98, F68, and uncoated PLGA NPs, respectively.

The pore sizes of the brain ECM has been previously estimated to be ~38 - 64 nm (*26*), but we have recently re-evaluated them using non-adhesive probes to be as large as ~110 nm (*20*). Therefore, there seems to stand a “myth” about the size-threshold for brain tissue penetration to be less than 100 nm. However, a lot of studies have combined the CED approach with nanocarriers possessing ~100 - 150 nm in size to treat brain tumors (*27*). Very few studies have used the CED technique to infuse nanocarriers with larger diameters, probably due to the known size-constraint in the ECM. As an example, MacKay J. A. et al. reported that ~200 nm liposomes penetrated less than 80 nm liposomes even when shielded with PEG (*28*). Similarly, Zhan W. et al. reported that liposomes with 100 nm and 135 nm in diameter have comparable diffusivity in tumor tissue, whereas the value reduces by one order of magnitude when diameter reaches 500 nm (*29*). This is consistent with what we saw when infusing F127/PLGA-NPs with diameters larger than ~160 nm, which experienced a reduction in the volumetric distribution by ~2-fold after CED. Based on these results, we determined that non-adhesive NPs, smaller than ~150 nm, are preferable for maximum brain tissue penetration, particularly for brain tumor applications.

The unique pathological hallmarks of brain tumors, particularly malignant gliomas, present significant challenges for CED. First, brain tumors are often characterized by the presence of necrotic regions, hemorrhage and fibrin clots, making them naturally heterogeneous structures

(*30*). Second, the increased vascular permeability in tumors and surrounding regions can cause rapid clearance of infused drugs (*27*). Additionally, the high pressure within brain tumors can lead to reflux or backflow of the infusate up through the catheter (*18*). These features have shown to affect distribution of polymer-based NPs after CED. Therefore, nanoparticle distribution depends on the size and properties of the tumor and appears to be heterogeneous and asymmetric (*31*). Saucier-Sawyer J. K. et al. showed how significant quantities of PLGA NPs tend to accumulate in the peritumoral space, such that most of the tumor is surrounded by particles which are distributed along the tumor margins. In our studies, images from F127/PLGA-NPs infused into large F98 tumors showed consistent coverage of the tumor, where the margins of these larger tumors are surrounded by the "excess" of particles that diffused further away from the tumor core due to the "human-error" of the CED execution. These findings suggest that tumor size and NPs characteristics are important criteria that should be considered when determining infusion site and parameters for CED.

The steric obstruction imposed by the ECM structure remains a challenging limitation to non-adhesive NPs for achieving widespread distribution in the brain (*32*), particularly when relatively large NPs are required. To overcome this hurdle, Nicholson et al. and Zhang C. et al. have demonstrated that exposure of brain tissues to modestly hyperosmolar solutions (500 mOsmol/kg) increases the volume of the intercellular space, which minimizes the tissue's resistance to NP diffusion (*23, 24*). In agreement with these studies, we demonstrated that the osmotic modulation of the "ready-to-use" F127/PLGA-NPs resulted in enhanced volume of distribution, by enlargement of the ECM mesh spacings as water is drawn out of cells into intercellular space via an osmotic gradient established by the hyperosmolar saline.

5. Conclusions

In this study, we showed the use of Pluronic coatings to improve the ability of the most-widely used biodegradable PLGA nanoparticle platform to penetrate within the brain parenchyma. This led to the discovery of a new brain-penetrating nanoparticle formulation, F127/PLGA-NPs, for future drug studies in brain tumors. We also developed a simple and safe method to maximize the distribution of therapeutic F127/PLGA-NPs in the brain, combining the CED approach in a hyperosmolar infusate solution, that could address major drawbacks currently associated with CED applications in clinical trials, including limited ECM distribution and perivascular sequestration. Additional studies need to be completed to optimize and determine drug-loading and release dependence on formulation parameters to obtain a nanoparticle platform that can penetrate to infiltrative tumor cells and deliver a sustained, therapeutically effective amount of drug.

6. References

1. E. Allard, C. Passirani, J. P. Benoit, Convection-enhanced delivery of nanocarriers for the treatment of brain tumors. *Biomaterials* **30**, 2302-2318 (2009).
2. D. J. Wolak, R. G. Thorne, Diffusion of macromolecules in the brain: implications for drug delivery. *Mol Pharm* **10**, 1492-1504 (2013).
3. H. Heinz *et al.*, Nanoparticle decoration with surfactants: Molecular interactions, assembly, and applications. *Surface Science Reports* **72**, 1-58 (2017).
4. R. Gref *et al.*, Biodegradable long-circulating polymeric nanospheres. *Science* **263**, 1600-1603 (1994).
5. A. P.-B. a. N. P. E. Barry, Pluronic® block-copolymers in medicine: from chemical and biological versatility to rationalisation and clinical advances. *Polym. Chem.* , 3291-3297 (2014).
6. S. A. Kulkarni, S. S. Feng, Effects of surface modification on delivery efficiency of biodegradable nanoparticles across the blood-brain barrier. *Nanomedicine (Lond)* **6**, 377-394 (2011).
7. A. Ambruosi *et al.*, Influence of surfactants, polymer and doxorubicin loading on the anti-tumour effect of poly(butyl cyanoacrylate) nanoparticles in a rat glioma model. *J Microencapsul* **23**, 582-592 (2006).
8. B. Petri *et al.*, Chemotherapy of brain tumour using doxorubicin bound to surfactant-coated poly(butyl cyanoacrylate) nanoparticles: revisiting the role of surfactants. *J Control Release* **117**, 51-58 (2007).
9. W. G. Singleton *et al.*, Convection enhanced delivery of panobinostat (LBH589)-loaded pluronic nano-micelles prolongs survival in the F98 rat glioma model. *Int J Nanomedicine* **12**, 1385-1399 (2017).
10. F. Danhier *et al.*, PLGA-based nanoparticles: an overview of biomedical applications. *J Control Release* **161**, 505-522 (2012).

11. H. K. Makadia, S. J. Siegel, Poly Lactic-co-Glycolic Acid (PLGA) as Biodegradable Controlled Drug Delivery Carrier. *Polymers (Basel)* **3**, 1377-1397 (2011).
12. P. Kocbek, S. Baumgartner, J. Kristl, Preparation and evaluation of nanosuspensions for enhancing the dissolution of poorly soluble drugs. *Int J Pharm* **312**, 179-186 (2006).
13. J. Zhou *et al.*, Highly penetrative, drug-loaded nanocarriers improve treatment of glioblastoma. *Proc Natl Acad Sci U S A* **110**, 11751-11756 (2013).
14. N. Sharma, P. Madan, S. Lin, Effect of process and formulation variables on the preparation of parenteral paclitaxel-loaded biodegradable polymeric nanoparticles: A co-surfactant study. *Asian Journal of Pharmaceutical Sciences* **11**, 404-416 (2016).
15. V. R. Recinos *et al.*, Combination of intracranial temozolomide with intracranial carmustine improves survival when compared with either treatment alone in a rodent glioma model. *Neurosurgery* **66**, 530-537; discussion 537 (2010).
16. B. Tyler *et al.*, A thermal gel depot for local delivery of paclitaxel to treat experimental brain tumors in rats. *J Neurosurg* **113**, 210-217 (2010).
17. A. K. Vellimana *et al.*, Combination of paclitaxel thermal gel depot with temozolomide and radiotherapy significantly prolongs survival in an experimental rodent glioma model. *Journal of Neuro-Oncology* **111**, 229-236 (2013).
18. A. Jahangiri *et al.*, Convection-enhanced delivery in glioblastoma: a review of preclinical and clinical studies. *J Neurosurg* **126**, 191-200 (2017).
19. E. Song *et al.*, Surface chemistry governs cellular tropism of nanoparticles in the brain. *Nat Commun* **8**, 15322 (2017).
20. E. A. Nance *et al.*, A dense poly(ethylene glycol) coating improves penetration of large polymeric nanoparticles within brain tissue. *Sci Transl Med* **4**, 149ra119 (2012).
21. A. Giese, R. Bjerkvig, M. E. Berens, M. Westphal, Cost of Migration: Invasion of Malignant Gliomas and Implications for Treatment. *Journal of Clinical Oncology* **21**, 1624-1636 (2003).

22. K. C. Chen, C. Nicholson, Changes in brain cell shape create residual extracellular space volume and explain tortuosity behavior during osmotic challenge. *Proc Natl Acad Sci U S A* **97**, 8306-8311 (2000).

23. J. Kume-Kick *et al.*, Independence of extracellular tortuosity and volume fraction during osmotic challenge in rat neocortex. **542**, 515-527 (2002).

24. C. Zhang *et al.*, Strategies to enhance the distribution of nanotherapeutics in the brain. *J Control Release* **267**, 232-239 (2017).

25. E. V. Batrakova, A. V. Kabanov, Pluronic block copolymers: evolution of drug delivery concept from inert nanocarriers to biological response modifiers. *J Control Release* **130**, 98-106 (2008).

26. R. G. Thorne, C. Nicholson, In vivo diffusion analysis with quantum dots and dextrans predicts the width of brain extracellular space. *Proc Natl Acad Sci U S A* **103**, 5567-5572 (2006).

27. Y. E. Seo, T. Bu, W. M. Saltzman, Nanomaterials for convection-enhanced delivery of agents to treat brain tumors. *Curr Opin Biomed Eng* **4**, 1-12 (2017).

28. J. A. MacKay, D. F. Deen, F. C. Szoka, Jr., Distribution in brain of liposomes after convection enhanced delivery; modulation by particle charge, particle diameter, and presence of steric coating. *Brain Res* **1035**, 139-153 (2005).

29. W. Zhan, C. H. Wang, Convection enhanced delivery of liposome encapsulated doxorubicin for brain tumour therapy. *J Control Release* **285**, 212-229 (2018).

30. R. Saito, T. Tominaga, Convection-enhanced Delivery of Therapeutics for Malignant Gliomas. *Neurologia medico-chirurgica* **57**, 8-16 (2017).

31. J. K. Saucier-Sawyer *et al.*, Distribution of polymer nanoparticles by convection-enhanced delivery to brain tumors. *J Control Release* **232**, 103-112 (2016).

32. E. Sykova, C. Nicholson, Diffusion in brain extracellular space. *Physiological reviews* **88**, 1277-1340 (2008).

Karina Negrón, B.S. (PhD candidate)

400 N Broadway, Robert H. and Clarice Smith Building, Room 6001

Baltimore, MD 21231

knieves1@jhmi.edu

Cellphone: (939) 642-3334

I. EDUCATION

Johns Hopkins School of Medicine
Pharmacology and Molecular Sciences PhD Program
Graduation 03/2019

Relevant coursework in Chemistry: Organic Mechanisms in Biology, Mechanisms in Bio-Organic Chemistry, Macromolecular Structure and Analysis, Biochemical and Biophysical Principles, and Neuropathology ≥ 12 semester hours of Chemistry

Relevant coursework in Pharmacology: Graduate Pharmacology, Topics in Pharmacology, Principles of Drug Development, Principles of Clinical Pharmacology ≥ 12 semester hours of Pharmacology

Relevant coursework in Biology: Cell Structure and Dynamics, Molecular Biology and Genomics, Organ Physiology, Cell Structure and Dynamics, Pathways and Regulations, Computational Biology and Bioinformatics ≥ 12 semester hours of Biology

University of Puerto Rico at Cayey
Chemistry B.S. (Magna Cum Laude)
Degree acquired 06/2014

Relevant coursework in Chemistry: Analytical Chemistry, Instrumental Analytical Chemistry, Organic Chemistry I-II, Organic Chemistry Lab I-II, Inorganic Chemistry, Biochemistry, Physical Chemistry I-II, and Physical Chemistry lab I-II ≥ 30 semester hours of Chemistry

---

II. HONORS AND AWARDS

2016-2019	National Research Service Award (NRSA) Individual Predoctoral Fellowship (F31)
2018	Best Presentation Award, Pharmacology Research Symposium, Johns Hopkins
2018	Carl Storm Underrepresented Minority (CSURM) Fellowship
2018	Collaborative Teaching Fellows Scholarship, Johns Hopkins
2013-2014	The American Chemical Society (ACS) Scholars Program Scholarship
2010-2014	Honor Student Award, University of Puerto Rico at Cayey
2013	Best Presentation Award, Research Symposium, Yale University
2013	Best Speaker Award, University of Puerto Rico at Cayey
2012-2014	Research Initiative for Scientific Enhancement (RISE) Program (R25) Fellowship
2012	Best Presentation Award, University of Puerto Rico at Cayey

---

III. CERTIFICATIONS IN TEACHING

2018 CIRTL Certificate: An Introduction to Evidence-Based STEM Undergraduate Teaching
2018 Collaborative Teaching Fellowship Program, Johns Hopkins University
2018 Program Completion at the Teaching Academy, Johns Hopkins University
2017 Teaching Institute, Johns Hopkins University

IV. TEACHING AND MENTORING EXPERIENCE

2018 (Spring Semester) Teaching Intern, Biochemistry Course at Goucher College, Towson, MD
Reference: Professor Judith Levine, judith.levine@goucher.edu
410.337.6525

2014-Present (Mentorship Experience in the Research Laboratory):

Undergraduate Research Students

1. Tina Huang, *Neuroscience* (06/2018 – present)
2. Sunny Chen, *Chemical and Biomolecular Engineering* (03/2018 - present)
3. Namir Khalasawi, *Chemical and Biomolecular Engineering* (04/2017- present)
4. Jillian Ho, *Chemical and Biomolecular Engineering* (04/2017- present)
5. Casey Zhu, *Chemical and Biomolecular Engineering* (04/2017- present)
6. Billy Lu, *Cellular and Molecular Biology* (06/2016-06/2017)
7. YoungEun Kim, *Chemical and Biomolecular Engineering* (12/2014-06/2017)
8. Miguel Sobral, *Biomedical Engineering* (12/2014-06/2017)
9. Amna Ali, *Biomedical Engineering* (01/2016-08/2017)
10. Kali Barnes, *Biomedical Engineering* (01/2016-08/2016)
11. Michael Mudgett, *Biomedical Engineering* (06/2015-05/2016)

Research Scholar (Visiting Student)

1. Umara Afzal, PMAS-Arid Agriculture University, Pakistan (06/2015-12/2016)

High School Students

1. Malavika Pillai (Summer 2018)
2. Jack Stump, Archbishop Spalding High School, MD (Summer 2016)
3. Ayush Jain, Marriotts Ridge High School, MD (Summer 2016)

V. PUBLICATIONS

1. **Negron K**, Khalasawi N, Lu B, Ho C.Y., Lee J, Shenoy S, Wang T.H., Hanes J, Suk JS. Widespread Gene Transfer to Malignant Gliomas with In vitro-to-In vivo Correlation. *Journal of Controlled Released*. Accepted.

2. Huang X, Zhuang J, Chung SW, Halpert G, **Negron K**, Huang B, Hwang P, Hanes J, Suk JS. Hypoxia-tropic Protein Nanocages for Modulation of Tumor- and Chemotherapy-associated Hypoxia. *ACS Nano*. (IF 13)

3. Elam AW, Cao W, Kang H, Huehn A, Hocky GM, Prochniewicz E, Schramm AC, **Negron K**, Garcia J, Bonello TT, Gunning PW, Thomas DD, Voth GA, Sindelar CV, De La Cruz EM. Phosphomimetic S3D-Cofilin Binds but Only Weakly Severs Actin Filaments. *J. Biol. Chem.* 2017; doi:10.1074/jbc.M117.808378 (IF 4)

VI. MANUSCRIPTS IN PREPARATION

1. **Negron K**, Zhu C, Chen S, Khalasawi N, Ho C.Y., Eberhart CG, Hanes J, Suk JS. New Biodegradable Polymer-Based DNA Nanoparticles to Achieve Widespread Distribution in Malignant Gliomas.

2. **Negron K**, Huang T, Chen S, Khalasawi N, Sur S, Eberhart CG, Hanes J, Suk JS. Developing New Pluronic-Coated Brain Penetrating Drug-Loaded Nanoparticles Against Glioblastoma.

3. Curley C, Mead B, Kim N, **Negron K**, Garrison W, Song J, Miller W. G., Mandell J, Purow B.W., Suk JS, Hanes J, Price RJ. Focused Ultrasound Tissue Modulation for Augmented Nanoparticle Penetration and Efficacy in the Central Nervous System.

4. Curley CT, Mead BP, Kim N, **Negron K**, Song J, Miller WG, Garrison W, Kingsmore KM, Munson JM, Klibanov A, Suk JS, Hanes J, Price RJ. (In Preparation). Brain-Penetrating Nanoparticle-Mediated Non-Viral Transfection of Brain Tumors via Pulsed Focused Ultrasound.

5. Rao D, Phal A, Naga V, **Negron K**, Oh Y, Hanes J, Suk JS. (In Preparation). Combinatorial Approach of DNA-loaded Brain Penetrating Nanoparticles and Tumor-specific Promoter for Widespread yet Cancer Selective Gene Transfer to Brain Tumors.

VII. BOOK CHAPTERS

1. **Negron K**, Khalasawi N, Suk JS. Strategies to Enhance the Distribution of Nanotherapeutics in the Brain via Convection Enhanced Delivery. Book Chapter from: Nanotherapy for Brain Tumor Drug Delivery. Neuromethods series (Springer Nature Publishing).

VIII. TRAVEL AWARDS

2018	ASGCT Underrepresented Minority Travel Award
2017	Pharmacology Travel Award, Johns Hopkins University
2017	Underrepresented Graduate Student Travel Award, ASPET Experimental Biology
2013	Society of Toxicology (SOT) Travel Award
2013	The American Chemical Society (ACS) Travel Award
2012	Annual Biomedical Research Conference for Minority Students (ABRCMS) Travel Award

---

IX. RESEARCH EXPERIENCE

2014-Present — Johns Hopkins School of Medicine, Dr. Justin Hanes and Dr. Jung Soo Suk
Department of Pharmacology and The Center for Nanomedicine
Drug and Gene Nano-Therapy for Malignant Gliomas and CNS Diseases
hanes@jhmi.edu; jsuk@jhmi.edu

2014 (Rotation) — Johns Hopkins School of Medicine, Dr. Martin G. Pomper
Department of Radiology and Neurosurgery
High-Throughput Screening for Blood Brain Barrier Permeability
mpomper@jhmi.edu

2014 (Rotation) — Johns Hopkins School of Medicine, Dr. James T. Stivers
Department of Pharmacology and Molecular Sciences
Enzyme Kinetics and Pharmacological Assays in HIV-1 Infected Cells
jstivers@jhmi.edu

2012-2014 — University of Puerto Rico at Cayey, Dr. Vibha Bansal
Department of Biochemistry
Development of Protein Purification and Analytical Assays
vibha.bansal@upr.edu

2013 (Summer) — Yale University, Dr. Enrique M. De La Cruz
Department of Molecular Biology and Biochemistry
Enzyme Kinetics and Fluorescence Microscopy for Experimental Biophysics
enrique.delacruz@yale.edu

2012 (Summer) — University of Pennsylvania, Dr. Tobias Baumgart
Department of Biophysics and Biochemistry
Enzyme Kinetics and Fluorescence Microscopy for Oncolytic Pathways
baumgart@sas.upenn.edu

X. CONFERENCE ABSTRACTS

1. **Karina Negron**, Namir Khalasawi, Jillian Ho, Justin Hanes, Jung Soo Suk. (2018) Brain Penetrating Nanoparticles (BPN) and Convection Enhanced Delivery (CED) for Gene Transfer in the Brain. Gordon Research Conference Barriers to CNS 2018: New London, New Hampshire.

2. Colleen T. Curley, Brian Mead, **Karina Negron**, Namho Kim, Jung Soo Suk, Richard J. Price. (2018) Augmented Brain-Penetrating Nanoparticle-Mediated Non-Viral Transfection of Brain Tumors Via Pre-Treatment with Pulsed Focused Ultrasound. ITSU 2018: Nashville, Tennessee.

3. **Karina Negron**, Amna Ali, Billy Lu, Clark Zhang, Justin Hanes, Jung Soo Suk. (2017) Optimal strategies for Convection Enhanced Delivery (CED) of DNA Brain-Penetrating Nanoparticles (DNA-BPN) for Glioblastoma (GBM) Treatment. EB 2017: Chicago, Illinois.

4. Dongeun Heo, **Karina Negron**, Jung Soo Suk, Justin Hanes, Dwight Bergles. (2017) Non-viral nanocarriers for CRISPR-Cas9 gene editing in Cortical Astrocytes for ALS Applications. Society for Neuroscience Meeting. Washington, DC.

5. Colleen T. Curley, Ying Zhang, **Karina Negron**, G. Wilson Miller, Alexander L. Klibanov, Roger Abounader, Jung Soo Suk, Justin Hanes, Richard J. Price. (2016) MR Image-Guided Delivery of Non-Viral miRNA-34a Gene Vectors via Focused Ultrasound Inhibits Tumor Growth in a Mouse Glioma Model. BMES 2016 Annual Meeting: Minneapolis, Minnesota.

6. Richard J. Price, Brian P. Mead, Colleen F. Curley, G. Wilson Miller, Roger Abounader, Namho Kim, **Karina Negron**, Panagiotis Mastorakos, Jung Soo Suk, Justin Hanes. MR Image-Guided Nanoparticle Delivery with Focused Ultrasound (2016). NannoDDS 2016: Baltimore, Maryland.

7. Colleen T. Curley, Ying Zhang, **Karina Negron**, G. Wilson Miller, Alexander L. Klibanov, Roger Abounader, Jung Soo Suk, Justin Hanes, Richard J. Price. (2016) MR Image-Guided Delivery of Non-Viral miRNA-34a Gene Vectors via Focused Ultrasound Inhibits Tumor Growth in a Mouse Glioma Model. NanoDDS 2016: Baltimore, Maryland.

8. Umara Afzal, Amna Ali, **Karina Negron**, Michael Noback, Clark Zhang, Muhamad Gulfraz, Jung Soo Suk, Justin Hanes. (2016) Albumin Based Brain Penetrating Nanoparticles for Localized Drug Delivery. Nanno DDS 2016: Baltimore, Maryland.

9. W. Austin Elam, Hyeran Kang, Ewa Prochniewicz, **Karina Negron**, David Thomas, Enrique M. De La Cruz. (2015) Phosphomimic S3D Cofilin Binds Actin Filaments but Does Not Sever Them. Biophysical Society 2015 Annual Meeting Baltimore, Maryland.

10. **Karina Negron**, Vibha Bansal, Ezio Fasoli. (2013) Developing Method for the Estimation of L-lysine Bound to Regenerated Cellulose Membranes. ACS Annual Meeting 2013: New Orleans, Louisiana.

11. **Karina Negron**, Vibha Bansal, Ezio Fasoli. (2013) Developing Method for the Estimation of L-lysine Bound to Regenerated Cellulose Membranes. SOT Annual Meeting 2013: San Antonio, Texas.

12. **Karina Negron**, Vibha Bansal, Ezio Fasoli. (2013) Developing Method for the Estimation of L-lysine Bound to Regenerated Cellulose Membranes. ABRCMS Annual Meeting 2012: New Orleans, Louisiana.

XI. RESEARCH SEMINARS

1. Brain Penetrating Nanoparticles (BPN) for Brain Tumors (2018). Department of Pharmacology: Research in Progress (RIP). Johns Hopkins School of Medicine.

2. Brain Penetrating Nanoparticles for Glioblastoma (2017). University of Puerto Rico at Cayey.

3. Formulation of Brain Penetrating Nanoparticles (BPN) for Glioblastoma Treatment via Convection Enhanced Delivery (2016). Department of Pharmacology: Research in Progress (RIP). Johns Hopkins School of Medicine.

4. Improving the Therapeutic Relevance of Cisplatin for Treatment of Glioblastoma Using Brain Penetrating Nanoparticles (2014). Department of Pharmacology: Rotation Presentations. Johns Hopkins School of Medicine.

5. Developing a Quantification Assay for L-Lysine in Regenerated Cellulose Membranes for Protein Purification (2013). Department of Chemistry Research Symposium. University of Puerto Rico at Cayey.

6. Enzyme Kinetics for Functional Regulation of Cofilin as an Actin Severing Protein (2013). Sackler NSF REU. Yale University.

7. Developing a Quantification Assay for L-Lysine in Regenerated Cellulose Membranes for Protein Purification (2012). RISE Program Research Symposium. University of Puerto Rico at Cayey.

8. Enzyme Kinetics of PIP3 Dephosphorylation by PTEN Enzyme in Cancer (2012). University of Pennsylvania.

XII. LABORATORY SKILLS

1. Non-viral gene therapy
2. Brain surgery in rodents
3. Orthotopic brain tumor models
4. Xenografts brain tumor models
5. Develop survival curves
6. Polymer synthesis
7. Drug-release *in vitro*
8. Nanoparticle formulation (drug and DNA-based)
9. Cell-culture (including primary cells)
10. 3D-cell culture tissue organoids and tumor spheroids
11. Confocal Microscopy
12. Real-time fluorescence microscopy in *ex vivo* and *in vivo* brain tissue
13. Live-imaging (IVIS) in rodents
14. *In vitro* drug screening (cell viability assays)
15. Western-blotting
16. RT-PCR
17. H-NMR
18. HPLC
19. Cell sorting-Flow cytometry
20. Immunohistochemistry

XIII. OTHER SKILLS

1. Write SOPs
2. Animal Protocols
3. Research Proposals
4. Protocol Amendments

5. Research-Progress Reports
6. Review Articles
7. Presentation and oral skills
8. Bilingual (Spanish and English)

XIV. SOFTWARES AND PROGRAMS KNOWLEDGE

1. Matlab
2. Imaris Bitplane
3. ImageJ
4. ZEN
5. AccuriFlow
6. MetaMorph
7. Mest-Rec
8. KaleidaGraph
9. GraphPad Prism
10. EndNote

XV. PROFESSIONAL SOCIETY MEMBERSHIPS

1. American Brain Tumor Association
2. American Chemical Society
3. Society of Toxicology
4. The American Society for Pharmacology and Experimental Therapeutics
5. Biophysical Society

XVI. EXTRACURRICULAR ACTIVITIES

Present Teacher for Middle School and High School girls, National Girls Ministries Club
2018 Teaching Intern at Goucher College, department of Chemistry, Towson, MD
2018 Team Member, Race for Hope: Fight Against Brain Tumors, Washington, DC
2018 Math Tutor at Elementary School Level
2017 Leader of Campaign Hats and Quilts for Love, Johns Hopkins Pediatric Oncology Unit
2016 Volunteer/Teacher/Group Leader, National Girls Ministries, Youth Program of Assembly of God
2015 Team Member, Cystic Fibrosis Foundation Great Strides Walk, Johns Hopkins University
2015 Math Tutor to Middle School Students
2014 Tutor at Centro de Apoyo al Estudiante (CAE), University of Puerto Rico at Cayey

XVII. References

Research Advisor: Dr. Jung Soo Suk; jsuk@jhmi.edu; (410) 371-9085

Teaching Mentor: Dr. Judith Levine; judith.levine@goucher.edu; (410) 715-8787

PhD Program Director: Dr. Caren Meyers; cmeyers@jhmi.edu ; (410) 502-4807